이학박사 학위논문

A Multi-Wavelength Study of Galaxy Transition in Different Environments

다파장 관측 자료를 이용한 다양한 환경에서의 은하 진화 연구

2017년 8월

서울대학교 대학원

물리천문학부 천문학전공

이 광 호

ABSTRACT

The role of environment in galaxy evolution is an important issue in recent astronomy. In order to better understand how environment affects galaxy transition from star-forming galaxies to quiescent galaxies, we conduct several studies using multi-wavelength data, from near-ultraviolet to mid-infrared (MIR), of nearby galaxies in various environments.

First, using the *Wide-field Infrared Survey Explorer (WISE)* data, we study the MIR properties of the galaxies in the A2199 supercluster at $z = 0.03$ to understand the star formation activity of galaxy groups and clusters in the supercluster environment. We classify the supercluster galaxies into three classes in the MIR color-luminosity diagram: MIR blue cloud (massive, quiescent and mostly early-type), MIR star-forming sequence (mostly late-type), and MIR green valley galaxies. These MIR green valley galaxies are distinguishable from the optical green valley galaxies, in the sense that they belong to the optical red sequence. We find that the fraction of each MIR class does not depend on virial mass of each group/cluster. We compare the cumulative distributions of surface galaxy number density and cluster/group-centric distance for the three MIR classes. MIR green valley galaxies show the distribution between MIR blue cloud and MIR star-forming sequence galaxies. However, if we fix galaxy morphology, early- and late-type MIR green valley galaxies show different distributions. Our results suggest a possible evolutionary scenario of these galaxies: 1) Late-type MIR star-forming sequence galaxies $\rightarrow$ 2) Late-type MIR green valley galaxies $\rightarrow$ 3) Early-type MIR green valley galaxies $\rightarrow$ 4) Early-type MIR blue cloud galaxies. In this sequence, star formation of galaxies is quenched before the galaxies enter the MIR green valley, and then morphological transformation occurs in the MIR green valley.

Second, we study the MIR properties of galaxies in compact groups and their en-

vironmental dependence. We find that the MIR $[3.4] - [12]$ colors of compact group early-type galaxies are on average bluer than those of cluster early-type galaxies. When compact groups have both early- and late-type member galaxies, the MIR colors of the late-type members in those compact groups are bluer than the MIR colors of cluster late-type galaxies. As compact groups are located in denser regions, they tend to have larger early-type galaxy fractions and bluer mean MIR colors of member galaxies. These trends are also seen for neighboring galaxies around compact groups. However, compact group member galaxies always have larger early-type galaxy fractions and bluer MIR colors than their neighboring galaxies. Our findings suggest that the properties of compact group galaxies depend on both internal and external environments of compact groups, and that galaxy evolution is faster in compact groups than in the central regions of clusters. Furthermore, our findings suggest that there is a connection between compact group members and their neighboring galaxies, and that neighboring galaxies are sources of compact group members.

Third, we present the two-dimensional distribution of stellar population in five E+A galaxies ($0.03 < z < 0.05$) from GMOS-N/IFU spectroscopy. Numerical simulations demonstrated that E+A galaxies formed by major mergers contain young stellar populations (e.g., A-type stars) that are centrally-concentrated within scales of 1 kpc. However, several IFU studies reported that A-type stars are widely distributed on >kpc scales. In contrast, Pracy et al. (2013) found a central concentration of A-stars and strong negative Balmer absorption line gradients within 1 kpc scales for local ($z < 0.04$) E+A galaxies. They claimed that previous studies failed to detect the central concentration because the E+A galaxies samples in previous studies are too far ($z \sim 0.1$) to resolve the central kpc scales. To check Pracy et al.'s argument and the expectation from simulations, we selected five E+A galaxies at $0.03 < z < 0.05$. Thanks to good seeing ($\sim 0.''8 \simeq 0.7$ kpc) of our observations, we are able to resolve the central 1 kpc region of our targets. We find that all five

galaxies have negative Balmer line gradients, but that three galaxies have flatter gradients than those reported in Pracy et al. We discuss the results in relation with galaxy merger history.

Finally, we investigate the connection between the presence of bars and AGN activity, using a volume-limited sample of ∼9,000 late-type galaxies with axis ratio $b/a > 0.6$ and $M_r < -19.5$ at low redshift ($0.02 \leq z \lesssim 0.055$), selected from Sloan Digital Sky Survey Data Release 7. We find that the bar fraction in AGN-host galaxies (42.6%) is ∼2.5 times higher than in non-AGN galaxies (15.6%), and that the AGN fraction is a factor of two higher in strong-barred galaxies (34.5%) than in non-barred galaxies (15.0%). However, these trends are simply caused by the fact that AGN-host galaxies are on average more massive and redder than non-AGN galaxies because the fraction of strong-barred galaxies (f_{SB}) increases with $u - r$ color and stellar velocity dispersion. When $u - r$ color and velocity dispersion (or stellar mass) are fixed, both the excess of f_{SB} in AGN-host galaxies and the enhanced AGN fraction in strong-barred galaxies disappears. Among AGN-host galaxies we find no strong difference of the Eddington ratio distributions between barred and non-barred systems. These results indicate that AGN activity is not dominated by the presence of bars, and that AGN power is not enhanced by bars. In conclusion we do not find a clear evidence that bars trigger AGN activity.

Keywords: galaxies: clusters: individual (A2199) – galaxies: evolution – galaxies: groups: general – galaxies: interactions – galaxies: active – galaxies: nuclei – galaxies: Seyfert – galaxies: sprials – galaxies: starburst – galaxies: statistics – galaxies: stellar content – infrared: galaxies

Student Number: 2010-30121

Contents

List of Figures

List of Tables

Chapter 1

Introduction

1.1 Environmental Effects on Galaxy Evolution

A galaxy ecosystem is influenced by its environment. The predominance of early-type galaxies (e.g., ellipticals and lenticulars) in galaxy clusters was discovered long ago (Hubble & Humason 1931; Spitzer & Baade 1951; Abell 1965). Through morphological analysis of $\sim$6000 galaxies in 55 rich clusters ($z \lesssim 0.06$), Dressler (1980) established the "morphology-density relation" that the early-type galaxy fraction increases with increasing local density. Because local density decreases as clustercentric radius increases, the morphology-density relation is consistent with the "morphology-radius relation" suggested by Oemler (1974). These early findings provide important insights on environment-driven galaxy evolution.

Several physical mechanisms have been proposed to explain the predominance of early-type galaxies in the cluster environment. The proposed mechanisms can be grouped into three categories. First, ram pressure stripping and thermal evaporation: removal of the cold interstellar medium (ISM) gas in galaxies through the interactions between galaxies and the hot intracluster medium (ICM) in clusters (Gunn & Gott 1972; Cowie & Songaila 1977; Nulsen 1982). Second, strangulation or

starvation: removal of the hot halo gas reservoirs by interaction with the hot ICM, leading to a depletion of the cold gas supply from the halo to galaxies (Larson et al. 1980; Bekki et al. 2002; Peng et al. 2015). Third, harassment: impulsive heating and morphology transformation caused by frequent high-speed tidal interactions between cluster galaxies and/or by tidal interaction with cluster potential well (Byrd & Valtonen 1990; Moore et al. 1996).

From late-type (star-forming) galaxies to early-type (quiescent) galaxies, these proposed mechanisms require different time-scales in galaxy transition. Furthermore, the efficiency of each mechanism on galaxies also depends on the characteristics of each galaxy (e.g. stellar mass) and the characteristics of the cluster environment (Boselli & Gavazzi 2006). For example, ram pressure and strangulation, driven by interaction with the hot ICM, are more efficient for dwarf galaxies rather than for giant galaxies (Haines et al. 2007). The harassment effect is greater in more-massive (or relaxed) clusters than less-massive (or unrelaxed) clusters (Dressler et al. 1997). Therefore, more studies are needed to answer the question of what is the main mechanism driving the environmental dependence of cluster galaxies.

Many proposed mechanisms in the previous studies are oriented to the cluster environment. However, many observational studies found evidence that environment-driven galaxy evolution already begins in group-scale environments. Postman & Geller (1984) found that the morphology-density relation is not restricted to clusters, but that it is also found in groups of galaxies. Zabludoff & Mulchaey (1998) suggested that the formation of cluster ellipticals, including cD galaxies, is pre-processed via mergers in poor group environments. Later, several studies reported direct observational evidence for star formation quenching of galaxies in group environments (e.g., Tran et al. 2001; Lewis et al. 2002; Wilman et al. 2005, 2008; Weinmann et al. 2006). Because groups are less massive than clusters, environmental effects caused by interaction with the ICM, such as ram pressure, are not expected to be as strong

as in the cluster environment. Instead, galaxy-galaxy interactions may be the main driver for galaxy transition in group environments (e.g., Hickson 1982; Rubin et al. 1990; Coziol et al. 1998a,b; Verdes-Montenegro et al. 2001).

With unprecedentedly large amounts of photometric and spectroscopic data of galaxies from the Sloan Digital Sky Survey (SDSS, York et al. 2000), the role of the environment in controlling various galaxy properties has been extensively studied. Thanks to spectroscopic redshifts with a homogeneous depth ($m_r < 17.77$), SDSS-based studies cover a full range of environments from clusters to the field (Gómez et al. 2003; Balogh et al. 2004; Tanaka et al. 2004; Park et al. 2007, 2008; Park & Hwang 2009; Park & Choi 2009; Blanton & Moustakas 2009; Lee et al. 2012a) including superclusters (Mahajan et al. 2010, 2011; Hwang et al. 2012a; Einasto et al. 2014; Lee et al. 2015; Cohen et al. 2017), compact groups (Sohn et al. 2013, 2015, 2016; Lee et al. 2017), and even filament/void environments (Tempel et al. 2014; Shim et al. 2015; Kuutma et al. 2017).

How to quantify environment is an important issue that directly affects results (Muldrew et al. 2012). Park et al. (2007, 2008) adopted three environmental parameters such as large-scale background density[1], distance to the nearest neighbor galaxy, and morphology of the neighbor (Park & Choi 2005). Park et al. (2007) found that the fraction of early-type galaxies strongly depends on distance to the nearest neighbor galaxy at a given large-scale background density. Interestingly, Park et al. (2008) showed that when a galaxy is located within the nearest neighbor's virial radius, the probability that the two galaxies have the same morphologies increases. Furthermore, Park & Hwang (2009) found that the neighbor's effects are

---

[1]The large-scale density of a galaxy is defined by $\rho_{20}(x)/\bar{\rho} = \sum_{i=1}^{20} \gamma_i L_i W_i(|x_i - x|)/\bar{\rho}$, where x is the location of the galaxy, and γ_i, L_i, x_i, and $\bar{\rho}$ are mass-to-light ratio, luminosity, position of the closest twenty galaxies brighter than $M_r = -19$, and the mean mass density. W_i is the spline-kernel weight function (see Park et al. 2007 for details).

more significant compared to the effects of cluster hot gas outside 0.1 virial radius of clusters. These results suggest that the distance to the neighbor and the neighbor's morphology are important parameters in determining galaxy properties.

However, galaxy transition is not solely caused by environmental effects. Strong outflow, caused by stellar feedback or active galactic nuclei (AGN) feedback, is another mechanism responsible for stripping the ISM gas in galaxies (e.g., Daddi et al. 2007; Silverman et al. 2009). Peng et al. (2010a) presented two distinct processes, "environment quenching" and "mass quenching": stellar mass is a main driver of terminating star formation for high-mass ($\gtrsim 10^{10.5}\ M_\odot$) galaxies independently of environment, while environmental effects are more important for low-mass ($\lesssim 10^{10.5}\ M_\odot$) galaxies. Therefore, we need to consider both the internal and external conditions of galaxies when studying environmental effects on galaxy evolution.

1.2   Why Do We Need Multi-Wavelength Data?

The spectral energy distributions (SEDs) represent the sum of the radiation from stars, gas, and dust in galaxies (e.g., da Cunha et al. 2008). Thus, SEDs provide direct clues on star formation history and the contents in stars, gas, and dust. In the rest-frame, ultraviolet, optical, and near-infrared radiation are mainly dominated by flux from stars with different ages. Ultraviolet and optical radiation suffer from dust attenuation more than near-infrared (Brinchmann et al. 2004). Thus, ultraviolet, optical, and near-infrared radiation provide information about past star formation history, dust attenuation, and also chemical enrichment. Energy absorbed from starlight re-radiates by dust emission at mid- and far-infrared wavelengths. At mid-infrared (MIR) wavelengths ($3 - 30\ \mu$m), the SEDs are also contributed by stellar photospheric emission coming from circumstellar dust around asymptotic giant brach stars (e.g., Piovan et al. 2003; Cassarà et al. 2013; Villaume et al. 2015). Far-infrared and submillimeter wavelengths ($30-500\ \mu$m) are mainly dominated by

emission from warm and cold dust. Thus, far-infrared and submillimeter radiation provide information about dust contents (e.g., Kennicutt 1998; Casey et al. 2014; Lee et al. 2016). Therefore, it is necessary to use multi-wavelength data to understand the physical conditions of the constituents of galaxies (e.g., stars, gas, and dust) and star formation history.

Galaxy transition from the blue cloud to the red sequence is one of the key issues in extragalactic astronomy (e.g., Faber et al. 2007; Tinker et al. 2013). "Green valley" galaxies located in a region between the red sequence and the blue cloud are an important population to understand galaxy transition. Since galaxy number density in the green valley is relatively low, the transition in the green valley is thought to occur during a short timescale of $\lesssim 1$ Gyr (Springel et al. 2005; Faber et al. 2007; Pan et al. 2013). However, Schawinski et al. (2014) mentioned that "the green valley is a red herring[2]." They showed that optical green valley galaxies have different near-ultraviolet (NUV) color distributions depending on morphology. Through comparison with simple stellar population models (Bruzual & Charlot 2003), Schawinski et al. suggested that the NUV color difference can be explained by different quenching timescales of star formation; the quenching timescales of early-type galaxies (< 250 Myr) is much shorter than those of late-type galaxies (> 1 Gyr).

Ko et al. (2012) found that red-sequence early-type galaxies consist not only of quiescent ("red and dead") galaxies but also of another type of galaxies. Some red-sequence early-type galaxies exhibit stronger MIR dust emission than normal early-type galaxies. Ko et al. (2013) found that some early-type galaxies with strong MIR emission also have strong near-ultraviolet (NUV) emission, and found that small ($1 - 5\%$) amount of intermediate-age ($0.5 - 2$ Gyr) stellar populations make the red-sequence early-type galaxies have NUV and/or MIR emission. These findings are attributed to that NUV (< 2 Gyr) and MIR ($< 5 - 10$ Gyr) trace star formation

---

[2] "Red herring" means something that misleads or distracts from a relevant or important issue.

over a longer timescale than optical ($<$ 1 Gyr).

Schawinski et al.'s and Ko et al.'s works are good examples of the need for the multi-wavelength approach in understanding galaxy transition. In this thesis, we also use multi-wavelength data, from NUV to MIR, of nearby galaxies to obtain a better understanding how galaxy transition occurs in different environments.

1.3   A Nearby Supercluster of Galaxies, the A2199 Supercluster

Superclusters are vast complexes displaying numerous different types of galaxy structures. In the supercluster environment, galaxy clusters and groups are interacting with each other, and are connected by filamentary structures. Furthermore, clusters and groups are surrounded by smaller scale structures that are infalling into the most massive clusters. Thus, supercluster environments provide direct evidence of hierarchical structure formation models and a comprehensive picture of the environmental effects on galaxy evolution.

The A2199 supercluster at $z = 0.03$ is one of the most massive galaxy structures in the nearby universe (Rood 1976; Chincarini et al. 1981; Gregory & Thompson 1984; Dixon et al. 1989; Markevitch et al. 1999; Rines et al. 2001, 2002). This supercluster consists of one rich cluster (A2199) and six X-ray bright groups (Mahdavi et al. 2000). The entire region of the supercluster occupies $12° \times 12°$ (roughly 30 Mpc $\times$ 30 Mpc) in the sky. The A2199 supercluster is embedded in a large-scale X-ray emitting filamentary structure (Rines et al. 2001)[3]. Furthermore, the A2199 supercluster is located within the Great Wall (Geller & Huchra 1989; Falco et al. 1999).

---

[3]Rines et al. (2001) found the X-ray structure in A2199 supercluster region using the *ROSAT* All-Sky Survey data (Voges et al. 1999).

A2199 is a regular, rich cluster located at the center of this supercluster. A2199 hosts the nearest prototypical cD galaxy, NGC 6166 (Minkowski 1961; Lachieze-Rey et al. 1985; Lauer 1986; Di Matteo et al. 2001; Kelson et al. 2002), exhibiting a strong cooling flow (Johnstone et al. 2002) and radio jets (Giovannini et al. 1998). A2197W and A2197E are located 1.5° north of A2199. These two galaxy systems were reported as a single rich cluster, A2197, in early studies (Rood 1976; Gregory & Thompson 1984). However, while X-ray emission from A2199 is quite symmetrical and centrally concentrated (Mohr et al. 1995), X-ray emission from A2197 is less centrally concentrated and is elongated (Rines et al. 2001). Thus, Rines et al. (2001, 2002) suggested that A2197 is composed of two groups, A2197W and A2197E, that are interacting with each other. NRGs385, NRGs388, NRGs396, and NGC 6159 (group) are X-ray bright groups with X-ray lumonisities $L_{\rm X} \simeq 10^{42}\ h^{-2}$ erg s^{-1}, comparable to those of A2197W and A2197E, but smaller than $L_{\rm X} \simeq 10^{44}\ h^{-2}$ erg s^{-1} of A2199 (Mahdavi et al. 2000; Rines et al. 2002). By investigating the redshift distribution of supercluster member galaxies as a function of distance from A2199, Rines et al. (2002) suggested that A2197W, A2197E, and NRGs388 are infalling groups bound to the supercluster gravitationally, but that NRGs385 and NRGs396 (maybe NGC 6159 too) are not infalling onto the supercluster in the present epoch.

The entire region of the A2199 supercluster is covered by the SDSS (York et al. 2000) and *Wide-field Infrared Survey Explorer* (*WISE*, Wright et al. 2010). Hwang et al. (2012a) constructed a multi-wavelength catalog of galaxies in the entire region of the A2199 supercluster, by combining the SDSS Data Release 7 (DR7, Abazajian et al. 2009) spectroscopic data and the *WISE* data. The SDSS Spectroscopic data are available for galaxies brighter than $m_r = 17.77$. However, the completeness of the spectroscopic data is low for bright galaxies with $m_r < 14.5$ because of saturation and cross-talk in the spectrograph, and for galaxies in high-density regions due to fiber collision. To reduce this incompleteness problem, they supplemented redshift data

for the SDSS photometric sample of galaxies from several redshift survey data such as the redshift survey of Abell clusters (Hill & Oegerle 1993, 1998), EFAR survey (Wegner et al. 1996, 1999), MX northern Abell cluster redshift survey (Slinglend et al. 1998), Updated Zwicky Catalog (Falco et al. 1999), and the NASA Extragalactic Database. A total of 1529 galaxies with redshifts are included in this catalog, and all these galaxies are detected with the *WISE*.

Using this multi-wavelength catalog, in Chapter 2, we present a detailed view of the various properties of supercluster galaxies and their environmental dependence. We estimate star formation activity of the galaxy systems in the A2199 supercluster, and investigate whether group/cluster mass plays a role in controlling the global star formation activity of the system. Furthermore, we present a new galaxy classification scheme using the *WISE* MIR data, and address how galaxies evolve and how supercluster environment impacts galaxy evolution through the perspective of the MIR.

1.4   The Densest Environment, Compact Groups of Galaxies

Postman & Geller (1984) extended the morphology-density relation, discovered by Dressler (1980), to group environments using the CfA Redshift Survey data (Huchra et al. 1983). This finding broadened the scope of the environmental study of galaxy evolution from cluster environments to group-scale environments. Through numerical simulation, Barnes (1985) showed that groups are "likely sites" for interactions and merging between member galaxies. They also expected that galaxy groups in the local universe consist of a high fraction of merger remnants. These expectations were confirmed by Zabludoff & Mulchaey (1998). They found that the fraction of early-type galaxies in poor groups ranges from the $\lesssim 25\%$ in the field to $\sim 55\%$ in

rich clusters. They also found observational evidence that massive early-type galaxies are formed by galaxy-galaxy mergers in poor groups, and then fall into cluster environments. This "pre-processing" in group environments was confirmed in numerous studies (e.g., Fujita 2004; Balogh et al. 2004; Wilman et al. 2008; Koyama et al. 2011; Lemaux et al. 2012; Hess & Wilcots 2013; Mahajan 2013; Wetzel et al. 2013; Bahé & McCarthy 2015).

Galaxy groups are expected to have frequent interaction between member galaxies because velocity dispersions of group galaxies ($\sim190-750$ km s^{-1}, Rines & Diaferio 2010) are on average smaller than those of cluster galaxies ($\sim400-1300$ km s^{-1}, Rines et al. 2013). In this regard, compact groups are more favorable for galaxy interactions than loose groups[4]. In fact, tidally disturbed features are common in compact group galaxies (e.g., Mendes de Oliveira & Hickson 1994; Hunsberger et al. 1996; Yun et al. 1997; Verdes-Montenegro et al. 2001; Coziol & Plauchu-Frayn 2007; Konstantopoulos et al. 2012; Sohn et al. 2016). Most compact groups show velocity dispersions of $50-350$ km s^{-1} (Sohn et al. 2016), smaller than those of loose groups on average. Furthermore, compact groups are $\lesssim 100$ kpc, much smaller than the typical virial radius of loose groups (~ 0.5 Mpc, Rines & Diaferio 2010) and the typical radius of galaxy clusters (~ 1 Mpc, Park & Hwang 2009; Rines et al. 2013). Thus, compact groups consists of $3-10$ member galaxies concentrated at $\lesssim 100$ kpc, which makes them the densest galaxy systems in the universe. This extremely high galaxy density and low velocity dispersion make compact groups the ideal environment for frequent interaction and mergers between galaxies.

There is an open question of why member galaxies in each compact groups have not merged into a single massive galaxy. The lifetime of compact groups is expected to be very short (shorter than a few Gyr) due to the great likelihood of mergers between member galaxies and short group crossing times (< 0.02 Hubble time,

---

[4]Many studies use the term "loose group" for comparison with compact groups.

Mamon 1987; Barnes 1989; Hickson et al. 1992; Pompei & Iovino 2012). From this perspective, it is expected that the abundance of compact groups increases with redshift.

However, the redshift-dependence has not yet been reported. Using a spectroscopic complete sample of 332 compact groups, Sohn et al. (2015) found that the abundance of compact groups changes little with redshift at $0.01 < z < 0.22$. Diaferio et al. (1994) suggested that compact groups replenish themselves with new members from the surrounding environment, thereby extending their lifetimes. This replenishment model can explain the lack of redshift-dependence of the abundance of compact groups. However, as of yet, there is no observational evidence supporting the replenishment model.

In order to prove the replenishment model, we need to first study where compact groups are located. Many studies found that more than half of compact groups are embedded in or associated with larger-scale structures (de Carvalho et al. 1994; Ramella et al. 1994; Rood & Struble 1994; Ribeiro et al. 1998; Mendel et al. 2011; Pompei & Iovino 2012). However, we note that most previous studies used compact group catalogs suffering from some observational biases. The observational biases are attributed to the widely used Hickson's selection criteria (Hickson 1982). The Hickson's selection criteria of compact groups are as follows.

1. Population criterion: $N(\Delta m < 3) \geq 4$, where the $(\Delta m < 3)$ indicates that the number of galaxies with brightness difference of < 3 magnitudes from the brightest galaxy.

2. Isolation criterion: $\theta_{\mathrm{N}} = 3\theta_{\mathrm{G}}$ & $N(\theta = [\theta_{\mathrm{N}}, \theta_{\mathrm{G}}]) = 0$, where θ_{G} is the angular distance from the group center to the farthest member galaxy, and θ is the angular distance from the group center.

3. Compactness criterion: $\bar{\mu} \leq 26.0$ mag arcsec^{-2}, where $\bar{\mu}$ denotes the surface

brightness within $\theta < \theta_G$ in red-band (E) in the Palomar Observatory Sky Survey (POSS) data.

Using these selection criteria, Hickson (1982) identified 100 compact groups. These selection criteria were also applied to several large-scale surveys; COSMOS/UKST Southern Galaxy Catalog (Prandoni et al. 1994), the Digitized Second POSS data (Iovino et al. 2003; de Carvalho et al. 2005), the two micron all sky survey data (Díaz-Giménez et al. 2012), the SDSS Data Release 4 (Lee et al. 2004) and the SDSS Data Release 6 (McConnachie et al. 2009).

Currently, the largest sample of compact groups is the catalog constructed by McConnachie et al. (2009). This catalog includes 77,088 compact groups and their 313,508 tentative member galaxies. The reason why these 313,508 galaxies are tentative members is because this catalog is based only on photometric information following Hickson's selection criteria. In fact, McConnachie et al. (2009)'s catalog is highly contaminated with interlopers ($> 50\%$, Mendel et al. 2011; Sohn et al. 2013). To reduce this contamination, we need to reject chance projections of galaxies along the line-of-sight by using spectroscopic redshifts.

Sohn et al. (2015) complied the spectroscopic redshifts from Fred Lawrence Whipple Observatory (FLWO)/FAST observations and from the SDSS Data Release 12 (DR12, Alam et al. 2015) for photometric sample of tentative compact group members in McConnachie et al. (2009). Sohn et al. (2015)'s catalog is a spectroscopically complete sample, but their sample is not free from an issue caused by the Hickson's isolation criterion.

Hickson (1982) identified their compact groups when there is no galaxy satisfying $\Delta m < 3$ magnitudes in $\theta = [\theta_N, \theta_G]$ annulus for each compact group. They adopted this isolation criterion in order to avoid selecting very dense regions such as cluster cores. However, this isolation criterion inevitably leads to a selection bias that misses nearby compact groups with apparently large angular sizes and embedded compact

groups in dense environments (Barton et al. 1996).

Recently, Sohn et al. (2016) published a new catalog of 1588 compact groups and their member galaxies at $0.01 < z < 0.19$ using SDSS DR12 spectroscopic data supplemented with additional redshifts from the literature and from FLWO/FAST observations (Sohn et al. 2015). They applied a friends-of-friends algorithm to identify compact groups without using the isolation criterion. By not applying the isolation criterion, the new catalog successfully contains nearby compact groups and embedded compact groups in high-density regions. This catalog helps us study the relationship between compact groups and their surrounding environments without any sample bias.

Johnson et al. (2007) and Walker et al. (2010, 2012) found that compact groups galaxies exhibit a bimodal distribution in the *Spitzer* IRAC $3.6 - 8.0$ μm color space with a statistically evident gap, so-called "MIR canyon". They showed that this gap is not found in comparison samples from the field, interacting galaxies, or cluster galaxies. These results suggest that galaxy evolution is accelerated in compact groups. However, these results are based on the catalogs of compact groups selected using the Hickson's selection criteria, which can introduce sample bias. Therefore, in Chapter 3, we revisit the issues on how fast galaxy evolution is in compact groups compared to other environments and how the evolution of compact groups is affected by their surrounding environment, using the unbiased sample of compact groups from Sohn et al. (2016) and the *WISE* data.

1.5   Galaxies in Transition, E+A Galaxies

Post-starburst, or "E+A" galaxies are characterized by unusual spectra with strong Balmer absorption lines (e.g., Hδ, Hγ, and Hβ) and no significant emission lines (e.g., [OII] and Hα). Strong Balmer absorption lines indicate the presence of a large population of A stars, while a lack of emission lines indicate the absence of current

star formation. The spectra of post-starburst galaxies reveal that these galaxies must have undergone a phase of vigorous starburst which was abruptly quenched within the last 1 Gyr (Dressler & Gunn 1983; Couch & Sharples 1987; Newberry et al. 1990). Dressler & Gunn (1983) identified three E+A galaxies, for the first time, using the spectra of 26 galaxies in the field of the 3C 295 galaxy cluster ($z =$ 0.45), obtained with the PFUEI Spectrograph mounted on the 5m Hale telescope on Palomar Mountain. Couch & Sharples (1987) suggested that E+A galaxies are descendants of blue galaxies found in distant clusters (Butcher & Oemler 1978).

The unusual E+A spectra inevitably pose several questions of where E+A galaxies form, and what mechanisms are responsible for the formation of E+A galaxies. At intermediate redshifts ($z = 0.3 - 0.6$), several studies reported that the fraction of E+A galaxies is higher in clusters than in field (Dressler et al. 1999; Tran et al. 2004), which might suggest that cluster-driven mechanisms (e.g., interactions between intracluster medium and infalling galaxies) are responsible for triggering E+As (Poggianti et al. 2004, 2009; Yagi et al. 2007). However, Balogh et al. (1999) found a similarly low E+A galaxy fraction in both clusters and the field at $0.18 < z < 0.55$. At $z < 0.1$ universe, many studies found that E+A galaxies are rare in clusters, and that a large fraction of E+A galaxies reside in the field (e.g., Zabludoff et al. 1996; Blake et al. 2004), suggesting that interactions with the cluster environment are not essential for the formation of E+A galaxies.

Zabludoff et al. (1996) found clear tidal features in at least five E+As using the images of 21 E+As from the STScI Digitized Sky Survey, and argued that galaxy-galaxy interactions and mergers are responsible for the E+A formation. This argument was confirmed in Yang et al. (2004, 2008) who presented disturbed morphologies of E+A galaxies using high-resolution HST images. They showed that most E+A galaxies have early-type morphologies with low surface brightness tidal features. They also reported that most E+As have large bulge-to-total light ratios

and high Sersic indices ($n \gtrsim 4$), characteristics of elliptical galaxies, but that E+As have larger asymmetry indices than ellipticals and stand apart from ellipticals in the fundamental plane. All these results lead us to draw the conclusion that galaxy-galaxy interactions and mergers are at least one mechanism for producing the E+A phase, and that E+A galaxies are in a transition phase between gas-rich star-forming galaxies and "red and dead" early-type galaxies.

Many numerical simulations showed that the E+A phase begins during or after the starburst phase in gas-rich major mergers (e.g., Hopkins et al. 2008; Snyder et al. 2011), which supports the merger-driven mechanism (Zabludoff et al. 1996; Yang et al. 2004, 2008). During a gas-rich major merger, tidal torques drive gas inflows to the galactic center, triggering a compact central starburst (e.g., Barnes & Hernquist 1992, 1996; Mihos & Hernquist 1996). As a result of the compact starbursts, the young stellar population (A stars) is expected to be confined within the galactic center, at $\lesssim 1$ kpc scales (Bekki et al. 2005; Hopkins et al. 2008, 2009). If this prediction is correct, the Balmer absorption lines should be enhanced at the galactic center, from which a steep radial gradient of the Balmer absorption line strength should be observed.

However, observational studies of E+A galaxies reveal conflicting results regarding the observed distribution of A stars formed in the recent starburst, as traced by strong Balmer absorption lines. Norton et al. (2001) investigated the spatial distribution of young ($\lesssim 1$ Gyr) stellar populations in E+A galaxies using long-slit spectroscopy of 20 E+As at $z \leq 0.13$, drawn from the Las Campanas Redshift Survey data. They found that although the young stellar populations are more centrally concentrated than the old ($\gtrsim$few Gyr) stellar populations, they are not confined to the galaxy core region ($\lesssim 1$ kpc). Yagi & Goto (2006) obtained similar results using long-slit spectroscopy of three E+As at $0.04 < z < 0.09$. Swinbank et al. (2012) analyzed GMOS IFU spectroscopy of 11 E+As at $0.06 < z < 0.12$, and found that

A stars tend to be widely distributed within the E+As, on average $\sim$33% of the galaxy image and extending over area $2 - 15$ kpc^2. This extended E+A signature has also been found in several integral field unit (IFU) studies(Pracy et al. 2005, 2009; Chilingarian et al. 2009). These results suggest that A stars were formed not only in nuclear regions but also in outer regions, contrary to predictions from numerical simulations.

Interestingly, Pracy et al. (2013) found a centrally concentrated distribution ($\lesssim 1$ kpc) of A stars in four nearby E+As ($0.019 < z < 0.034$), which is consistent with predictions from previous simulations, through GMOS IFU spectroscopy. Pracy et al. (2013) argued that the previous studies failed to detect Balmer line gradients within the central 1 kpc regions because the higher ($z \sim 0.1$) redshift E+A galaxies in the previous studies are too far to resolve the central 1 kpc region spatially given ground-based seeing.

To verify Pracy et al. (2013)'s argument, we need more local E+As with IFU data. Thus, we conducted GMOS-North IFU observations (ID: GN-2015B-Q-15, PI: Gwang-Ho Lee) of five E+As at $z \simeq 0.04$, similar to those of Pracy et al. (2013)'s targets. In Chapter 4, we address whether A stars in the five E+As are centrally concentrated or not.

1.6   Properties of Barred Galaxies and Environment

Stellar bars are common in spiral galaxies. The fraction of barred galaxies among spiral galaxies is about 30% (Sandage & Tamman 1981; de Vaucouleurs et al. 1991; Nair & Abraham 2010a; Masters et al. 2010; Lee et al. 2012a) in local universe. If weak bars are included, the bar fraction increases to $\sim$45$-$60% (Reese et al. 2007; Sheth et al. 2008; Barazza et al. 2008; Aguerri et al. 2009; Ann & Lee 2013). By removing the angular momentum of gas from the outer disk, bars deliver gas from the outer disk to the nuclear region (e.g., Lynden-Bell 1979; Sellwood 1981; Combes

& Gerin 1985; Bournaud & Combes 2002; Athanassoula 2003), which plays a crucial role in forming of bulges or pseudo-bulges (e.g., Combes & Sanders 1981; Pfenniger 1984; Hasan & Norman 1990; Norman et al. 1996; Shen & Sellwood 2004; Kormendy & Kennicutt 2004; Sheth et al. 2005; Bournaud et al. 2005; Athanassoula et al. 2005) and igniting central starburst (e.g., Heckman 1980; Quillen et al. 1995; Ho et al. 1997; Hunt & Malkan 1999; Sakamoto et al. 1999; Eskridge et al. 2000; Jogee et al. 2005; Marinova & Jogee 2007; Seo & Kim 2013, 2014). Furthermore, bars are thought to have an important role in fueling AGN (e.g., Shlosman et al. 1989; Ho et al. 1997; Thakur et al. 2009; Kim & Elmegreen 2017).

In differentially rotating disk structures, bars can be formed by non-axisymmetric perturbations (Hohl 1971; Ostriker & Peebles 1973). Many simulations focused on how the bar formation depends on disk dynamics and interactions with the dark halo (e.g., Sellwood & Wilkinson 1993; Athanassoula 2002; Athanassoula & Misiriotis 2002): these studies suggested that bars are difficult to be generated either if the disk is dynamically too hot, or if the disk mass is too small. Interactions between the dark matter halo and baryons in the disk regulate the bar instability, so that it affects the timescale of bar formation.

On the other hand, other simulations suggested that bars can be induced by galaxy interactions or mergers (e.g., Noguchi 1988; Gerin et al. 1990; Byrd & Valtonen 1990; Berentzen et al. 2004; Elmegreen 2005; Romano-Díaz et al. 2008; Aguerri & González-García 2009; Łokas et al. 2016). Some early observational studies found that the fraction of barred galaxies is larger in clusters than in less-dense environments (Thompson 1981; Eskridge et al. 2000; van den Bergh 2002), which is consistent with the expectation from numerical simulations. However, the environmental dependence of the bar fraction was not found in later studies using a large number of galaxies drawn from the SDSS (Aguerri et al. 2009; Li et al. 2009; Méndez-Abreu et al. 2010; Cameron et al. 2010; Barway et al. 2011).

In Lee et al. (2012a), we investigated the dependence of the bar fraction on galaxy properties and environment to understand how the existence of bars is related with the physical properties of host galaxies and what kind of environmental conditions bars prefer. We used a volume-limited sample of 33,391 galaxies with $M_r < -19.5$ and $0.02 \leq z \leq 0.05489$, drawn from the SDSS DR7. We classified early-type (E/S0) and late-type galaxies (S/Irr) using the automated method introduced by Park & Choi (2005). They found that the $u-r$ color versus $g-i$ color gradient and the $u-r$ color versus i-band concentration index diagrams are useful to classify galaxies into early and late types. The reliability and completeness of this automated method is $\sim$ 90%. To improve the accuracy of morphology classification, we performed additional visual inspection. Morphology information given by this scheme has been used in many studies (e.g., Park et al. 2007, 2008; Park & Hwang 2009; Park & Choi 2009; Hwang & Park 2009; Hwang et al. 2012a,b; Ko et al. 2009, 2012, 2013, 2014; Sohn et al. 2013, 2015, 2016). Our studies (Lee et al. 2012b, 2015, 2017) to be introduced in Chapters 2−5 also adopted this morphology information or the classification scheme.

We also identified bars through visual inspection. For late-type galaxies, we adopted an i-band isophotal axis ratio limit, $b/a > 0.6$, to reduce the internal extinction effects and the selection bias due to the inclination. The number of late-type galaxies with $b/a > 0.6$ is 10,674. Among them, we found 3240 barred galaxies with 2542 strong bars and 698 weak bars. When considering both strong and weak bars, the bar fraction is 30.4%. This bar classification has been used in several papers (Cervantes-Sodi et al. 2012, 2013; Cervantes Sodi et al. 2015; Cervantes Sodi 2017; Lin et al. 2014) including Lee et al. (2012b).

Lee et al. (2012a) found that the bar fraction strongly depends on the $u-r$ color and the velocity dispersion (or mass) of host galaxies. The bar fraction increases as $u-r$ increases and peaks at intermediate velocity dispersion ($\sigma \simeq 150$ km s^{-1}). If $u-r$ or velocity dispersion is fixed, the bar fraction does not depend on background

density. These results suggest that color and velocity dispersion are more influential parameters than background density in determining the bar fraction, and that background density does not play a direct role in bar formation and evolution. Lee et al. (2012a) also found that the bar fraction decreases as the distance to the nearest neighbor galaxy becomes smaller than 0.1 times the virial radius of the neighbor galaxy. This result suggests that it is difficult for barred galaxies to maintain their bars during strong tidal interactions or mergers. In conclusion, we did not find any direct evidence for environmental contribution to the bar formation. Similar results were reported in Casteels et al. (2013) and Lin et al. (2014).

On the other hand, it is still an open question whether or not bars trigger AGN. Bar-driven gas inflow has been considered as a mechanism for triggering AGN (Combes 2003). For the past three decades, many efforts has been devoted to understanding the connection between bars and AGN (e.g., Shlosman et al. 1989; Hopkins & Quataert 2010). However, it is not yet clear whether bars transport gas down to vicinity of supermassive black holes (Arsenault 1989; Moles et al. 1995; Laine et al. 2002; Ho et al. 1997; Laurikainen et al. 2004). Some studies suggested that nuclear spirals (Mulchaey & Regan 1997; Maciejewski & Sparke 1997; Ho et al. 1997) and secondary gaseous bars (Martini & Pogge 1999; Márquez et al. 2000; Martini et al. 2003) are responsible for triggering AGN. In Chapter 5, we use a $\sim$9000 late-type galaxies and their bar classification (Lee et al. 2012a) to investigate the connection between the presence of bars and AGN.

1.7 Purpose of this Thesis

In this thesis, we try to address the issues of which environmental mechanisms trigger galaxy transition from star-forming into quiescent, and what happens during the galaxy transition phase. We investigate the multi-wavelength properties of galaxies in a full range of environments to understand the environmental effects on galaxy

transition. We deal with interesting environments such as the A2199 supercluster and compact groups. We also investigate the stellar populations in E+A galaxies. Furthermore, we investigate whether stellar bars are a favorable environment for triggering AGN. We use multi-wavelength photometric and spectroscopic data drawn from several large-scale surveys (SDSS, *WISE*, and *GALEX*) and our observations with the Gemini-North 8m telescope.

This thesis consists of six chapters. Chapter 2 presents a study of the multi-wavelength properties of galaxies located in the A2199 supercluster. We address how galaxy properties depend on environment. We also present a new galaxy classification scheme in MIR color-luminosity diagram with a definition of the MIR green valley. In Chapter 3, we present a MIR view of galaxy evolution in compact groups using a recently published catalog of compact groups identified by a friends-of-friends algorithm (Sohn et al. 2016). Chapter 4 presents the two-dimensional distribution of young stellar populations in E+A galaxies, obtained from GMOS/IFU spectroscopy of five nearby E+A galaxies. Chapter 5 presents the connection of the presence of bars and AGN, using a volume-limited ($M_r < -19.5$ and $0.02 \leq z \leq 0.05489$) sample of galaxies (Lee et al. 2012a), drawn from the SDSS DR7. Summary and conclusions of this thesis are presented in Chapter 6.

Chapter 2

Galaxy Evolution in the MIR Green Valley: A Case of the A2199 Supercluster

(This chapter is published in the Astrophysical Journal.)[1]

2.1 Introduction

Color bimodality of galaxies appears in several wavelengths including the optical (Strateva et al. 2001; Baldry et al. 2004; Choi et al. 2007), ultraviolet (Wyder et al. 2007; Brammer et al. 2009), and MIR bands (Johnson et al. 2007; Walker et al. 2013). In optical color-magnitude diagrams galaxies are often separated into two classes: a red sequence and a blue cloud. The evolution between the two populations is one of the key issues in the recent study of galaxy formation and evolution (Faber et al. 2007; Tinker et al. 2013).

Galaxies in a region between the red sequence and the blue cloud (i.e., green

---

valley) seem to be an important population to understand this evolution. They might be in a transition phase from the blue cloud toward the red sequence; the transition would occur during a short timescale less than 1 Gyr (Springel et al. 2005; Faber et al. 2007; Pan et al. 2013). Recently, Schawinski et al. (2014) suggested that the green valley galaxies are not in a single transitional state from the blue cloud toward the red sequence. They found that early- and late-type galaxies in the green valley of optical color-mass diagrams have significantly different ultraviolet−optical colors. They pointed out that this color difference could be explained by different quenching timescales of star formation; quenching timescale for early-type galaxies (< 250 Myr) is much shorter than that for late-type galaxies (> 1 Gyr).

Galaxies can also be divided into several classes based on MIR colors such as AKARI $N3$ ($3.2\ \mu$m) $- S11$ ($10.4\ \mu$m) (Shim et al. 2011; Ko et al. 2012) and *Spitzer* IRAC $3.5\ \mu$m $- 8\ \mu$m (Johnson et al. 2007; Walker et al. 2013). These MIR colors are useful indicators of specific star formation rates (SFRs, Duc et al. 2002; Chung et al. 2011) and of mean stellar ages (Piovan et al. 2003; Temi et al. 2005; Ko et al. 2009). For example, Hwang et al. (2012a) studied the galaxies of the A2199 supercluster in the $[3.4] - [12]$ color versus $12\ \mu$m luminosity diagram using the *WISE* data. They found that early- and late-type galaxies are well separated into two groups; late-type galaxies with MIR red colors form the "MIR star-forming sequence", but early-type galaxies mainly form the "MIR blue cloud".

As in the optical color-magnitude diagrams, galaxies with intermediate MIR colors seem to be transition populations (e.g., Shim et al. 2011; Ko et al. 2012, 2013). Recently, Alatalo et al. (2014) defined the infrared transition zone in the *WISE* $[4.6] - [12]$ color space, and suggested that the galaxies in this zone are in the late stages of transition across the optical green valley. However, how this transition differs depending on galaxy morphology is not well understood. This is the goal of this study; we define "MIR green valley" galaxies in the MIR color-luminosity

diagram, and study their properties in connection to other populations.

On the other hand, galaxy properties including the star formation activity and the galaxy morphology are strongly affected by environment (Park et al. 2007; Blanton & Moustakas 2009). Galaxy clusters are an ideal place to study this environmental dependence of galaxy properties, and several physical mechanisms in the cluster environment have been proposed to explain the dependence: ram pressure stripping (Gunn & Gott 1972), thermal evaporation (Cowie & Songaila 1977), strangulation (Larson et al. 1980), galaxy harassment (Moore et al. 1996), starvation (Bekki et al. 2002), and cumulative galaxy-galaxy hydrodynamic/gravitational interactions (Park & Hwang 2009).

Some cluster galaxies might have experienced the environmental effects even before they enter the cluster regions. For example, Zabludoff & Mulchaey (1998) suggested that massive early-type galaxies are formed by galaxy-galaxy mergers in group-scale environment, and then fall into clusters later. The galaxy interactions and mergers should be very frequent and effective because of low velocity dispersion of galaxies in the group environment (Hickson et al. 1992; Sohn et al. 2013). This "pre-processing" in groups is supported by numerical simulations (Fujita 2004) and by observations (Koyama et al. 2011; Lemaux et al. 2012; Hess & Wilcots 2013; Mahajan 2013). Therefore, it is important to study the galaxies in galaxy groups to better understand the environment effects on galaxy properties.

Because superclusters of galaxies contain several clusters and groups, they can be excellent laboratories for studying the environmental dependence of galaxy properties in a full range of environment from cluster to field (e.g., Haines et al. 2011; Biviano et al. 2011). In this study, we use a multiwavelength catalog of the galaxies in the A2199 supercluster at $z = 0.03$ to study the MIR properties of galaxies and their environmental dependence. The main goal is to examine how the galaxies in the MIR green valley differ from other populations as a function of environment.

Section 2.2 describes the observational data we use. We derive physical parameters of the groups and clusters in the A2199 supercluster in Section 2.3. We investigate the dependence of mass-normalized integrated SFRs of galaxy groups and clusters on their virial masses in Section 2.4. We classify the galaxies in the MIR color-luminosity diagram, and study the environmental dependence of their MIR properties in Section 2.5. We discuss our results in Section 2.6, and conclude in Section 2.7. Throughout, we adopt flat ΛCDM cosmological parameters: $H_0 = 70 \ \mathrm{km \ s^{-1} \ Mpc^{-1}}$, $\Omega_\Lambda = 0.7$, and $\Omega_m = 0.3$.

2.2   Data

We used the galaxy catalog of the A2199 supercluster given by Hwang et al. (2012a). Hwang et al. (2012a) compiled the multi-wavelength data of the galaxies at $m_r < 17.77$ from the SDSS DR7 and the *WISE* data. The *WISE* provides all-sky survey data in four MIR bands (3.4, 4.6, 12, and 22 μm) with a much better sensitivity than previous infrared surveyors. Thus, the data cover the entire region of the A2199 supercluster at $z = 0.03$ ($12° \times 12° \simeq 27 \ \mathrm{Mpc} \times 27 \ \mathrm{Mpc}$).

Hwang et al. (2012a) selected member galaxies using the caustic method (Diaferio & Geller 1997; Diaferio 1999; Serra et al. 2011). They also compiled redshift data for the galaxies fainter than $m_r = 17.77$ from other large spectroscopic surveys (Rines et al. 2002; Rines & Geller 2008). However, these surveys cover only the central region ($R < 50$ arcmin) of the A2199 supercluster. Therefore, we did not use these faint galaxies, but used the galaxies at $m_r < 17.77$ to have a galaxy sample with uniform depth in the entire supercluster region. The final sample contains 1529 member galaxies including 559 early-type (E/S0) and 970 late-type galaxies (S/Irr).

Galaxy morphology information is mainly from the Korea Institute for Advanced Study (KIAS) DR7 value-added galaxy catalog (VAGC, Choi et al. 2010). The morphology information is based on the automatic classification by Park & Choi (2005),

which uses $u - r$ color, $g - i$ color gradient, and i-band concentration index. The completeness and reliability of this method are $> 90\%$. Hwang et al. (2012a) conducted an additional visual inspection to improve the classification results and to classify the galaxies not included in the KIAS DR7 VAGC. The detailed description of the galaxy catalog is in Hwang et al. (2012a).

All the 1529 member galaxies are detected at the *WISE* 3.4 and 4.6 μm with signal-to-noise ratio (S/N) ≥ 3. However, there are 1151 (75.3%) and 552 galaxies (36.1%) among the members detected at 12 and 22 μm with S/N ≥ 3, respectively. We provide physical parameters of the member galaxies used in this paper. Table 2.1 lists SDSS-related parameters, and Table 2.2 lists *WISE*-related parameters.

2.3 Galaxy Groups and Clusters in the A2199 Supercluster

The A2199 supercluster at $z = 0.03$ contains several galaxy groups and clusters. Rines et al. (2001, 2002) identified seven galaxy systems including three clusters (A2199, A2197W/E) and four X-ray bright groups (NRGs385, NRGs388, NRGs396, and the NGC 6159 group). They derived the physical parameters of these systems. Figure 2.6 displays the spatial distribution of three clusters and groups. The A2199 supercluster covers a wide range of environment: e.g., $-0.85 < \log\Sigma_5 \,(\text{Mpc}^{-2}) < 2.85$ if we define the environment by the galaxy surface number density (see Section 2.5.3 for details). The density range is wider than the range that we used in the study of A2255 (Shim et al. 2011).

A2199 is located in the center of the supercluster. It is a typical (rich and regular) cluster of galaxies in the nearby universe. The X-ray emission around A2199 is quite symmetric, suggesting that A2199 did not experience recent major merger (Rines et al. 2001). There is a cooling flow and a radio jet in A2199 (Markevitch et al.

Table 2.1. SDSS-related physical parameters of member galaxies

SDSS ObjID (DR7)	R.A. (J2000)	Decl. (J2000)	z	MC^a	$\log(M_{star}/M_{\odot})$	$u-r^b$	$\log SFR_{SDSS}$	D_n4000
587725992501969046	16:46:57.61	41:56:22.7	0.0327	2	9.703	1.075	1.288	1.257
587725992503017882	16:53:52.93	39:49:46.7	0.0338	1	9.816	2.543	0.035	1.655
587725992503017689	16:53:56.32	39:48:45.4	0.0332	1	10.794	2.876	0.049	1.961
587725992502820896	16:52:29.10	40:18:43.0	0.0292	1	10.765	2.857	0.140	2.006
587725993036939572	16:36:03.51	45:44:47.6	0.0309	2	10.524	2.027	1.188	1.750

Note. — ^{a} Morphology classification: 1- Early types (E/S0), 2- Late types (S/Irr). ^{b} Extinction-corrected $u-r$

Table 2.2. *WISE*-related physical parameters of member galaxies

WISE ID	$[3.4] - [12]$	$\log(L_{12\mu m}/L_\odot)$	$(S/N)_{12\mu m}$	MIRcl^a	$\log SFR_{WISE}$	$(S/N)_{22\mu m}$
J164657.63+415622.9	1.389	8.564	21.60	3	0.683	6.30
J165352.94+394946.7	-0.600	7.680	1.40	0	0.255	-1.70
J165356.33+394845.4	-1.879	8.106	8.40	1	0.404	3.30
J165229.09+401843.0	-1.934	8.096	11.40	1	0.311	1.20
J163603.52+454447.8	0.406	8.753	34.20	3	0.739	7.70

Note. — ^{a} MIR classification: 0- $(S/N)_{12\mu m} < 3$, 1- MIR blue cloud galaxies, 2- MIR green valley galaxies, 3- MIR star-forming sequence galaxies.

1999; Johnstone et al. 2002; Kawano et al. 2003), which may be associated with a cD galaxy, NGC 6166 (Kelson et al. 2002).

Because we have recent redshift data for the supercluster, we recalculate some physical parameters of these systems. For example, we compute the mean redshifts, v [km s^{-1}] (biweight location of Beers et al. 1990), using the galaxies at $R \leq 0.25$ h^{-1} Mpc of each system. The radius for computing the mean redshifts is small enough so that the galaxy systems do not overlap each other, as used in Rines et al. (2002). We also compute the projected velocity dispersions, σ_p [km s^{-1}] (biweight scale of Beers et al. 1990), using the galaxies at $R \leq 1.0$ h^{-1} Mpc. We use this radius, smaller than the one used in Rines et al. (2002) (i.e., 1.5 h^{-1} Mpc), to avoid the overlap between the systems. If we use $R = 1.5$ h^{-1} Mpc aperture, σ_p changes within the uncertainty.

Our estimates of v for the systems in the A2199 supercluster are in the range $8767 - 9507$ km s^{-1}; these agree well with previous measurements in Rines et al. (2002). On the other hand, our σ_p ranges from 244 km s^{-1} to 675 km s^{-1}; these are on average $\sim 20\%$ smaller than previous measurements in Rines et al. (2002). This difference seems to result mainly from the difference in the data. For example, σ_p of A2199 in this study is 675 ± 35 km s^{-1}. This is smaller than 796^{+38}_{-33} km s^{-1} in Rines et al. (2002), but is similar to 676^{+37}_{-32} km s^{-1} in Rines & Diaferio (2006) who used the same SDSS data. Table 2.3 lists our measurements of v and σ_p for each system.

To estimate the size of each system, we convert σ_p into R_{200} (approximately the virial radius) using the formula given in Carlberg et al. (1997). We then determine the virial mass (M_{200}) of each system using the $M_{200} - \sigma_p$ relation given in Rines et al. (2013): M_{200} [$10^{14} M_\odot$] $= 0.093 \times (\sigma_p/200)^{2.90 \pm 0.15}$. The derived values of R_{200} and M_{200} of A2199 are 1.65 ± 0.09 Mpc and $(3.16 \pm 0.48) \times 10^{14} M_\odot$, respectively. These values agree well with the estimates in Rines & Diaferio (2006): $R_{200} = 1.44$ Mpc and $M_{200} = (3.41 \pm 1.10) \times 10^{14}$ $M_\odot$. The M_{200} for other systems in the A2199

Table 2.3. Galaxy Groups/Clusters in the A2199 Supercluster

System	R.A.$_{2000}$ (J2000)	Decl.$_{2000}$ (J2000)	v [km s^{-1}]	σ_p [km s^{-1}]	R_{200} [degree]	R_{200} [Mpc]	M_{200} [$10^{14}\ M_\odot$]	$\log L_X$ [h^{-2} erg s^{-1}]
A2199	16:28:38	39:33:05	9140±135	675±35	0.73±0.04	1.65±0.09	3.16±0.48	44.1
A2197W	16:27:41	40:55:40	9482±144	537±22	0.58±0.02	1.31±0.05	1.63±0.19	42.5
A2197E	16:29:43	40:49:12	8767± 88	543±22	0.59±0.02	1.32±0.05	1.68±0.20	42.4
NRGs385	16:17:43	34:58:00	9321±100	426±21	0.46±0.02	1.04±0.05	0.83±0.12	42.8
NRGs388	16:23:01	37:55:21	9399±146	549±33	0.60±0.04	1.34±0.08	1.74±0.30	42.3
NRGs396	16:36:50	44:13:00	9507±110	244±33	0.26±0.04	0.60±0.08	0.17±0.07	42.0
NGC 6159	16:27:25	42:40:47	9397± 94	243±31	0.26±0.03	0.59±0.08	0.16±0.06	42.3

Note. — Right ascension and declination are mainly from Rines et al. (2001, 2002). In the cases of NRGs385 and the NGC 6159 group, their coordinates are taken from the NASA/IPAC Extragalactic Database. The uncertainties in v and σ_p are determined by the bootstrap re-sampling method.

supercluster are in the range $0.15 - 2 \times 10^{14}$ $M_\odot$, similar to the masses of galaxy groups at $z < 0.1$ (Rines & Diaferio 2010). Table 2.3 lists R_{200} and M_{200} of the groups and clusters in the A2199 supercluster.

2.4   Integrated SFRs of Galaxy Systems in the A2199 Supercluster

To study the dependence of the star formation activity of clusters on cluster mass, many studies have used the mass-normalized integrated SFRs of clusters (i.e., $\Sigma SFR/M_{200}$) as a proxy for the global SFRs (e.g., Finn et al. 2005; Geach et al. 2006; Bai et al. 2007, 2009; Chung et al. 2010; Koyama et al. 2010; Shim et al. 2011; Biviano et al. 2011; Chung et al. 2011). In this section, we study this dependence for the galaxy systems in the A2199 supercluster using the *WISE* data.

To compute the integrated SFR of each system, we use the SFRs of galaxies converted from total IR $(8 - 1000$ μm) luminosities $(L_{\rm IR})$. We compute the total IR luminosities of galaxies using the *WISE* 22 μm flux densities and the spectral energy distribution templates of Chary & Elbaz (2001). Following Hwang et al. (2012a), we use the relation in Kennicutt (1998) for the conversion of the total IR luminosities into SFRs with the assumption of a Salpeter (1955) initial mass function with a power law index $x = 2.35$: $SFR_{\rm WISE}$ $(M_\odot$ $yr^{-1}) = 1.72 \times 10^{-10}$ $L_{\rm IR}(L_\odot)$. These IR-based SFRs ($SFR_{\rm WISE}$) of galaxies agree well with those derived from the optical spectra (Hwang et al. 2012a,b; Lee et al. 2013).

To have a fair comparison with other studies (e.g., Finn et al. 2005; Bai et al. 2007, 2009), we first use the same selection criteria adopted in other studies to compute the integrated SFRs (i.e., $SFR_{\rm WISE} > 2$ $M_\odot$ yr^{-1} and $R \leq 0.5R_{200}$). We do not include active galactic nucleus (AGN)-host galaxies such as Seyferts, LINERs, Type I AGNs with broad Balmer lines (FWHM > 1000 R_{200}) and MIR-selected

AGNs ($[3.4] - [4.6] > 0.44$, Hwang et al. 2012a) because their L_{IR} (based on the *WISE* 22 μm flux densities) can be dominated by AGN rather than by star formation (Brand et al. 2009; Lee et al. 2012). However, we include composite galaxies because the AGN contribution to the 22 μm flux densities in these galaxies is small ($\sim 6\%$) (Lee 2012).

As listed in Table 2.4, we could obtain $\Sigma\mathrm{SFR}/M_{200}$ only for two galaxy systems: 4.78 ± 1.45 for A2199 and 1.97 ± 0.84 for A2197E in unit of 10^{-14} yr^{-1}. These values are similar to other clusters at similar redshifts (e.g., Coma and A1367, Bai et al. 2007). However, we could not determine $\Sigma\mathrm{SFR}/M_{200}$ for the other systems because there are no galaxies satisfying the selection criteria (i.e., $\mathrm{SFR_{WISE}} > 2\ M_\odot$ yr^{-1} and $R \leq 0.5R_{200}$). It also should be noted that $\Sigma\mathrm{SFR}/M_{200}$ for A2199 and A2197E are based only on a small number of galaxies (i.e., three and one galaxies for A2199 and A2197E, respectively).

Thus, we change the selection criteria to increase the sample size: $\mathrm{SFR_{WISE}} > 0.5\ M_\odot$ yr^{-1} and $R \leq 0.5R_{200}$. Most galaxies with $\mathrm{SFR_{WISE}} > 0.5\ M_\odot$ yr^{-1} are detected at 22 μm with $\mathrm{S/N_{22\mu m}} \geq 3$ (94%), suggesting no significant bias due to incompleteness. This limit is much lower than the one used in a recent study based on similar *WISE* data (e.g., $4.6\ M_\odot$ yr^{-1} in Chung et al. 2011).

Table 2.4 lists $\Sigma\mathrm{SFR}$ and $\Sigma\mathrm{SFR}/M_{200}$ of each system based on samples of galaxies with $\mathrm{SFR_{WISE}} > 0.5\ M_\odot$ yr^{-1}. We derive the values for two cases: $R \leq 0.5R_{200}$ and $R \leq R_{200}$. Figure 2.1(a) shows that $\Sigma\mathrm{SFR}/M_{200}$ for $R \leq 0.5R_{200}$ does not depend on M_{200}. Similarly, $\Sigma\mathrm{SFR}/M_{200}$ for $R \leq R_{200}$ in panel (b) does not show M_{200} dependence. The Spearman's coefficient for the data in panel (a) is -0.18, while that in panel(b) is 0.07. In addition, the probability of obtaining the correlation by chance is over 70% in the both case. These results suggest that there is no significant correlation between $\Sigma\mathrm{SFR}/M_{200}$ and M_{200}.
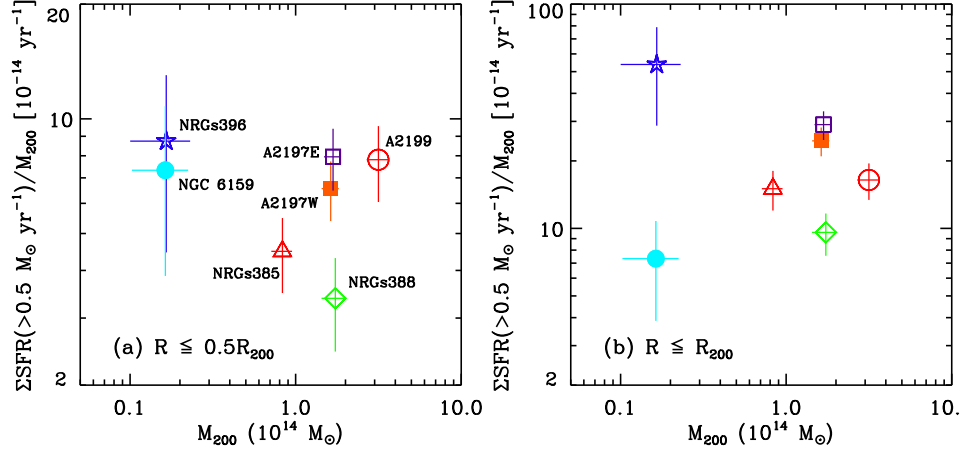
Figure 2.1 ΣSFR$/M_{200}$ for (a) $R \leq 0.5R_{200}$ and (b) $R \leq R_{200}$ of galaxy groups and clusters as a function of M_{200} using galaxies with SFR$_{\mathrm{WISE}} > 0.5$ $M_\odot$ yr^{-1}.

Table 2.4. ΣSFR and ΣSFR$/M_{200}$ of Groups/Clusters in A2199 Supercluster

Galaxy System		$R \leq 0.5R_{200}$			$R \leq R_{200}$	
	N_{gal}	ΣSFR (> 0.5) $[M_\odot$ yr$^{-1}]$	ΣSFR$/M_{200}$ $[10^{-14}$ yr$^{-1}]$	N_{gal}	ΣSFR (> 0.5) $[M_\odot$ yr$^{-1}]$	ΣSFR$/M_{200}$ $[10^{-14}$ yr$^{-1}]$
A2199	15	24.67 ± 4.16	7.81 ± 1.76	34	51.97 ± 5.56	16.44 ± 3.04
A2197W	12	10.68 ± 1.41	6.56 ± 1.17	33	40.01 ± 3.44	24.57 ± 3.61
A2197E	12	13.37 ± 1.90	7.95 ± 1.47	37	48.82 ± 4.24	29.03 ± 4.24
NRGs385	6	3.73 ± 0.63	4.49 ± 1.00	12	12.50 ± 1.77	15.03 ± 3.02
NRGs388	4	5.87 ± 1.25	3.38 ± 0.93	15	16.66 ± 2.05	9.60 ± 2.05
NRGs396	2	1.44 ± 0.42	8.74 ± 4.28	6	8.90 ± 2.22	53.83 ± 25.11
NGC 6159	2	1.20 ± 0.35	7.33 ± 3.46	2	1.20 ± 0.35	7.33 ± 3.46

2.5 MIR Properties of Galaxies in Galaxy Systems of the A2199 Supercluster

To compare the star formation activity of galaxy systems in the A2199 superclus-ter in detail, we investigate the MIR properties of the galaxies in each system in this section. We first divide galaxies into three MIR classes in the MIR color-luminosity diagram (Section 2.5.1), and then compute the fraction of galaxies in each MIR class for the galaxy groups/clusters in the A2199 supercluster (Section 2.5.2). We also ex-amine the environmental dependence of the MIR properties of galaxies in Section 2.5.3.

2.5.1 Galaxy Classification in the MIR Color-Luminosity Diagram

The MIR colors such as $AKARI\ N3 - S11$ or $WISE$ $[3.4] - [22]$, $[4.6] - [12]$ are useful indicators of the specific SFRs and of the presence of intermediate-age stellar populations (e.g., Lee et al. 2009; Ko et al. 2009, 2012, 2013; Shim et al. 2011; Donoso et al. 2012; Hwang et al. 2012a). $WISE$ $[3.4] - [12]$ colors are also a good indicator of the specific SFRs because 3.4 and 12 μm luminosities, respectively, trace stellar masses and SFRs (Donoso et al. 2012; Hwang et al. 2012b). The other $WISE$ colors including $[4.6] - [12]$, $[3.4] - [22]$, and $[4.6] - [22]$ can also be used. However, we use $[3.4] - [12]$ in this study because 3.4 μm probes the old stellar components better than than 4.6 μm, and 12 μm sensitivity is better than 22 μm.

The left panels in Figure 2.2 show the distribution of galaxies in the $[3.4] - [12]$ versus 12 μm luminosity diagram. As shown in Hwang et al. (2012a), late-type star-forming galaxies form a linear "MIR star-forming sequence", while most early-type galaxies form a "MIR blue cloud" with low 12 μm luminosities. For robust classification of the galaxies in this diagram, we use a large sample of SDSS galaxies at $0.025 < z < 0.035$ including the A2199 supercluster galaxies. The contours in
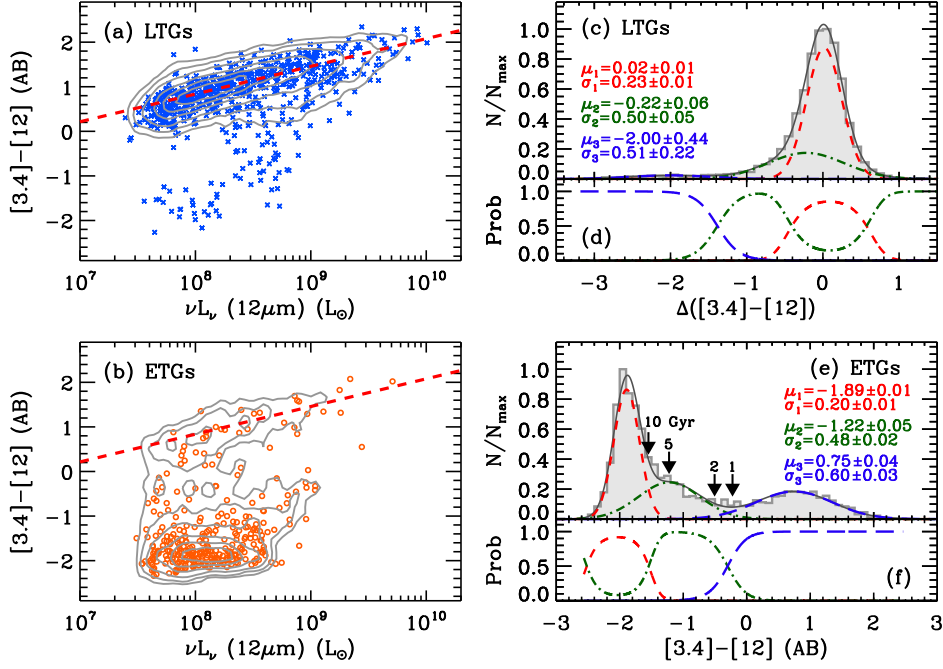
Figure 2.2 (a) MIR color-luminosity diagram for (a) late-type and (b) early-type galaxies. Contours represent number density distribution of galaxies at $0.025 < z < 0.035$, while color symbols are member galaxies in the A2199 supercluster. Dashed lines are the "MIR star-forming sequence" that is a linear fit for late-type galaxies with star-forming nuclei, which is defined in Hwang et al. (2012a). (c) Histogram of $\Delta([3.4] - [12])$, the deviation of $[3.4] - [12]$ from the MIR star-forming sequence fit, for late-type galaxies. We use the Gaussian mixture modeling (GMM, Muratov & Gnedin 2010) to decompose the histogram with multi-Gaussian functions. We overplot three Gaussians and their sum, and list the mean and standard deviation of each Gaussian. (d) the probability distribution from the GMM that indicates which Gaussian galaxies should belong to. (e) Histogram of $[3.4] - [12]$ for early-type galaxies, and three Gaussians and the sum obtained from the GMM. Arrows represent the predicted $[3.4] - [12]$ colors of early-type galaxies with different mean stellar ages from the SSP models (Piovan et al. 2003). (f) The Probability of $[3.4] - [12]$ belonging to each Gaussian.

Figure 2.2(a) and (b) indicate the number density distributions of early- and late-type galaxies, respectively. The linear fit to this large galaxy sample gives a relation,

$$[3.4] - [12] = \log(\nu L_\nu(12\mu\text{m})) \times (0.62 \pm 0.01) - (4.13 \pm 0.05). \qquad (2.1)$$

This relation is similar to the one derived in Hwang et al. (2012a), but based on a much larger sample.

We plot the distribution of vertical offsets of late-type galaxies from the MIR star-forming sequence, $\Delta([3.4] - [12])$, in panel (c). The histogram is negatively skewed. We use the Gaussian mixture modeling (GMM, Muratov & Gnedin 2010) to decompose the histogram with multi-Gaussian functions. The histogram is well described by the sum of three Gaussians rather than the sum of two Gaussians. We overplot the three Gaussians with their sum, and list the mean and standard deviation of each Gaussian.

Figure 2.2(d) shows the probability distribution from the GMM that indicates which Gaussian galaxies should belong to. At $\Delta([3.4] - [12]) < -1.38$, the probability that galaxies belong to the left Gaussian (long-dashed line) is larger than 50%. At $-1.38 < \Delta([3.4] - [12]) < -0.41$, the probability that galaxies belong to the middle Gaussian is over 50%. We adopt $\Delta([3.4] - [12]) = -1.38$ to separate the galaxies in the left tail from the majority of late-type, star-forming galaxies.

On the other hand, the majority of early-type galaxies are distributed around $[3.4] - [12] = -2$, which is the MIR blue cloud. Some early-type galaxies have MIR colors, much redder than the MIR blue cloud. Figure 2.2(e) shows the distribution of $[3.4] - [12]$ colors for early-type galaxies at $0.025 < z < 0.035$. The histogram is well described by the sum of three Gaussians. The Gaussian in the left covers a narrow color range centered at $[3.4] - [12] \simeq -1.9$ (i.e., MIR blue cloud). The Gaussians in the middle and right are for those in the green valley (to be defined in this section) and in the MIR star-forming sequence, respectively.

We overplot the predicted $[3.4] - [12]$ colors from the single stellar population

models (SSP) of Piovan et al. (2003). This model considers the MIR emission from dusty circumstellar envelops of asymptotic giant branch stars when constructing spectral energy distribution of early-type galaxies. Four arrows indicate mean stellar ages of 1, 2, 5, and 10 Gyr ($[3.4] - [12] = -0.22, -0.51, -1.22$, and -1.55). This suggests that the Gaussian in the left mainly traces the galaxies with stellar populations older than 10 Gyrs, while the Gaussian in the middle traces the galaxies with intermediate-age stellar populations.

To separate the early-type galaxies with intermediate and old stellar populations, we adopt a cut of $[3.4] - [12] = -1.55$ that corresponds to the color of 10 Gyr stellar populations. This color cut is the one where the probability that the galaxies belong to the Gaussian in the left becomes larger than 50%, as shown in panel (f).

Based on the results in Figure 2.2, we divide the galaxies into three MIR classes in the MIR color-luminosity diagram as shown in Figure 2.3. We use two demarcation lines, $\Delta([3.4] - [12]) = -1.38$ from the MIR star-forming sequence and $[3.4] - [12] = -1.55$. We call the galaxies at $\Delta([3.4] - [12]) > -1.38$ from the MIR star-forming sequence "MIR star-forming sequence galaxies", and those with $[3.4] - [12] < -1.55$ "MIR blue cloud galaxies". Then the galaxies between the two lines are "MIR green valley galaxies".

Among 997 member galaxies in this diagram, the number of MIR star-forming sequence, MIR green valley, and MIR blue cloud galaxies are 678 (68.0%), 126 (12.6%), and 193 (19.4%), respectively. The majority (93%, 628/678) of MIR star-forming sequence galaxies are morphologically late types. In contrast, MIR blue cloud galaxies are mainly (90%, 174/193) early types. Two-thirds of MIR green valley galaxies are early-type galaxies (68%, 86/126), and one third of them are late types (40/126).

To compare the MIR classification with that in the optical bands, we plot the galaxies in each MIR class in the optical color-mass diagram. Figure 2.4 shows an extinction-corrected $u - r$ color as a function of stellar mass. To correct for dust
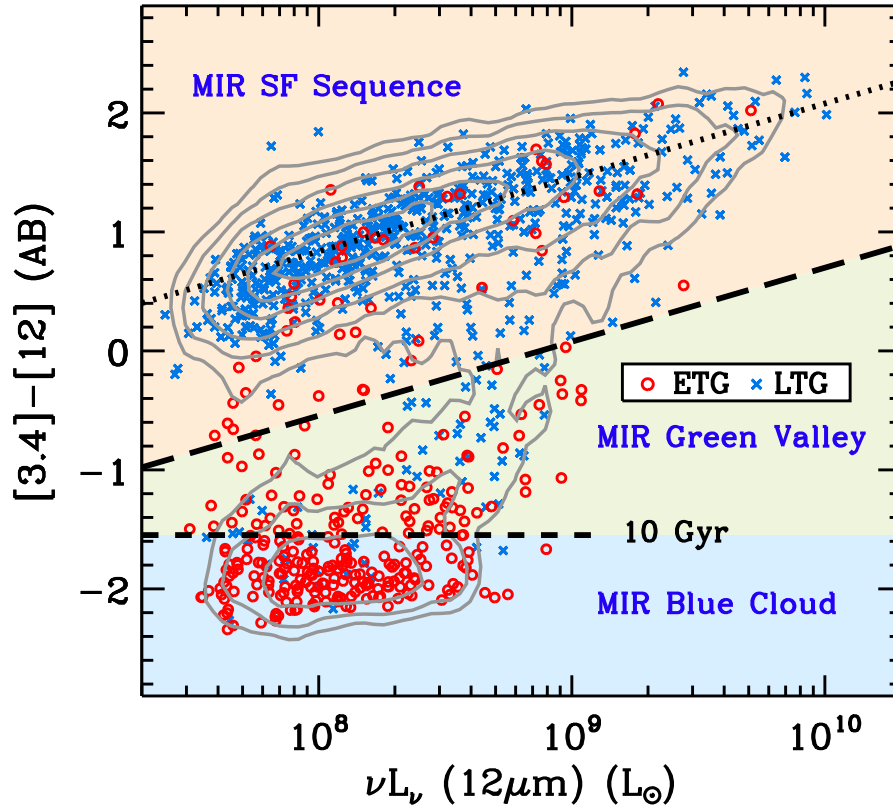
Figure 2.3 MIR color-luminosity diagram for galaxies with $S/N_{12\mu m} \geq 3$. Contours represent the number density distribution of galaxies at $0.025 < z < 0.035$, while circles and crosses are early- and late-type member galaxies of the A2199 supercluster, respectively. We divide galaxies into three classes: MIR star-forming sequence galaxies, MIR green valley galaxies, and MIR blue cloud galaxies. Long and short dashed lines are demarcation lines for this MIR galaxy classification. The latter corresponds to the the color of 10 Gyr stellar populations (Piovan et al. 2003). A dotted line indicates a linear fit for the MIR star-forming sequence.

extinction, we use E(B-V) values from the stellar continuum fits of Oh et al. (2011) and apply the reddening law of Cardelli et al. (1989). Grayscale contours indicate the number density of the SDSS galaxies at $0.025 < z < 0.035$. Two dashed lines define the optical green valley adopted from Schawinski et al. (2014).

As expected, MIR star-forming sequence galaxies are mainly distributed in the optical blue cloud (see panel c). Some of them are in the optical green valley. MIR blue cloud galaxies are distributed in the optical red sequence (panel a). Interestingly, the majority of MIR green valley galaxies roughly follow the optical red sequence despite a scatter in color (panel b). These are consistent with the results in other studies (Ko et al. 2012; Walker et al. 2013).

The stellar mass range of MIR green valley galaxies is nearly the same as that of MIR blue cloud galaxies (log $(M_{\mathrm{star}}/M_{\odot}) > 10$). This means that the discrimination between MIR blue cloud and MIR green valley galaxies based only on optical parameters is difficult. It is interesting to note that the MIR green valley galaxies are not the same as the optical green valley galaxies. The optical green valley galaxies are included in the MIR star-forming sequence class. Panels (a-c) also show that the distributions of early- and late-type galaxies in each panel are not significantly different.

In panel (d) we plot the distribution of 12 μm undetected galaxies (i.e., S/N$_{12\mu\mathrm{m}}$ < 3); they are not included in the MIR classification. They are distributed either in the optical blue cloud or in the red sequence. They appear to have stellar masses lower than other MIR classes in a fixed morphology. The majority ($\sim 80\%$) of the 12 μm undetected galaxies have no strong emission lines in their optical spectra; most of their spectral types are undetermined. These results suggest that they are a mixture of young galaxies with small stellar masses and of relatively massive galaxies that are quiescent; both of them have 12 μm flux densities, not high enough to be detected with *WISE*.
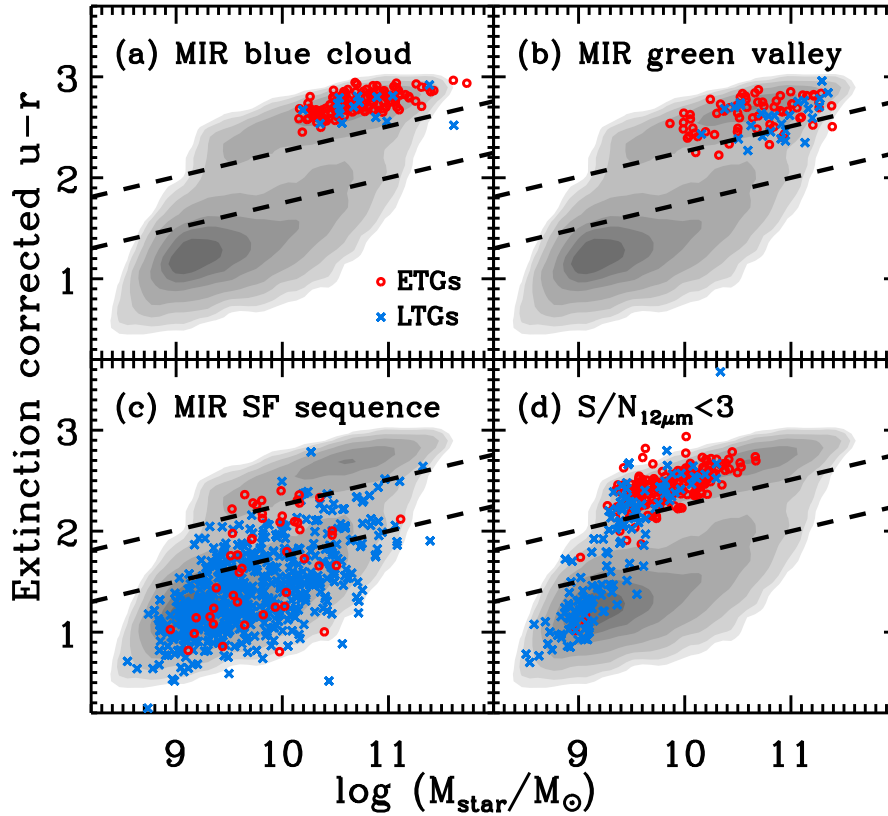
Figure 2.4 The extinction-corrected $u - r$ color vs. stellar mass diagram. Gray contours represent the number density distribution of galaxies at $0.025 < z < 0.035$. Circles and crosses represent early- and late-type A2199 supercluster members segregated by their MIR classes: (a) MIR blue cloud galaxies, (b) MIR green valley galaxies, (c) MIR star-forming sequence galaxies, and (d) 12 μm undetected galaxies ($S/N_{12\mu m} < 3$). Dashed lines indicate the optical green valley defined in Schawinski et al. (2014).
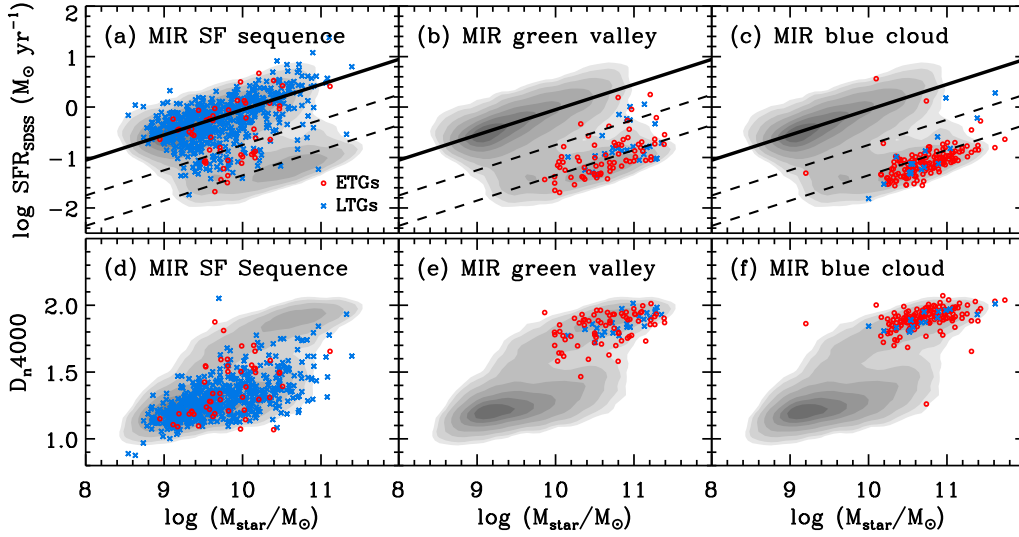
Figure 2.5 Top: stellar mass vs. SFR$_{SDSS}$ diagram. Contours represent number density distribution of galaxies at $0.025 < z < 0.035$. Circles and crosses represent early- and late-type member galaxies of the A2199 supercluster segregated by their MIR classes: (a) MIR star-forming sequence galaxies, (b) MIR green valley galaxies, and (c) MIR blue cloud galaxies. Solid lines are the linear fit to galaxies with star-forming nuclei, while dashed lines indicate 1/5 and 1/20 levels, respectively. Bottom: stellar mass vs. D_n4000 distribution of (d) MIR star-forming sequence, (e) MIR green valley, and (f) MIR blue cloud galaxies.

We also show the galaxies in each MIR class in the plot of SFR derived in the optical band and stellar mass (see top panels of Figure 2.5). We use SFR$_{SDSS}$ adopted from the MPA/JHU DR7 value-added galaxy catalog (Brinchmann et al. 2004). The grayscale number density contours based on the galaxies at $0.025 < z < 0.035$ show two distinctive sequences. The upper sequence (solid lines) is for star-forming galaxies, which is called a "main sequence" of star-forming galaxies (Noeske et al. 2007; Elbaz et al. 2011). The lower sequence is for those with SFRs much smaller than the main sequence galaxies.

As expected, MIR star-forming sequence galaxies are well distributed along the main sequence (panel a). In contrast, MIR blue cloud galaxies are on the sequence in the bottom. Similarly, MIR green valley galaxies are mainly found on the sequence in the bottom. The SFRs of MIR green valley galaxies appear to be slightly higher than those for MIR blue cloud galaxies in a give stellar mass. However, the difference is not significant.

We also examine the distribution of D_n4000 for the three MIR classes in bottom panels. The D_n4000 is a useful measure of mean stellar age of galaxies (Balogh et al. 1999; Shim et al. 2011). Galaxies with $D_n4000 < 1.5$ contain young stellar populations with $\lesssim 1$ Gyr (Kauffmann et al. 2003a). On the other hand, D_n4000 larger than 1.5 indicates mean stellar age larger than 1 Gyrs (Kranz et al. 2010). As expected, most MIR star-forming sequence galaxies have D_n4000 smaller than 1.5. In contrast, D_n4000 of the majority of the MIR green valley and MIR blue cloud galaxies is larger than 1.5. The mean D_n4000 of the MIR green valley galaxies (1.84 ± 0.03) is not different significantly from that of the MIR blue cloud galaxies (1.90 ± 0.01). However, the rms of D_n4000 for the MIR green valley galaxies is larger (0.10 ± 0.01) than that for the MIR blue cloud galaxies (0.07 ± 0.01), suggesting that the dispersion of mean stellar ages for the MIR green valley galaxies is larger than that for the MIR blue cloud galaxies. However, the difference in mean stellar ages between the two populations is more evident in the MIR color space.

2.5.2   Galaxies in Groups/Clusters and their MIR Classes

In this section we examine the spatial distribution of three MIR classes in the A2199 supercluster. We compute the fraction of each MIR class in galaxy groups/clusters, and examine the variation of the fraction with the mass of each system.

We first show the spatial distribution of galaxies in each MIR class over the en-

tire region of the A2199 supercluster in Figure 2.6. We mark the positions of three clusters (A2199, A2197W/E) and four X-ray bright groups (NRGs385, NRGs388, NRGs396, and the NGC 6159 group) as thick circles. The size of circles is proportional to their virial radii (R_{200}). We also mark the positions of four X-ray faint groups (NRGs389, NRGs395, NRGs399, and NRGs400, Rines et al. 2001) as triangles. To better show the clustering of galaxies, we overplot the grayscale galaxy number density map using all the member galaxies regardless of their MIR classes in each panel.

The 12 μm undetected galaxies (panel a) are mainly found in high-density regions. Early-type galaxies are highly concentrated in central regions of groups/clusters. Note that these early-type galaxies are in the optical red sequence with low stellar masses. Similarly, MIR blue cloud galaxies (panel b) and MIR green valley galaxies (panel c) are mainly found in groups and clusters. In contrast, MIR star-forming sequence galaxies are distributed over the entire supercluster region. Some of them are in groups and clusters, but they do not show a central concentration like MIR blue cloud and MIR green valley galaxies. Four X-ray faint groups do not show any significant clustering of galaxies.

We then calculate the fraction of each MIR class in the X-ray bright groups and clusters. We use the galaxies in the inner region ($R \leq 0.5R_{200}$) and in the outer region ($0.5R_{200} < R \leq R_{200}$) separately. For comparison, we also calculate the fraction of each MIR class for the galaxies not associated with any group or cluster (i.e., $R > 3 \times R_{200}$) in the supercluster region; these are the galaxies in "underdense regions". We use only 12 μm detected galaxies for computing fractions. If we use all the galaxies to compute the fractions by including the 12 μm undetected galaxies, the results do not change much.

The left panels of Figure 2.7 show the fraction of each MIR class in the inner region as a function of M_{200} of each galaxy system. The fractions of MIR blue cloud
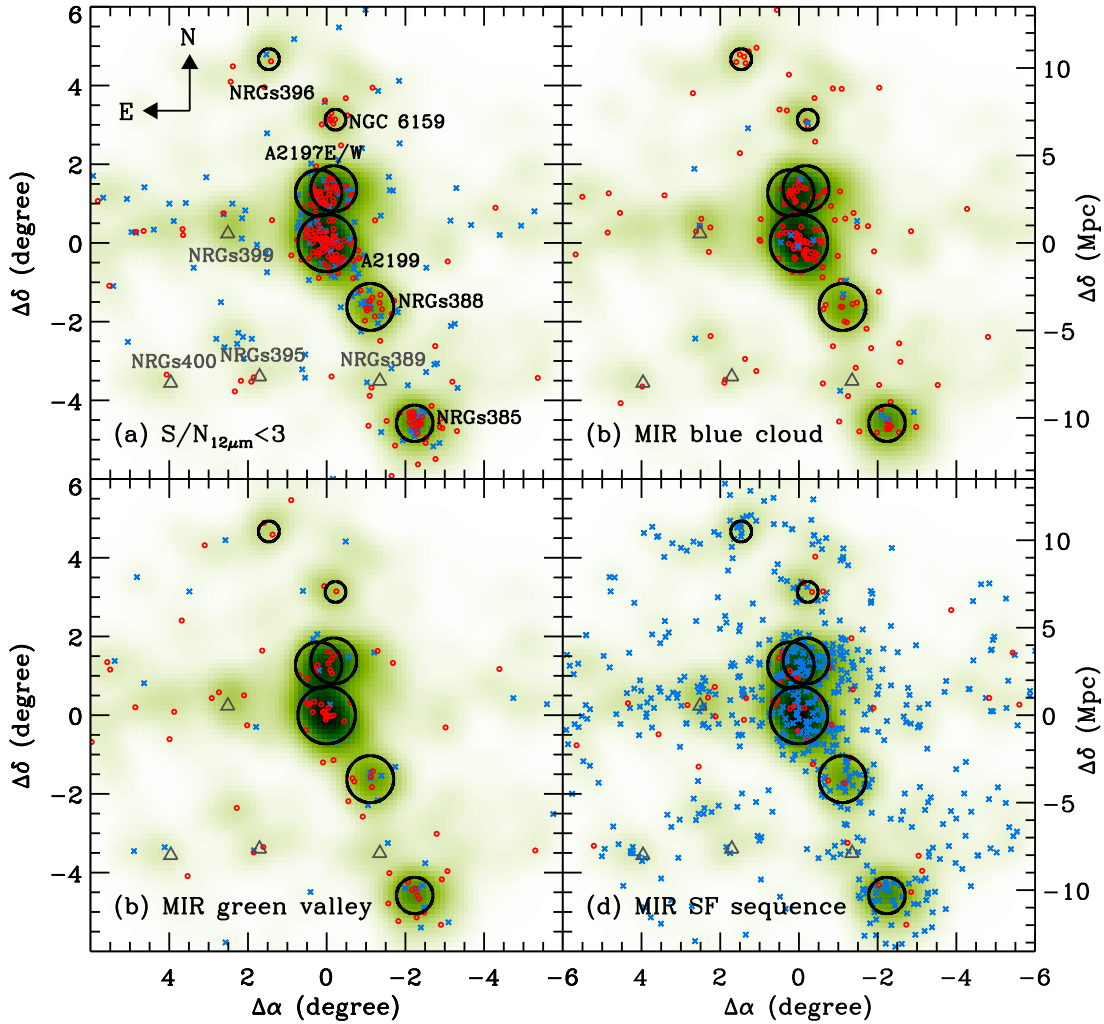
Figure 2.6 Spatial distribution of (a) the member galaxies undetected at 12μm ($S/N_{12\mu m} < 3$), (b) MIR blue cloud galaxies, (c) MIR green valley galaxies, and (d) MIR star-forming sequence galaxies in the A2199 supercluster. The green and white represent the galaxy number density distribution. Large circles represent the positions of X-ray bright clusters and groups, and their sizes are proportional to virial radii (R_{200}). Triangles represent the positions of four X-ray faint groups. Small circles and crosses represent early- and late-type galaxies, respectively.

galaxies (panel a) and of MIR star-forming sequence galaxies (panel c) vary from $\sim 20\%$ to $\sim 60\%$, but do not show any dependence on M_{200}. The fractions of MIR green valley galaxies in the galaxy systems are similar ($\sim 25\%$).

Similarly, the right panels for the galaxies in the outer region of groups/clusters show no dependence of the fraction on M_{200}. One unique point is that the fraction of each MIR class is nearly the same for all groups and clusters. Although we calculate the fraction using the galaxies at $R \leq R_{200}$ of each group and cluster (i.e., sum of the left and right panels), the M_{200} dependence of the fraction is not apparent.

On the other hand, panel (a) shows that the fractions of MIR blue cloud galaxies in the inner region of groups/clusters are significantly higher than in the underdense region (11.1%). However, the fractions in the outer region (panel d) are on average $\sim$18.5%, close to the fraction in the underdense region. The fraction of MIR green valley galaxies in the underdense region is 10.9% This value is smaller than those in the inner region (panel b), but is comparable to those in the outer region (panel e). The fractions of MIR star-forming sequence galaxies in the inner region (panel c) are much smaller than that in the underdense region (78%). However, the fractions in the outer region are close to the value in the underdense region (panel f).

Thus Figure 2.7 suggests that massive galaxies with low SFRs (i.e., MIR blue cloud galaxies and MIR green valley galaxies) are mainly in the inner regions of groups/clusters regardless of their M_{200}. Some of them are found even in the low density regions (i.e., the underdense region), but their fraction is not significant (up to $\sim 20\%$).

2.5.3   Environmental Dependence based on Σ_5 and R/R_{200}

To further examine the environmental dependence of the MIR classes in the A2199 supercluster, we use two environmental indicators in this section; the surface number density (Σ_5) and the cluster-(or group-)centric distance normalized by virial
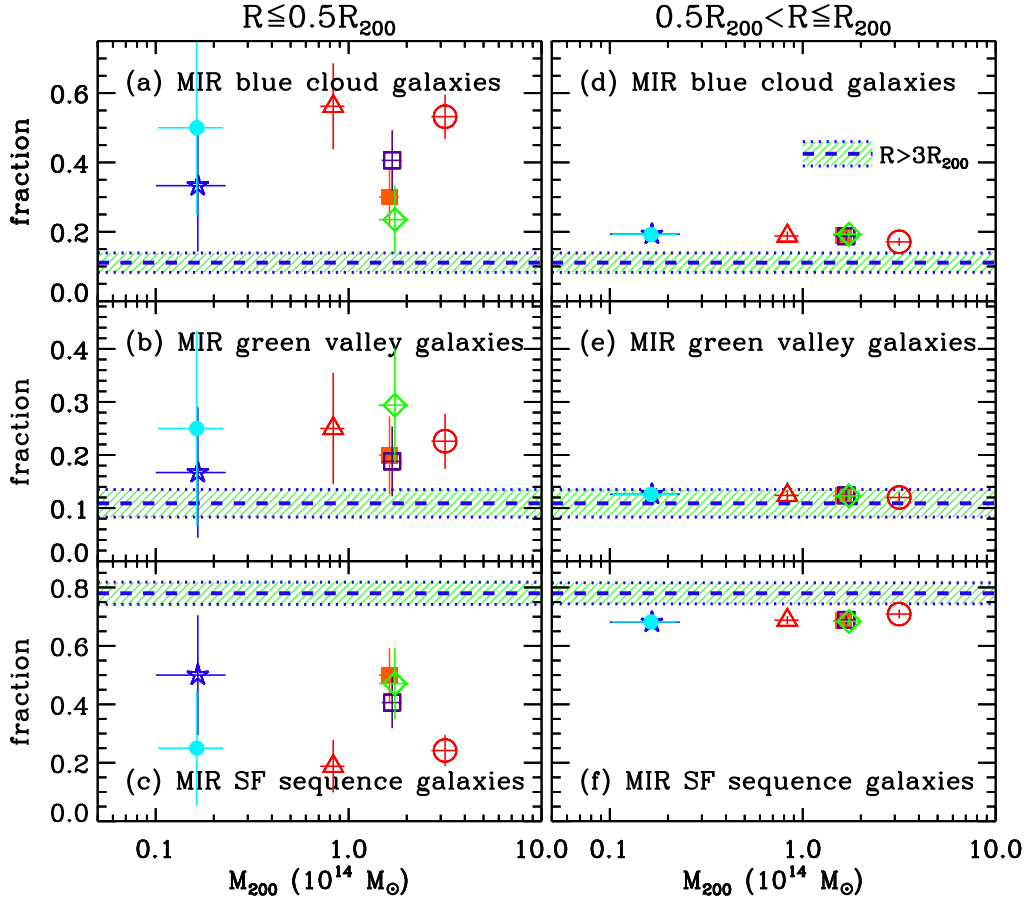
Figure 2.7 The fraction of (top) MIR blue sequence, (middle) MIR green valley, and (bottom) MIR star-forming sequence galaxies in the groups/clusters as a function of M_{200}. We use galaxies in the inner region ($R \leq 0.5R_{200}$, left) and the outer region ($0.5R_{200} < R \leq R_{200}$, right), separately, of groups and clusters. The symbols are the same as Figure 2.1. Hatched regions represent the fraction of each MIR class in the underdense region.

radius (R/R_{200}). The surface number density, Σ_5, is defined by $\Sigma_5 = 5(\pi D_{p,5}^2)^{-1}$, where $D_{p,5}$ is the projected distance to the 5th-nearest neighbor. The fifth-nearest neighbor to each galaxy is identified in the sample of A2199 supercluster member galaxies. We compare the cumulative distribution of each MIR class as function of two environmental indicators. We also use the Kolmogorov-Smirnov two-sample test to quantify the difference in the distribution if any.

Figure 2.8 shows the cumulative distribution of each MIR class as a function of Σ_5. Panel (a) shows the case for all the 12 μm detected galaxies. MIR star-forming sequence galaxies (red long dashed line) tend to be in low-density regions, and MIR blue cloud galaxies (blue solid line) prefer high-density regions. MIR green valley galaxies (green dashed line) are between the two. This result is consistent with the expectations from the morphology- and/or SFR-density relation (e.g., Dressler 1980; Lewis et al. 2002; Park & Hwang 2009; Hwang et al. 2010).

Panel (b) shows the same Σ_5 distribution of each MIR class, but only for early-type galaxies. It shows that the difference between MIR blue cloud and MIR green valley galaxies is noticeably reduced. The confidence level to reject the hypothesis that the two distributions are extracted from the same parent population changes from 92% in panel (a) into 52% in panel (b). This suggests that Σ_5 of MIR green valley early-type galaxies do not differ significantly from that of MIR blue cloud early-type galaxies. On the other hand, the cumulative distribution of MIR star-forming sequence early-type galaxies is still distinguishable from those of MIR blue cloud and MIR green valley early-type galaxies.

Figure 2.8(c) shows the cumulative distribution only for late-type galaxies. The confidence level to reject the hypothesis that the two distributions are extracted from the same parent population is 93% between MIR green valley and MIR blue cloud late-type galaxies, and is 97% between MIR green valley and MIR star-forming sequence late-type galaxies.
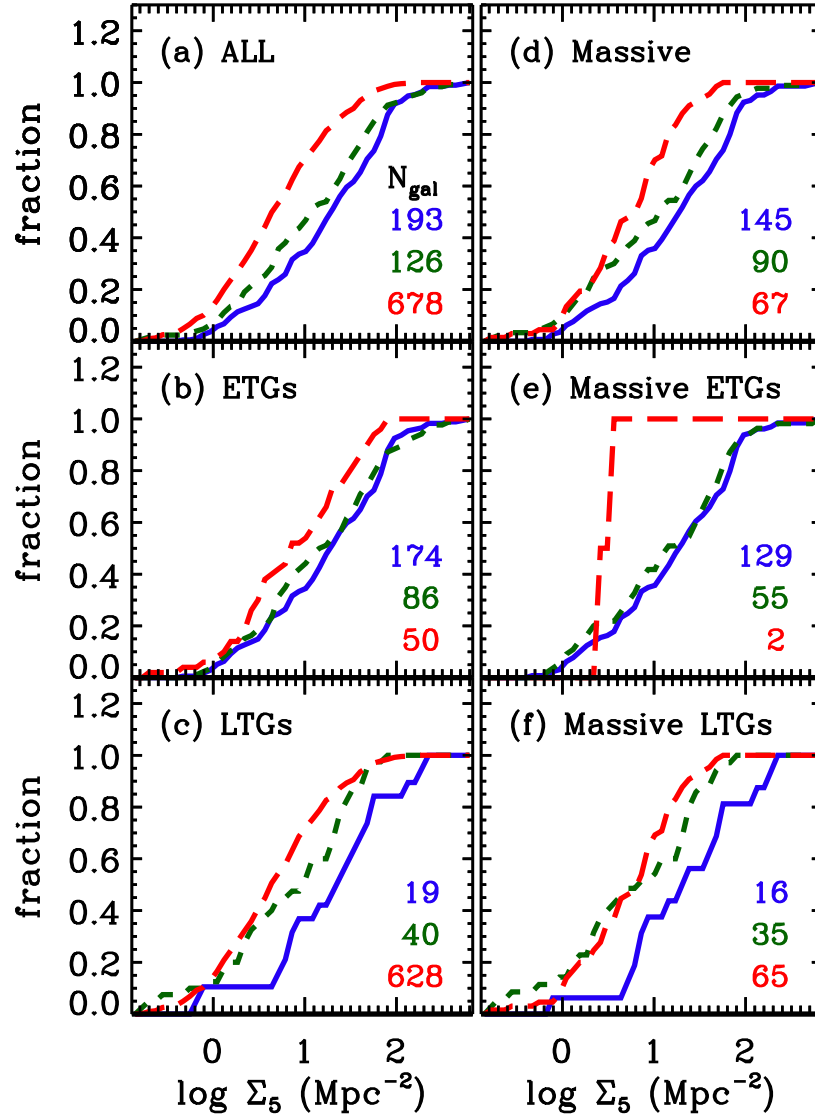
Figure 2.8 Cumulative distribution function of the three MIR classes as a function of the surface galaxy number density (Σ_5) for MIR blue cloud galaxies (solid line), MIR green valley galaxies (short dashed line), and MIR star-forming sequence galaxies (long dashed line). The galaxy sample used in each panel is (a) all 12 μm detected galaxies, (b) early-type galaxies, (c) late-type galaxies, (d) massive galaxies greater than log ($M_{star}/M_{\odot}$) > 10.5, (e) massive early-type galaxies, and (f) massive late-type galaxies. We list the number of three MIR class galaxies used in each panel.

Because galaxy properties also strongly depend on stellar mass as well as on environment (Tasca et al. 2009; Hwang et al. 2010; Cucciati et al. 2010; Bolzonella et al. 2010; Peng et al. 2010a; Sobral et al. 2011), we restrict our analysis to only massive galaxies with $\log(M_{\mathrm{star}}/M_\odot) > 10.5$ to reduce the mass effect on the MIR properties. Figure 2.8(d) shows the cumulative distribution for the massive galaxies with 12 μm detection. Although the number of galaxies in each MIR class is reduced, the result is similar to that in panel (a). Panel (e) shows the case of massive early-type galaxies. MIR blue cloud and MIR green valley galaxies again show similar distributions. However, the cumulative distribution of MIR green valley galaxies among the massive late-type galaxies (panel f) is still between MIR blue cloud and MIR star-forming sequence galaxies.

We perform similar analysis in Figure 2.9 using the normalized cluster/group-centric distance R/R_{200} instead of Σ_5. Panel (a) shows the cumulative distribution of each MIR class using all the 12 μm detected galaxies. The R/R_{200} distribution of MIR star-forming sequence galaxies is significantly different from those of MIR blue cloud and MIR green valley galaxies; the hypothesis that the two distributions are extracted from the same parent population can be rejected at a confidence level of >99%. However, the distributions of MIR blue cloud and MIR green valley galaxies are very similar. They show similar distributions even if we consider only early-type galaxies in panel (b), massive galaxies in panel (d), and massive early-type galaxies in panel (e).

On the other hand, when we consider late-type galaxies, the similar distribution between MIR blue cloud and MIR green valley galaxies disappears. The confidence level to reject the hypothesis that the two distributions are extracted from the same parent population is 92% in panel (c) and is 73% in panel (f). The cumulative distribution of MIR green valley late-type galaxies appears to be similar to that of MIR star-forming sequence late-type galaxies, and be still between the MIR blue
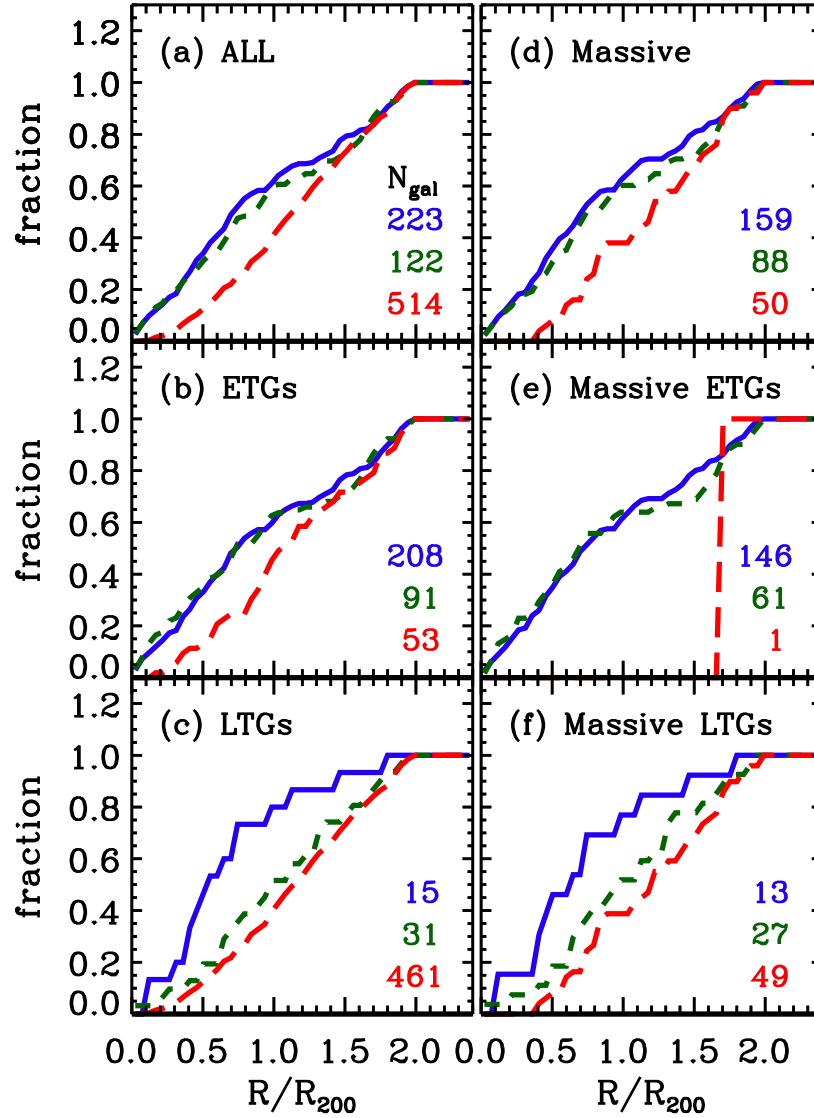
Figure 2.9 Same as Figure 2.8, but the cumulative distribution as a function of cluster/group-centric distance normalized by virial radius (R/R_{200}).

cloud and the MIR star-forming sequence galaxies (panels c and f).

Both Figures 2.8 and 2.9 give similar results. The cumulative distributions of Σ_5 and R/R_{200} for MIR green valley galaxies are between those for MIR blue cloud galaxies and for MIR star-forming sequence galaxies. However, among early-type galaxies the difference between MIR blue cloud and MIR green valley galaxies disappears. In contrast, when considering only late-type galaxies, the MIR green valley galaxies are still between the MIR blue cloud and the MIR star-forming sequence galaxies.

2.6   Discussion

2.6.1   Star Formation Activity of Galaxy Systems and their Dependence on Virial Mass

We compare the star formation activity of X-ray bright galaxy groups and clusters in the A2199 supercluster using $\Sigma SFR/M_{200}$ (Section 2.4) and the fraction of MIR star-forming sequence galaxies (Section 2.5.2). Interestingly, both $\Sigma SFR/M_{200}$ and the fraction do not seem to depend on virial masses of galaxy systems (see Figures 2.1 and 2.7). This is seen both in inner ($R \leq 0.5R_{200}$) and outer regions ($0.5R_{200} < R \leq R_{200}$).

Our results are consistent with those in other studies. For example, Goto (2005) used the SDSS data for 115 nearby clusters, and found no dependence of $\Sigma SFR/M_{200}$ and of blue/late-type galaxy fraction on cluster virial mass (see also Bai et al. 2009, 2010; Balogh & McGee 2010). A recent study based on *WISE* data for 69 clusters at $z < 0.1$ also find no correlation between $\Sigma SFR/M_{200}$ and M_{200} (Chung et al. 2011).

No correlation between the fraction of passive (or red) galaxies and the halo masses of groups/clusters could result from a simultaneous increase in the number of member galaxies and of massive quiescent elliptical galaxies with increasing M_{200}

of the systems (De Lucia et al. 2012). No correlation between the two can also be explained by the pre-processing mechanism (Zabludoff & Mulchaey 1998), which is that giant elliptical galaxies or cD galaxies are formed by galaxy-galaxy mergers in poor groups, and then fall into clusters later. This pre-processing occur in poor groups with $M_{200} < 10^{13}$ $M_{\odot}$. This results in no M_{200}-dependence of the star formation activity in groups/clusters when the poor groups fall into more massive clusters with $M_{200} > 10^{13}$ $M_{\odot}$ (Balogh & McGee 2010); this covers the mass range of the galaxy systems in the A2199 supercluster.

On the other hand, some studies show that there is mass dependence of the star formation activity of galaxy groups/clusters. For example, Finn et al. (2005) and Koyama et al. (2010) found an anti-correlation between ΣSFR/M_{200} and M_{200} for clusters at $z < 1$ (see also Bai et al. 2007 and Poggianti et al. 2008). This anti-correlation is seen in clusters with 10^{13} $M_{\odot} < M_{200} < 3 \times 10^{14}$ $M_{\odot}$ that covers our galaxy systems in the A2199 supercluster. Furthermore, Popesso et al. (2012) used far-infrared Herschel data for nine clusters ($M_{200} \geq 3 \times 10^{14}$ $M_{\odot}$) and nine groups/poor clusters (10^{13} $M_{\odot} < M_{200} < 3 \times 10^{14}$ $M_{\odot}$) at $z < 1.5$, and found that ΣSFR/M_{200} is higher for groups/poor clusters than for massive clusters at a given redshift. They suggested that this mass dependent star formation activity results from earlier quenching of the star formation activity in galaxies associated to more-massive halos (i.e., clusters).

Similarly, some studies show that the fraction of star-forming galaxies decreases with increasing cluster mass (e.g., Martínez et al. 2002; Rasmussen et al. 2012). Poggianti et al. (2006) used the clusters at low z ($0.04 < z < 0.08$) and at high z ($0.4 < z < 0.8$), and found an anti-correlation between the fraction of star-forming galaxies and velocity dispersion (σ_p) of the clusters; the anti-correlation is significant for low-z clusters with $\sigma_p < 550$ km s^{-1} ($M_{200} \leq 2 \times 10^{14} M_{\odot}$). Most galaxy systems in the A2199 supercluster have $\sigma_p < 550$ km s^{-1}. However, the fraction

of star-forming galaxies (i.e., MIR star-forming sequence galaxy fraction) in galaxy groups/clusters of the A2199 supercluster does not show any strong dependence on M_{200}.

It seems that the mass dependence of star formation activity of groups/clusters is still inconclusive. Some previous studies used heterogeneous data with different wavelength, sky coverage, redshift and sensitivity (see Appendix of Bai et al. 2007). Finn et al. (2005) and Koyama et al. (2010) suggested that the mass dependence of $\Sigma \mathrm{SFR}/M_{200}$ appears due to the strong redshift dependence (high-z clusters have higher $\Sigma \mathrm{SFR}/M_{200}$ and smaller M_{200} in their data). In addition, Poggianti et al. (2006) showed that their mass dependence of the fraction of star-forming galaxies becomes unclear when they used another cluster sample from Miller et al. (2005). Thus it still needs more efforts to examine whether cluster mass is a critical factor in determining their star formation activity or not.

If the star formation activity in groups/clusters indeed depends on M_{200}, no M_{200}-dependence for the galaxy systems in the A2199 supercluster indicates that there could be other mechanisms that have affected the star formation activity of the systems. One possible mechanism is the interaction between infall groups and the supercluster. If the star formation activity of group galaxies have gradually decreased through the gravitational and/or hydrodynamical interaction with the supercluster, the current star formation activity of the groups would depend on when the groups fell into the supercluster environment. Thus, the different infall time of the groups in the supercluster could explain the different star formation activity of groups at a given M_{200}.

Similarly, the interaction between groups/clusters can change their star formation activity (Bekki 1999; Owen et al. 2005; Miller 2005; Ferrari et al. 2005; Johnston-Hollitt et al. 2008; Hwang & Lee 2009). In fact, there are three clusters close to the central region of the A2199 supercluster: A2199, A2197E and A2197W. In particular,

A2197E and A2197W overlap each other both on the sky and in redshift space; two clusters may be currently interacting. A2199 also seems to interact with A2197W/E and with another nearby group, NRGs388. Thus, the star formation activity of A2199, A2197W/E, and NRGs388 could be enhanced by the interaction among them. Note that the merging/interaction stages are also important to determine the star formation activity of galaxy groups/clusters (Hwang & Lee 2009). Therefore, the different merging/interaction stages of the groups/clusters in the supercluster can add significant scatters to the anti-correlation between the star formation activity and M_{200}, and can results in no correlation between the two.

2.6.2 Morphology Dependence of the Galaxies in the MIR Green Valley

In Section 2.5.3 we compare the cumulative distribution of Σ_5 and R/R_{200} for different MIR classes. The different distributions between MIR blue cloud galaxies and MIR star-forming sequence galaxies are consistent with the expectations from the morphology- and SFR-density relations; most MIR blue cloud galaxies are morphologically early types with low SFRs, but MIR star-forming sequence galaxies are generally late-type galaxies with high SFRs (see Figure 2.5). Interestingly, the distribution of MIR green valley galaxies are between MIR blue cloud and MIR star-forming sequence galaxies in both environmental indicators. Because the environment strongly affects galaxy morphology and the star formation activity (Park et al. 2007; Blanton & Moustakas 2009), the MIR green valley galaxies between MIR blue cloud and MIR star-forming sequence galaxies seem to be in a transition stage.

However, when we fix galaxy morphology, the behavior of the MIR green valley galaxies changes. The MIR green valley galaxies with early-type morphology show a distribution very similar to that of the early-type MIR blue cloud galaxies. However, the MIR green valley galaxies with late-type morphology still show a distribution

between MIR blue cloud and MIR star-forming sequence galaxies. This trend is also apparent even if we use only massive galaxies with $\log(M_{\text{star}}/M_\odot) > 10.5$. The similarity between MIR green valley and the MIR blue cloud galaxies among the early types is also seen in their stellar masses: $\log(M_{\text{star}}/M_\odot) = 10.66 \pm 0.04$ for MIR green valley early types and $\log(M_{\text{star}}/M_\odot) = 10.75 \pm 0.03$ for MIR blue cloud early types.

To better understand the physical meaning of the observed galaxy colors, we show NUV$-r$ and $u - r$ colors of early-type galaxies as a function of *WISE* $[3.4] - [12]$ colors in Figure 2.10 (see also Ko et al. (2013)). We model that the MIR emission among early types (i.e., MIR green valley early-type galaxies) can be explained by the presence of a small fraction of young stellar population. Panel (a) shows the NUV$-r$ versus $[3.4] - [12]$ color-color distribution of early-type member galaxies and the SWIRE templates of Polletta et al. (2007). We overplot the two-component SSP models of Piovan et al. (2003) with various combination of an old stellar population (12 Gyr) and young populations (0.5, 1, and 2 Gyr) with solar metallicity. The model grids indicate different fractions of a young population from 0.1% to 50%.

The plot shows that only $> 1\%$ of 0.5 Gyr or $> 5\%$ of 1 Gyr population can make $[3.4] - [12]$ colors green (> -1.55). The plot also shows that about 50% of MIR green valley early-type galaxies have no NUV excess emission (NUV$-r > 5.4$). Ko et al. (2013) suggested that young stellar populations with 0.5 and 1 Gyr can make the galaxies to have both MIR and NUV excess, but 2 Gyr population does not make any NUV excess. This means that half of MIR green valley early-type galaxies stop forming stars at least 2 Gyr ago. This > 2 Gyr old recent star formation is detected only in the MIR (neither in the NUV nor in the optical) because the MIR traces star formation over longer timescale (> 2 Gyr) than NUV and optical bands (Ko et al. 2013; Schawinski et al. 2014).

Figure 2.10(b) displays the $u - r$ versus $[3.4] - [12]$ distribution of early-type
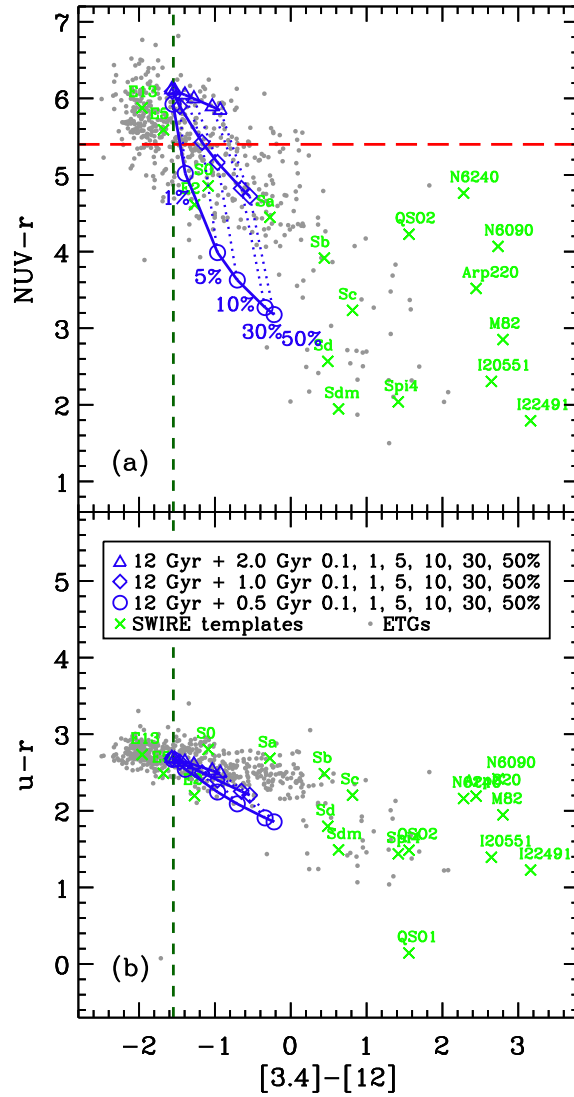
Figure 2.10 (a) NUV−r vs. $[3.4] − [12]$ and (b) $u − r$ vs. $[3.4] − [12]$ color-color distributions for early-type member galaxies (gray dots). Solid lines show the color prediction from the two-component SSP model (Piovan et al. 2003). These colors are obtained using several combinations of an old stellar population (12 Gyr) and young populations (0.5, 1, and 2 Gyr) with varying fraction (0.1, 1, 5, 10, 30, and 50%) of young populations. Crosses represent the SWIRE templates (Polletta et al. 2007). The vertical dashed line represents $[3.4] − [12] = −1.55$ that is the border line between MIR blue cloud and MIR green valley galaxies, while the horizontal dashed line is the NUV excess cut, NUV−r = 5.4, used in Ko et al. (2013).

member galaxies. The model grids show that $u - r$ colors change very little with increasing the fraction of young populations. This result is consistent with the results in Figures 2.4 and 2.5; the MIR green valley and MIR blue cloud early-type galaxies show similar optical properties.

The environmental dependence of these MIR classes and their optical properties shown in Section 2.5 suggest a possible evolutionary scenario of galaxies from late-type star-forming galaxies to early-type quiescent galaxies: 1) Late-type MIR star-forming sequence galaxies $\rightarrow$ 2) Late-type MIR green valley galaxies $\rightarrow$ 3) Early-type MIR green valley galaxies $\rightarrow$ 4) Early-type MIR blue cloud galaxies. Because the timescale for the suppression of star formation activity is shorter than the timescale for morphological transformation (Blanton & Moustakas 2009), we expect that the star formation activity of supercluster galaxies decreases first (1$\rightarrow$2), and then the morphological transformation would be followed (2$\rightarrow$3). Skibba et al. (2009) found that the color-density relation is more fundamental than the morphology-density relation. Bamford et al. (2009) also obtained a similar result, and suggested that the color transformation driven by environment should take place on shorter timescales than the morphological transformation. This agrees well with our scenario.

Masters et al. (2010) studied the environmental dependence of (optically) red (or passive) spiral galaxies that are considered as transition objects between normal blue spirals and red early-type galaxies. They showed that red spirals are mainly found in intermediate density regions and have higher stellar masses than blue spirals. These characteristics of red spirals are very similar to those of late-type MIR green valley galaxies (see Figures 2.5, 2.8, and 2.9). They also suggested that strangulation or starvation (removal of gas in outer halo and no further accretion of cold gas) is a plausible mechanism for producing red spirals. These mechanisms can explain quenching of star formation even in low-mass groups (Kawata & Mulchaey 2008; Wetzel et al. 2013), which accounts for the presence of late-type MIR green

valley located outside the cluster regions (see Figure 2.6). However, low-mass spirals cannot keep their spiral structures from the environmental processes (Bekki et al. 2002). This explains why late-type MIR green valley galaxies (red spirals) have higher stellar masses than late-type MIR star-forming sequence galaxies (normal blue spirals).

When galaxies enter the MIR green valley, they undergo morphological transformation from late types to early types. Early-type MIR green valley galaxies are more likely to exist in high density regions than late-type MIR green valley galaxies (see Section 2.5.3). This suggests that the environment can play a role in the morphological transformation in the MIR green valley. George et al. (2013) suggested that the observed morphological dependence of galaxies on environment cannot be fully explained by strangulation and disk fading (Quilis et al. 2000). Instead, galaxy mergers and close tidal interactions should be required for the morphological transformation. Park & Hwang (2009) also found that cumulative galaxy-galaxy gravitational/hydrodynamic interactions are the main drive for the morphological transformation in cluster environment. Bekki & Couch (2011) showed that the transformation in group environment can be driven by repetitive slow encounters with group members. These processes seem suitable for MIR green valley galaxies that are mainly in groups and clusters.

To summarize, the star formation of galaxies is quenched before the galaxies enter the MIR green valley, which is mainly driven by strangulation or starvation. Then, the morphological transformation from late types to early types occurs in the MIR green valley, especially, for massive late-type galaxies with log $(M_{\mathrm{star}}/M_\odot) > 10$. The main environmental mechanisms for the morphology transformation are galaxy-galaxy mergers and interactions. After the transformation, early-type MIR green valley galaxies stay for several Gyrs keeping the memory of their last star formation.

2.7   Summary and Conclusions

Using the multi-wavelength data covering the entire region of the A2199 supercluster, we study the star formation activity of galaxy groups/clusters in the supercluster and the MIR properties of the supercluster galaxies. We determine $\Sigma\mathrm{SFR}/M_{200}$ of groups and clusters using *WISE* 22 μm data, and find no dependence of $\Sigma\mathrm{SFR}/M_{200}$ on M_{200}.

We classify galaxies into three MIR groups in the *WISE* $[3.4] - [12]$ color versus 12 μm luminosity diagram: MIR blue cloud galaxies, MIR star-forming sequence galaxies, and MIR green valley galaxies. MIR blue cloud galaxies are mostly (90%) early types, while MIR star-forming sequence galaxies are predominantly (93%) late types. MIR green valley galaxies consist of early- (68%) and late-type galaxies (32%). SFRs for MIR blue cloud and MIR green valley galaxies are similar, but much smaller than those for MIR star-forming sequence galaxies. It is important that the MIR green valley galaxies are distinguishable from the optical green valley galaxies, in the sense that they belong to the optical red sequence. Thus star formation quenching of galaxies occurs before the galaxies enter the MIR green valley.

We calculate the fraction of each MIR class in groups/clusters. We could not find any dependence of the fraction of each MIR class on M_{200}, consistent with the trend of $\Sigma\mathrm{SFR}/M_{200}$. These results suggest that group/cluster mass does not play an important role in controlling the global star formation activity of the systems. On the other hand, there could be other mechanisms affecting the global star formation activity of the systems. These include the interaction between infalling groups and the supercluster, and between groups/clusters.

We compare the cumulative distribution of Σ_5 and R/R_{200} for the three MIR classes. MIR green valley galaxies show the distribution between MIR blue cloud and MIR star-forming sequence galaxies. When only considering early-type galaxies, the difference between MIR blue cloud and MIR green valley galaxies disappears. How-

ever, late-type galaxies in the MIR green valley still show the distribution between MIR blue cloud and MIR green valley galaxies. These results suggest a possible evolutionary scenario: 1) Late-type MIR star-forming sequence galaxies $\rightarrow$ 2) Late-type MIR green valley galaxies $\rightarrow$ 3) Early-type MIR green valley galaxies $\rightarrow$ 4) Early-type MIR blue cloud galaxies. Thus the MIR green valley is the site where morphology transformation of galaxies mainly appears to occur.

Chapter 3

A *WISE* MIR View on the Highway for Galaxy Evolution in Compact Groups

(This chapter is published in the Astrophysical Journal.)[1]

3.1 Introduction

Compact groups of galaxies contain several galaxies within just a few tens of kiloparsec scales. This makes compact groups have extremely high galaxy number densities (the median galaxy number density of $\log(\rho/[h^{-3}\ \mathrm{Mpc}^3])= 4.36$, Sohn et al. 2016), higher than the galaxy number densities of cluster and group environments (the median galaxy number density of $\log(\rho/[h^{-3}\ \mathrm{Mpc}^3])= 1.97$ for clusters and groups in the A2199 supercluster, Lee et al. 2015; Sohn et al. 2015). The velocity dispersions of compact groups are much smaller (< 879 km s^{-1} with a median value of 194 km s^{-1} with a standard deviation of 156 km s^{-1}, Sohn et al. 2016, Table 7)

---

[1]Lee, G.-H., Hwang, H. S., Sohn, J., & Lee, M. G. 2017, ApJ, 835, 280

than those of clusters ($\sim 400-1300$ km s^{-1} with a median value of 778 km s^{-1} and a standard deviation of 208 km s^{-1}, Rines et al. 2013). These two characteristics make compact groups an ideal environment for frequent interactions and mergers between galaxies (e.g., Rubin et al. 1990; Rodrigue et al. 1995; Amram et al. 2007; Coziol & Plauchu-Frayn 2007; Plauchu-Frayn & Coziol 2010; Gallagher et al. 2010; Konstantopoulos et al. 2012; Sohn et al. 2013; Vogt et al. 2015).

Numerical simulations suggested that galaxies in a compact group should merge into a single elliptical galaxy within a few Gyrs, causing the compact group to disappear (Barnes 1985, 1989; Mamon 1987). Gallagher et al. (2010) also reached a similar conclusion through their study of star cluster age-dating and neutral hydrogen content in the Hickson compact group 31; the compact group should merge into a single elliptical within 1 Gyr (see also Rubin et al. 1990). Kroupa (2015) suggested that the abundance of compact groups should decrease as the redshift decreases from $z \simeq 0.1$ to $z = 0$ in the ΛCDM universe. However, Sohn et al. (2015) found that the abundance of compact groups changes little with redshifts at $0.01 < z < 0.22$, using a spectroscopically complete sample of 332 compact groups. Kroupa (2015) also suggested an alternative scenario that compact groups do not merge, which predicts a constant abundance of compact groups at $z < 0.1$. However, this alternative scenario is based on the assumption of a universe without dark matter.

Diaferio et al. (1994) suggested that compact groups replenish themselves with new members from the surrounding environment, thereby extending their lifetimes to the current epoch. The finding of Sohn et al. (2015), constant abundance of compact group at $0.01 < z < 0.22$, can be explained by this replenishment model. This replenishment model is supported by several observational findings that showed that many ($> 50\%$) compact groups are embedded in or associated with larger-scale structures (Rood & Struble 1994; Ramella et al. 1994; de Carvalho et al. 1994; Ribeiro et al. 1998; Mendel et al. 2011; Pompei & Iovino 2012). However,

Díaz-Giménez & Zandivarez (2015) showed that only 27% of compact groups are embedded in surrounding structures.

Unfortunately, many existing compact group catalogs suffer from some observational biases, which make them difficult to use for testing compact group formation models and for studying the relation between compact groups and their surrounding environments. For example, McConnachie et al. (2009) constructed a large sample of compact groups, from the photometric data ($m_r < 21$) of SDSS Data Release 6 (Adelman-McCarthy et al. 2008), including 77,088 compact group candidates and their 313,508 tentative member galaxies. Their sample is the largest one currently, but it is highly contaminated with interlopers ($> 50\%$, Mendel et al. 2011; Sohn et al. 2013) because the sample is based only on photometric information using Hickson's selection criteria (Hickson 1982). To reduce this contamination, Sohn et al. (2015) compiled the redshifts from Fred Lawrence Whipple Observatory (FLWO)/FAST observations and from the SDSS DR12 for the photometric sample of compact group galaxies in McConnachie et al. (2009), and constructed a catalog of 332 compact groups. This catalog is currently the largest one with complete spectroscopic redshifts. However, this sample is affected by an isolation criterion from Hickson's selection criteria. The isolation criterion requires that no galaxies be present in a radius of up to three times the group radius. This criterion was adopted to avoid selecting very dense regions like cluster cores, but this could introduce a bias that misses nearby compact groups with apparently large sizes and embedded systems in dense environments (Barton et al. 1996).

Recently, Sohn et al. (2016) published a new catalog of 1588 compact groups and their 5178 member galaxies at $0.01 < z < 0.19$ using SDSS DR12 spectroscopic data supplemented by additional redshifts from the literature and from FLWO/FAST observations. They applied a friends-of-friends algorithm to identify the compact groups without using the isolation criterion. As a result, their catalog successfully

contains nearby ($z < 0.05$) compact groups and embedded systems in dense regions. This is important in order to study the relation between compact groups and their surrounding environments without any sample bias.

Previous observational studies suggested that galaxy evolution in compact groups is faster than in the field from the comparisons of Lick indices (Proctor et al. 2004; Mendes de Oliveira et al. 2005; de la Rosa et al. 2007), the star formation quenching timescales (Plauchu-Frayn et al. 2012), specific SFRs distribution (Tzanavaris et al. 2010; Coenda et al. 2015; Lenkić et al. 2016), and color distribution (Bitsakis et al. 2010, 2011, 2016; Walker et al. 2010, 2012). Proctor et al. (2004) and Mendes de Oliveira et al. (2005) found that the stellar ages and the early-type galaxy fractions of compact group galaxies are similar to those of cluster galaxies, which suggests that compact group galaxies evolve as fast as cluster galaxies.

On the other hand, Johnson et al. (2007) and Walker et al. (2010, 2012) showed that compact group galaxies exhibit a bimodal distribution in the *Spitzer* IRAC ($3.6 - 8.0$ μm) color space with a statistically evident gap, so-called "canyon", between star-forming galaxies with MIR red colors and quiescent galaxies with MIR blue colors. Recently, Zucker et al. (2016) newly identified the canyon galaxies in the *WISE* color-color diagram. This gap may suggest the accelerated galaxy evolution in compact groups because the gap is not seen in comparison galaxy samples from field, from interacting pairs, and from the center of the Coma cluster (Walker et al. 2010, 2012, 2013). Cluver et al. (2013) found that compact group galaxies in the gap mostly show enhanced warm H_2 emission from the observations with the *Spitzer* Infrared Spectrograph, which could be caused by shock heating (Appleton et al. 2006; Cluver et al. 2010). This result implies that shock heating may be responsible for rapid evolution of galaxies in compact groups.

However, these results are mainly based on the catalogs of compact groups selected using Hickson's criteria, which can introduce a sample bias. We therefore

revisit the issues on the comparison of compact groups galaxies with cluster and field galaxies using the unbiased sample of compact groups from Sohn et al. (2016). In this paper, we use the *WISE* MIR data to study the environmental effects on compact group galaxies and the relation between compact groups and their surrounding environments. The MIR data are useful indicators of mean stellar ages (Piovan et al. 2003; Ko et al. 2009), especially for compact group galaxies that are mainly dominated by old stellar populations. Red-sequence galaxies with small amounts of young (< 1 Gyr) and intermediate-age (1-10 Gyr) stellar populations can be distinguished from those without the populations in MIR color space (Ko et al. 2013, 2016; Lee et al. 2015). The sample we use in this paper contains 670 compact groups with 2175 member galaxies drawn from the catalog of Sohn et al. (2016). When we investigate the MIR properties of galaxies in Sections 3.3 and 3.4, we use 1541 member galaxies detected at 12 μm with a signal-to-noise ratio (S/N) greater than 3. This sample is larger than those of previous MIR studies. For example, the samples of Walker et al. (2012) and several previous studies (Johnson et al. 2007; Bitsakis et al. 2010, 2011; Walker et al. 2010) have less than 50 compact groups, the sample of Walker et al. (2013) has 99 compact groups and 348 member galaxies, and the sample of Zucker et al. (2016) has 163 compact groups and 567 member galaxies.

Section 3.2 describes the compact group sample and comparison samples of cluster/field galaxies. In Section 3.3 we compare the properties of galaxies in compact groups with those in other environments, and investigate how environment affects the properties of galaxies in compact groups. In Section 3.4 we discuss the environmental effects on galaxy evolution in compact groups and the relation between compact groups and their surrounding environments. In Section 3.5 we summarize our results and present conclusions. Throughout, we adopt flat ΛCDM cosmological parameters: $H_0 = 70$ km s^{-1} Mpc^{-1}, $\Omega_\Lambda = 0.7$, and $\Omega_m = 0.3$.

3.2   Data

Sohn et al. (2016) constructed a catalog of compact groups using the spectroscopic sample of SDSS DR12 galaxies with $m_r < 17.77$. The completeness of the spectroscopic data in SDSS is low for bright galaxies at $m_r < 14.5$ because of saturation and cross-talk in the spectrograph, and for the galaxies in high-density regions (e.g., galaxy clusters) because of the fiber collision (see Figure 1 of Park & Hwang 2009). Therefore, Sohn et al. (2016) supplemented the catalog with redshifts from the literature (Hill & Oegerle 1993, 1998; Wegner et al. 1996, 1999; Slinglend et al. 1998; Falco et al. 1999; see also Hwang et al. 2010) and from FAST observations at FLWO (Sohn et al. 2015). They applied the friends-of-friends algorithm with a projected linking length of $\Delta D = 50 \ h^{-1}$ kpc and a radial linking length of $|\Delta V| = 1000$ km s^{-1}, and constructed a magnitude-limited ($m_r < 17.77$) sample of 1588 compact groups with each consisting of three or more member galaxies at $0.01 < z < 0.19$. This new catalog contains 18 times as many systems and reaches three times the depth of the catalog of Barton et al. (1996), which is also based on the friends-of-friends algorithm.

Sohn et al. (2016) also constructed two volume-limited subsamples: the V1 sample of galaxies with $M_r < -19.77$ and $0.01 < z < 0.0741$ and the V2 sample of galaxies with $M_r < -20.77$ and $0.01 < z < 0.1154$ (V2)[2]. These volume-limited samples contain 670 and 297 compact groups that are independently identified through the friends-of-friends algorithm. Unlike systems in the magnitude-limited sample, the volume-limited samples have systems with a median stellar mass independent of redshift. Therefore, the volume-limited samples allow us to study the properties of compact groups without any sample bias that could be introduced in the

---

[2]Sohn et al. (2016) used $M_r < -19 + 5\log h$ and $M_r < -20 + 5\log h$ with $h = 1$ (i.e., $H_0 = 100$ km s^{-1} Mpc^{-1}). However, we adopt $h = 0.7$ (i.e., $H_0 = 70$ km s^{-1} Mpc^{-1}), which results in $-19 + 5\log h \simeq -19.77$ and $-20 + 5\log h \simeq -20.77$.

magnitude-limited sample. Details for the catalogs and the compact group selection are described in Sections 2 and 3 of Sohn et al. (2016).

In this study, we use the V1 sample of 670 compact groups and their 2175 member galaxies with $M_r < -19.77$ and $0.01 < z < 0.0741$. To study the MIR properties of these galaxies, we cross-correlate the galaxies with the objects in the *ALLWISE* source catalog[3] using a matching tolerance of $3''$, corresponding to about half of the FWHM of the PSF at 3.4 μm. Among the 2175 galaxies, 2067 (95%) are matched with *ALLWISE* sources. We use the profile-fitting magnitudes of the sources at four MIR bands (3.4 μm, 4.6 μm, 12 μm, and 22 μm). When we investigate the MIR properties of galaxies, we use only galaxies detected at 12 μm with S/N > 3. Because the *ALLWISE* magnitudes with S/N < 2 are just upper limits, we choose only the galaxies with S/N > 3 to safely use the magnitudes. Among the 2175 galaxies, 1541 galaxies (71%) are detected at 12 μm. If we adopt the S/N cut of 5, the sample size is reduced from 1541 to 863 galaxies by 44%. However, we confirm that our conclusions do not change much even if we use this small sample.

To compare the physical properties of compact group galaxies with those in other environments, we use two comparison samples of cluster and field galaxies. Hwang et al. (2012c) constructed a sample of 129 relaxed Abell clusters at $0.02 < z < 0.14$ using the spectroscopic sample of the SDSS DR7. The cluster sample also includes the galaxies at $R < 10R_{200}$ (R_{200} is the virial radius of the cluster) and $\Delta V = |V_{\mathrm{gal}} - V_{\mathrm{cl}}| < 1000$ km s^{-1} (V_{gal} and V_{cl} are radial velocity of a galaxy and systematic velocity of the cluster). From this sample, we selected 2433 galaxies at $R < R_{200}$ as the cluster galaxy sample, and 6312 galaxies at $5R_{200} < R < 10R_{200}$ as the field galaxy sample. Park & Hwang (2009) showed that the fraction of early-type galaxies decreases with increasing clustercentric radius at $R < 3R_{200}$. However, the early-type galaxy fraction is nearly constant at $R > 4R_{200}$ (see their Figure 4),

---

[3]http://wise2.ipac.caltech.edu/docs/release/allwise/

Table 3.1. SDSS-related Physical Parameters of Compact Group Galaxies

Group ID[a]	Galaxy ID	R.A.	Decl	Redshift	M_r^b	$u - r^c$	Morph[d]
V1CG001	1237648705657307198	198.233322	1.007515	0.073839	-19.82 ± 2.21	2.28 ± 0.10	2
V1CG001	1237648705657307347	198.229294	1.010990	0.072679	-20.11 ± 0.01	2.57 ± 0.06	1
V1CG001	1237648705657307315	198.218872	1.019821	0.070435	-21.16 ± 0.01	2.67 ± 0.04	1
V1CG002	1237661126155436166	139.939529	33.745014	0.017118	-21.22 ± 0.06	2.77 ± 0.01	1
V1CG002	1237661126155436169	139.922531	33.738174	0.020334	-20.72 ± 0.05	2.61 ± 0.01	2
V1CG002	1237661126155436164	139.945221	33.749741	0.023006	-22.84 ± 0.01	2.91 ± 0.01	1

Note. — The full table is available in the online journal. A portion is shown here for guidance regarding its form and content.

[a] Group ID from Table 5 of Sohn et al. (2016).

[b] The $k_{z=0.1}$-, and evolution-corrected r-band Petrosian absolute magnitudes.

[c] The SDSS extinction- and k-corrected model magnitudes.

[d] Galaxy morphology. 1 indicates an early-type galaxy, while 2 indicates a late-type galaxies.

suggesting that the galaxies at $5R_{200} < R < 10R_{200}$ can be considered to be field galaxies. The galaxies in the two comparison samples also satisfy the criterion of $M_r < -19.77$ and $0.01 < z < 0.0741$ as do those in the V1 sample.

The optical parameters of galaxies that we consider in this study are r-band Petrosian absolute magnitude (M_r), $u-r$ color, and morphology. The M_r was computed using the Galactic reddening correction (Schlegel et al. 1998), K-corrections (Blanton & Roweis 2007), shifted to $z = 0.1$, and evolution correction, $E(z) = 1.6(z-0.1)$ (Tegmark et al. 2004). The $u - r$ color was computed using extinction- and K-corrected (to $z = 0.1$) u- and r-band model magnitudes. Galaxy morphology data are mainly from the KIAS DR7 VAGC. Galaxies in this catalog are morphologically classified into early (E/S0) and late types (S/Irr) based on an automated scheme with $u - r$ color, the $g - i$ color gradient, and the i-band concentration index (Park & Choi 2005). For galaxies not included in the KIAS DR7 VAGC, Sohn et al. (2016) classified them into early and late types through visual inspection. In Table 3.1, we list the group ID, galaxy ID, R.A., declination, redshift, M_r, $u-r$, and morphology of the 2175 compact group galaxies.

3.3 Results

3.3.1 Galaxy Color Distributions

Figure 3.1 shows the $u - r$ and $[3.4] - [12]$ distributions of the 1541 compact group galaxies detected at 12 μm. The mean $u-r$ error is 0.07, while the mean $[3.4] - [12]$ error is 0.12. In this diagram, compact group galaxies are distributed from the top-left corner to the bottom-right corner because galaxies with bluer optical colors tend to have redder MIR colors.

In panels (b) and (c), we plot the $u - r$ and $[3.4] - [12]$ distributions of compact group galaxies. For comparison, we also plot the distributions of cluster and field
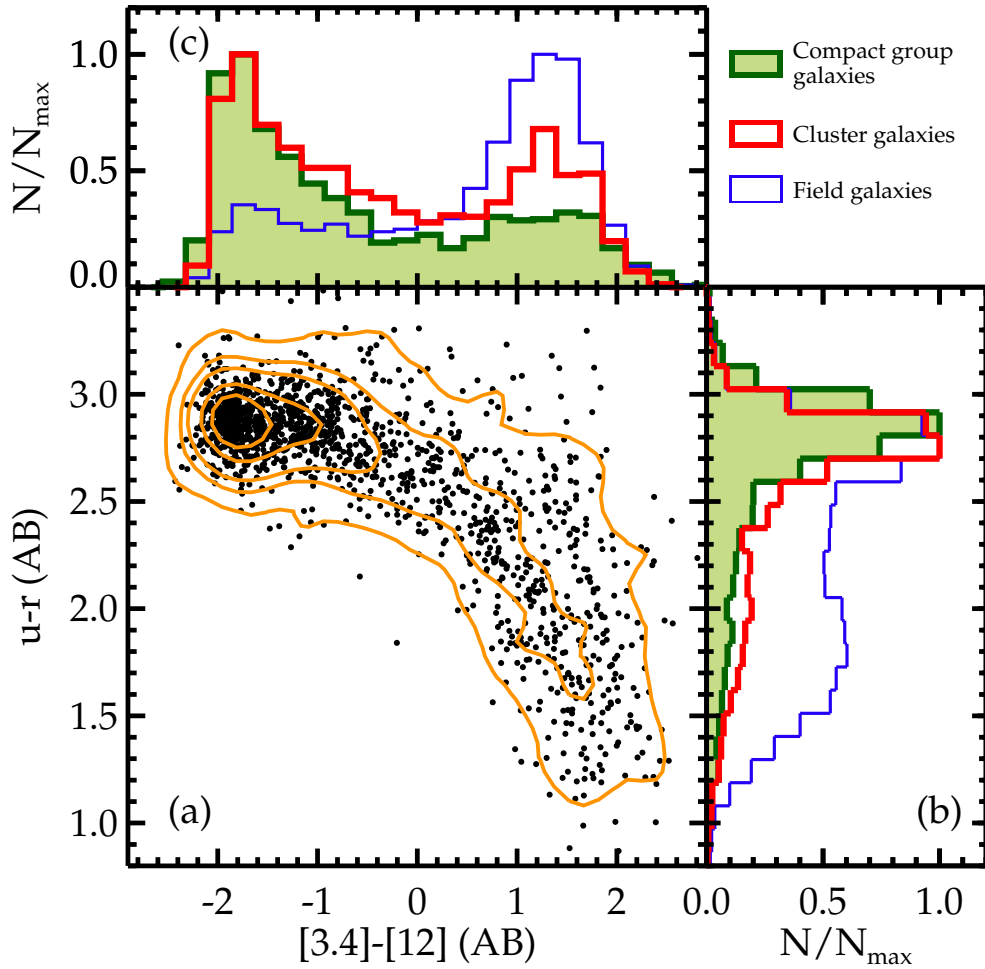
Figure 3.1 (a) $u - r$ versus $[3.4] - [12]$ diagram for the 1541 compact group galaxies detected at 12 μm. Contours represent the number density distribution. In panels (b) and (c), we display the $u - r$ and $[3.4] - [12]$ distribution for the compact group galaxies with the filled histograms. For comparison, we also plot the MIR color distribution of the 1461 cluster galaxies (open histogram with thick lines) and for the 5084 field galaxies (open histogram with thin lines).

galaxies. As shown in panel (b), $u-r$ histograms for the three galaxy samples peak at $u-r \simeq 2.6$. However, the fraction of galaxies with $u-r > 2.5$ in the compact group galaxy sample is $73.8\% \pm 1.1\%$, which is larger than that of the cluster galaxy sample ($64.1\% \pm 1.2\%$) and of the field galaxy sample ($38.4\% \pm 0.7\%$). The mean $u-r$ is 2.65 ± 0.02 in the compact group galaxy sample, which is also larger than the 2.50 ± 0.01 of the cluster galaxy sample and the 2.22 ± 0.01 of the field galaxy sample[4]. These suggest that compact group galaxies are dominated by optical red-sequence galaxies much like cluster galaxies, which is consistent with the findings of Walker et al. (2013) and Zucker et al. (2016).

Optical red-sequence galaxies, located in a narrow $u-r$ range of $2.5 - 3.2$, have MIR colors ranging from $[3.4]-[12] \simeq -2.4$ to $[3.4]-[12] \simeq 0$. Lee et al. (2015) divided optical red-sequence galaxies into MIR blue galaxies (i.e., $[3.4] - [12] < -1.55$) and MIR green galaxies (i.e., $-1.55 \leq [3.4] - [12] < -0.3$)[5]. The MIR blue galaxies are composed of stellar populations older than 10 Gyr, while the MIR green galaxies have small ($\sim$5%) mass fractions of relatively young ($0.5-1$ Gyr) or intermediate ($1-10$ Gyr) stellar populations (Piovan et al. 2003; Ko et al. 2013; Lee et al. 2015; Ko et al. 2016). Optical colors trace star formation on timescales up to 1 Gyr (Schawinski et al. 2014). Therefore, the MIR green galaxies are not distinguishable from the MIR blue galaxies in optical colors because both lie in the optical red-sequence (Walker et al. 2012, 2013; Ko et al. 2013; Lee et al. 2015; Zucker et al. 2016). Thus, we need to use MIR colors instead of optical colors to investigate whether galaxies in compact groups experienced different star formation histories from those in clusters, or not.

---

[4]The errors in the fractions and in the mean values are the standard deviations derived from 1000-times resamplings.

[5]This criterion is determined from the decomposition of the $[3.4] - [12]$ color distribution with three Gaussian functions using the Gaussian mixture modeling (Muratov & Gnedin 2010, see Figure 2 in Lee et al. 2015). We stress that this MIR green color selection criterion is not identical to the "MIR green valley" one in Section 3.3.2.

In panel (c) of Figure 3.1, we compare the MIR color distributions between the three different galaxy samples. The cluster galaxy sample shows a blue peak at $[3.4] - [12] \simeq -1.7$ and a red peak $[3.4] - [12] \simeq 1.3$. The blue peak is higher than the red peak. The compact group galaxy sample shows a strong blue peak and a red bump, but the field galaxy sample shows a different color distribution with a blue bump and a strong red peak. The mean $[3.4] - [12]$ is -0.54 ± 0.03 for the compact group galaxy sample, -0.29 ± 0.04 for the cluster galaxy sample, and 0.46 ± 0.02 for the field galaxy sample. These results suggest that compared to cluster galaxies, compact group galaxies are more dominated by MIR blue galaxies: the fraction of MIR blue galaxies is $32.6\% \pm 1.2\%$ in the compact group galaxy sample and $23.7\% \pm 1.1\%$ in the cluster galaxy sample. This suggests that the mean stellar ages of compact group galaxies are on average older than those of cluster galaxies.

On the other hand, because compact groups favor strong galaxy interactions, the presence of active galactic nuclei (AGN) should be expected (Coziol et al. 1998a,b; Martínez et al. 2010; Tzanavaris et al. 2014). Because the contribution of AGN to the MIR fluxes of the host galaxies is not negligible, we identify the AGN in our sample and remove them. First, we identify optically selected AGN using the scheme given by Kewley et al. (2006) who classified star-forming galaxies from AGN (Seyferts and LINERs) and composite galaxies in the $[NII]/H\alpha$ versus $[OII]/H\beta$ diagram (see their Figure 1). We remove 281 AGN and 149 composite galaxies from the sample of 1541 compact group galaxies. Second, we identify MIR selected AGN using the classification method introduced by Mateos et al. (2012) who defined the AGN wedge in the *WISE* $[3.4] - [4.6]$ versus $[4.6] - [12]$ color-color diagram (see their Figure 2). We find 8 MIR selected AGN in the compact group galaxy sample. Among the 8 MIR selected AGN, 5 are also optically selected AGN. In total, 433 galaxies (28%) are classified as AGN-host galaxies among the 1541 compact group galaxies.

We compare the MIR color distribution of all 1541 compact group galaxies with that of 1108 non-AGN compact group galaxies in Figure 3.2(a). The difference between the two distributions is remarkable at $-1.5 \lesssim [3.4] - [12] \lesssim 0.5$ where the AGN fraction is larger than 30%. This color range is similar to the *WISE* infrared transition zone, $-1.71 \lesssim [3.4] - [12] \lesssim 0.02$, defined by Alatalo et al. (2014)[6]. They showed that Seyferts and LINERs are representatives of the zone, which is consistent with our result.

In Figure 3.2(b), we compare the MIR color distribution of non-AGN compact group galaxies with that of non-AGN cluster galaxies. In this comparison, we use 1137 non-AGN cluster galaxies ($R < R_{200}$) after removing 324 AGN-host galaxies (22%) from the 1461 cluster galaxy sample. To statistically examine the difference in the color distributions of the two samples, we compute p-values from the Kolmogorov-Smirnov (KS) test (P_{KS}) and the Anderson-Darling (AD) k-sample test (P_{AD}). The P_{KS} and P_{AD} indicate the probability of rejecting the null hypothesis that the two samples are drawn from the same parent sample. The two tests on the two color distributions give the P_{KS} and P_{AD} of $\ll 0.01$, rejecting the null hypothesis at a significance of $> 3\sigma$ level.

In Figure 3.2(b), we use another comparison sample of 617 cluster galaxies located at $R < 0.5R_{200}$. In comparison with the $R < R_{200}$ cluster galaxy sample, the $R < 0.5R_{200}$ cluster galaxy sample displays the MIR color distribution more colsely to that of the compact group galaxy sample ($P_{KS} = 0.076$ and $P_{AD} = 0.035$; the null hypothesis is rejected at the $< 1.8\sigma$ level). The fractions of MIR red (i.e., $[3.4] - [12] \geq -0.3$) galaxies in the compact group galaxy sample is $35.4\% \pm 1.4\%$. This is similar to the $34.7\% \pm 1.8\%$ in the $R < 0.5R_{200}$ cluster galaxy sample, but smaller than the $43.9\% \pm 1.5\%$ in the $R < R_{200}$ cluster galaxy sample. The

---

[6]This color range is converted from the $0.8 < [4.6] - [12] < 2.4$ in Vega magnitude in Alatalo et al. (2014).
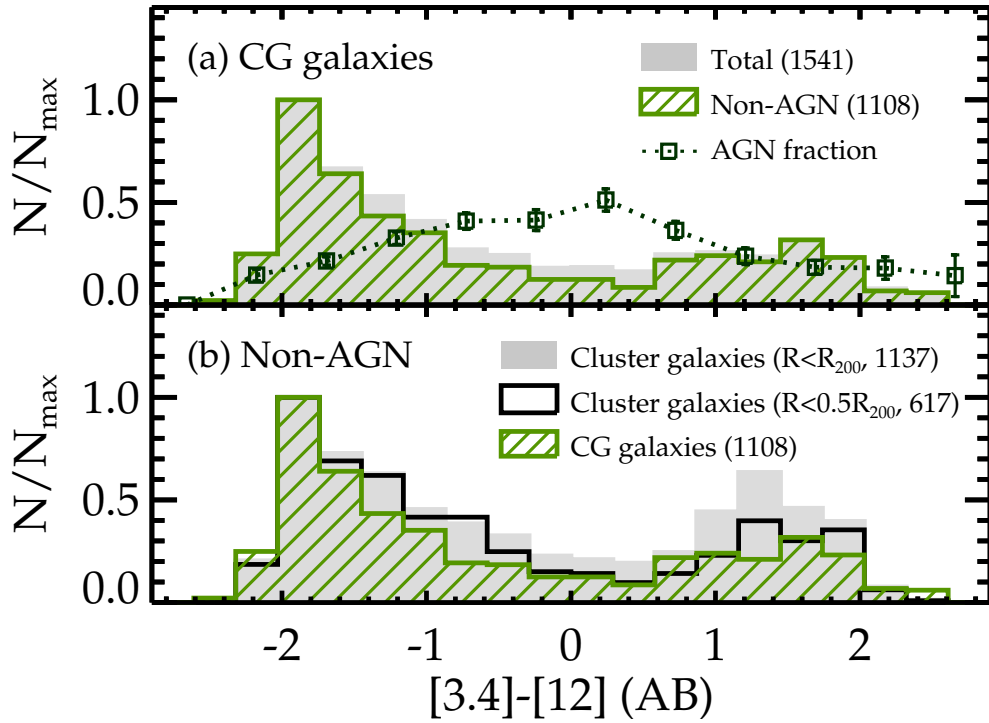
Figure 3.2 (a) $[3.4] - [12]$ color distribution for the all 1541 (filled) and the 1108 non-AGN (hatched) compact group galaxies. Squares represent the fraction of AGN as a function of $[3.4] - [12]$. The error bars indicate the 1σ deviation from 1000-times bootstrap resamplings. (b) Comparison of the color distributions between the 1108 non-AGN compact group galaxies (hatched), the 1137 non-AGN cluster galaxies at $R < R_{200}$ (filled), and the 617 non-AGN cluster galaxies at $R < 0.5R_{200}$ (open).

mean $[3.4] - [12]$ for the compact group galaxy sample (-0.57 ± 0.04) is similar to the -0.52 ± 0.06 for the $R < 0.5R_{200}$ cluster galaxy sample, but smaller than the -0.30 ± 0.04 for the $R < R_{200}$ cluster galaxy sample. The early-type galaxy fraction in the $R < 0.5R_{200}$ cluster galaxy sample $(66.0\% \pm 1.9\%)$ is similar to that in the compact group galaxy sample $(62.0\% \pm 1.5\%)$, while the fraction is $57.5\% \pm 1.5\%$ in the $R < R_{200}$ cluster galaxy sample. These results suggest that compact groups are composed of galaxy populations similar to those in cluster central regions.

However, we find that the fraction of MIR green (i.e., $-1.55 \leq [3.4] - [12] < -0.3$) galaxies is smaller in the compact group galaxy sample $(28.5\% \pm 1.3\%)$ than in the $R < 0.5R_{200}$ cluster galaxy sample $(34.5\% \pm 1.9\%)$. This may suggest that galaxy transition occurs faster in compact groups than in cluster environments. Hereafter, we use only the $R < 0.5R_{200}$ cluster galaxy sample in the comparison with the compact group galaxy sample.

Figure 3.3(a) shows again the MIR color distributions of the 1108 non-AGN compact group galaxies and of the 617 non-AGN cluster galaxies. In Figure 3.3 we divide these two galaxy samples into early-type and late-type galaxy samples. In Figure 3.3(b) we compare the MIR color distribution of the 687 compact group early-type galaxies with that of the 407 cluster early-type galaxies. The P_{KS} and P_{AD} values of < 0.001 reject the null hypothesis for the two color distributions at a $> 3\sigma$ significance. We find that the fraction of MIR green galaxies is smaller in the compact group early-type galaxy sample $(37.6\% \pm 1.8\%)$ than in the cluster early-type galaxy sample $(47.4\% \pm 2.5\%)$, and that the mean $[3.4] - [12]$ value is smaller in the compact group early-type galaxy sample (-1.40 ± 0.03) than in the cluster early-type galaxy sample (-1.28 ± 0.04).

In Figure 3.3(c) we compare the color distribution of the 421 compact group late-type galaxy sample with that of the 210 cluster late-type galaxy sample. The difference in the color distribution for the two late-type galaxy samples is not highly
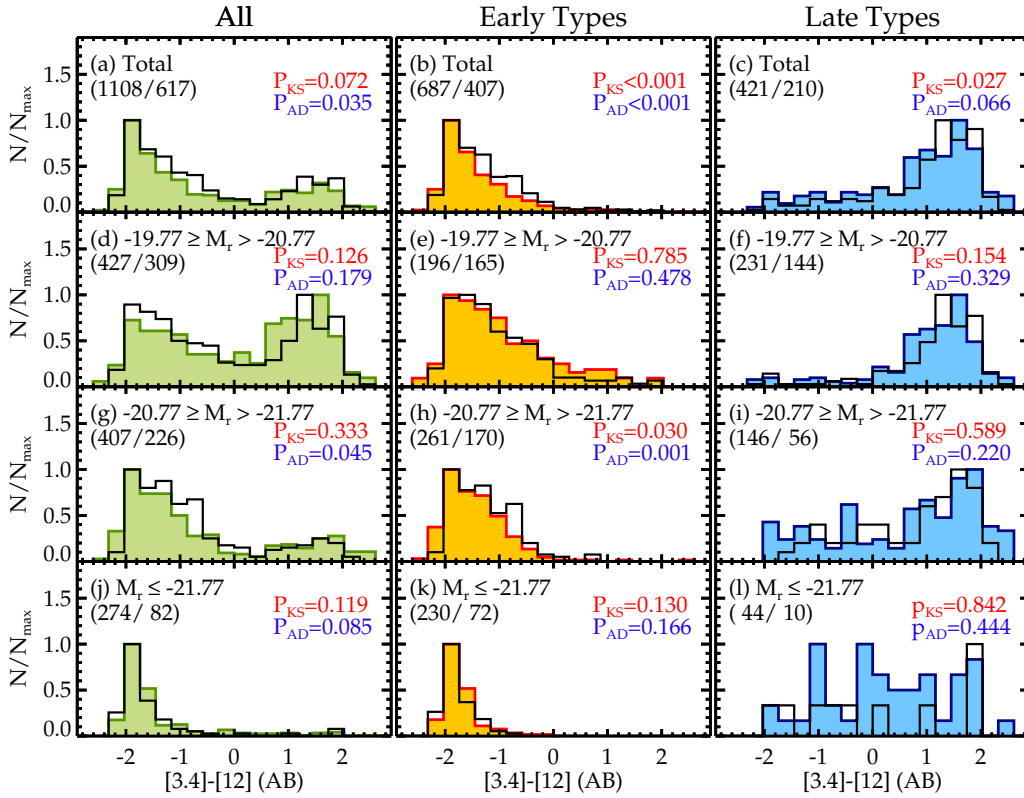
Figure 3.3 Comparison of $[3.4] - [12]$ color distributions for compact group galaxies (filled histograms) with those of cluster galaxies (open histograms). The middle column is for early-type galaxies, and the right-hand column is for late-type galaxies. The left-hand column is the sum. The second row is for faint galaxies with $-19.77 \geq M_r > -20.77$, the third row is for galaxies with $-20.77 \geq M_r > -21.77$, and the bottom row is for bright galaxies with $M_r \leq -21.77$. We list p-values from the KS and AD k-sample tests for the two distributions (for compact group galaxies and for cluster galaxies) in each panel.

significant ($< 1.9\sigma$), compared to the case for early-type galaxy samples. However, the mean $[3.4] - [12]$ value is smaller in the compact group late-type galaxy sample (0.80 ± 0.06) than in the cluster late-type galaxy sample (0.95 ± 0.07). The MIR green galaxy fraction is larger in the compact group late-type galaxy sample ($13.8\%\pm1.7\%$) than in the cluster late-type galaxy sample ($9.5\% \pm 1.9\%$).

Because galaxy properties are dependent on their stellar masses (or luminosities), we compare the MIR color distributions of compact group galaxies and cluster galaxies by using a fixed M_r. We use M_r instead of stellar masses because the former is available for all galaxies in both compact group and cluster galaxy samples. We find that the null hypothesis is rejected in the comparison for early-type galaxies with $-20.77 \geq M_r > -21.77$ at the $\gtrsim 2.2\sigma$ level (panel h; $P_{\mathrm{KS}} = 0.03$ and $P_{\mathrm{AD}} = 0.001$). For the total galaxy sample with $-20.77 \geq M_r > -21.77$ (panel g), P_{AD} rejects the null hypothesis at the 2σ level, but P_{KS} does not. The other cases show lower significance of rejection. This indicates that the difference in the MIR color distribution between the compact group galaxies and the cluster galaxies is mainly attributed to the galaxies with $-20.77 \geq M_r > -21.77$. We examine galaxy properties using the luminosity-limited subsamples in the following analysis, but find no significant difference from the results based on the total sample. We therefore present the results in the following analysis based on the total sample for better statistics.

3.3.2 MIR Color-Luminosity Diagram

In Figure 3.4 we investigate the $[3.4] - [12]$ versus 12 μm luminosity distribution of galaxies in compact groups, clusters, and field. In the $[3.4] - [12]$ versus 12 μm luminosity diagram, galaxies are divided into three classes following the classification scheme of Lee et al. (2015): MIR star-forming sequence galaxies (above the inclined dashed lines[7]), MIR blue cloud galaxies ($[3.4] - [12] < -1.55$), and MIR green valley

---

[7]$[3.4] - [12] = \log(L_{12}/L_{\mathrm{sun}}) \times 0.62 - 5.51$. See Section 2.5.1 for details.

galaxies located between the two classes. In this section we use this classification scheme to calculate the fractions of different MIR classes. In particular, MIR green valley galaxies are not necessarily "MIR green" in the sense of Section 3.3.1.

In the three panels in the top row of Figure 3.4, we plot 1108 compact group galaxies, 617 cluster galaxies, and 3854 field galaxies, separately. All these galaxies are not AGN-host galaxies. We find that the fraction of MIR blue cloud galaxies is larger in the compact group galaxy sample ($36.5\% \pm 1.4\%$) than in the cluster galaxy sample ($30.8\% \pm 1.9\%$) and in the field galaxy sample ($10.9\% \pm 0.5\%$). In the cluster galaxy sample and the field galaxy sample, the fractions of MIR blue cloud galaxies are smaller than the fractions of MIR green valley galaxies. In contrast, in the compact group galaxy sample, the fraction of MIR blue cloud galaxies is larger than the fraction of MIR green valley galaxies ($30.3\% \pm 1.4\%$).

When we consider only early-type galaxies, as shown in the middle row of Figure 3.4, we obtain similar results. The fraction of early-type galaxies is 62.0% ($687/1108$) in the compact group galaxy sample, 66.0% ($407/617$) in the cluster galaxy sample, and 26.5% ($1023/3854$) in the field galaxy sample. Among the three early-type galaxy samples, the compact group early-type galaxy sample shows the highest MIR blue cloud galaxy fraction. In addition, in the cluster early-type galaxy sample and in the field early-type galaxy sample, the fractions of MIR blue cloud galaxies is smaller than those of MIR green valley galaxies. However, in the compact group early-type galaxy sample, the fraction of MIR blue cloud galaxies ($55.5\% \pm 1.9\%$) is significantly larger than the fraction of MIR green valley galaxies ($38.4\% \pm 1.9\%$). These results suggest not only that early-type galaxies in compact groups are on average older than those in other environments, but also that the timescales for early-type galaxies to stay in the MIR green valley are shorter in compact groups than in other environments.

In the bottom row of Figure 3.4, we plot only late-type galaxies. The fraction
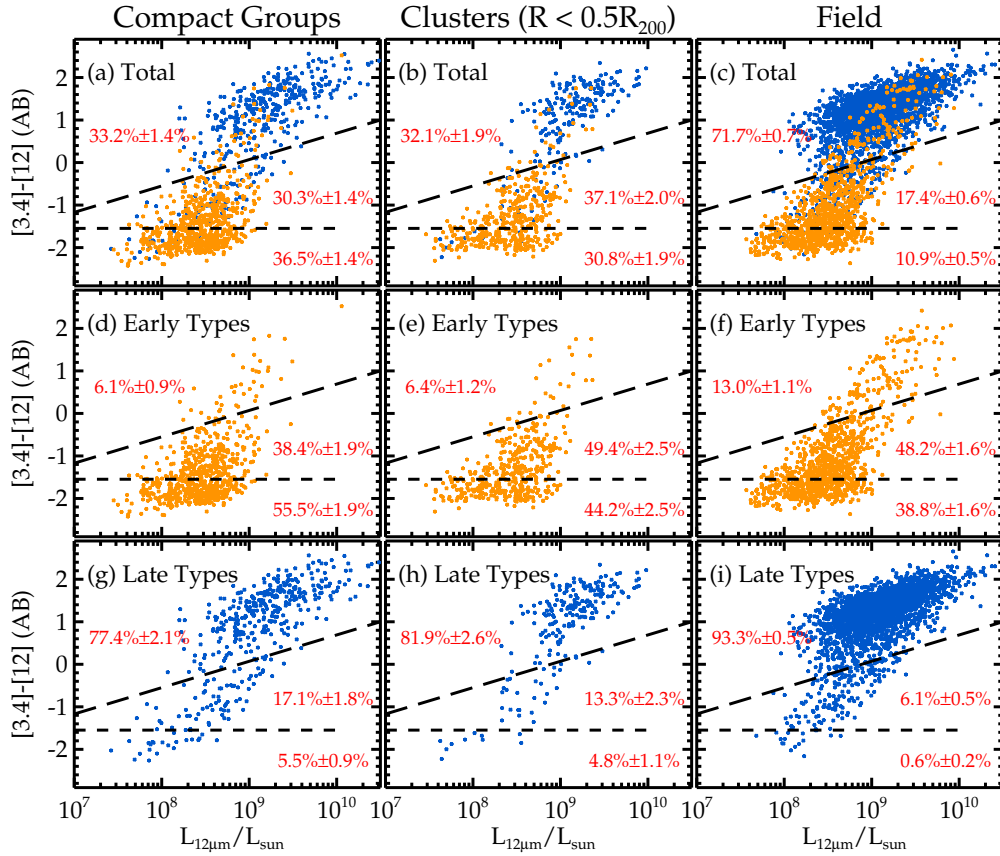
Figure 3.4 MIR color-luminosity diagrams for compact group galaxies (left), cluster ($R < 0.5R_{200}$) galaxies (middle), and field galaxies (right). Orange and blue dots represent early- and late-type galaxies, respectively. We divide the galaxies into three classes following the classification scheme of Lee et al. (2015): MIR star-forming sequence galaxies (above the long-dashed lines), MIR blue cloud galaxies (below short-dashed lines), and MIR green valley galaxies (between the two lines). Middle and bottom rows are for early- and late-type galaxies in different environments. We list the fractions of different MIR classes in each panel.

of MIR star-forming sequence galaxies decreases from the field ($93.3\% \pm 0.5\%$) to clusters ($81.9\% \pm 2.6\%$) to compact groups ($77.4\% \pm 2.1\%$). Thus, the fractions of MIR blue cloud galaxies and of MIR green valley galaxies are smallest in the field ($0.6\% \pm 0.2\%$ and $6.1\% \pm 0.5\%$) and largest in compact groups ($5.5\% \pm 0.9\%$ and $17.1\% \pm 1.8\%$). The smallest fraction of MIR star-forming sequence galaxies in compact groups is consistent with the case that the star formation quenching for late-type galaxies occurs more effectively in compact groups than in clusters and in the field. We note that the results in this section do not change significantly if we use $-1.55 \leq [3.4] - [12] < -0.3$ as the criterion to select MIR green galaxies. In Table 3.2, we list the *WISE*-related parameters and AGN classes of compact group galaxies.

3.3.3   Environments of Compact Group Galaxies

To investigate the environmental effects on galaxy properties in compact groups, we use three kinds of environmental parameters. The first parameter is the number of neighboring galaxies ($N_{\rm nei}$) of compact groups. Sohn et al. (2016) calculated $N_{\rm nei}$ around compact groups within a comoving cylinder defined by projected group centric radius $R = 1$ Mpc and $\Delta V = |V_{\rm gal} - V_{\rm gr}| = 1000$ km s^{-1}, where $V_{\rm gal}$ and $V_{\rm gr}$ are a radial velocity of a galaxy and a mean velocity of member galaxies in a compact group. In the $N_{\rm nei}$ count, Sohn et al. (2016) used galaxies in the V2 sample ($M_r < -20.77$ and $0.01 < z < 0.115$). In this study, we recalculate $N_{\rm nei}$ for 670 compact groups using galaxies in the V1 sample ($M_r < -19.77$ and $0.01 < z < 0.0741$). We exclude the compact group members in the $N_{\rm nei}$ count. We do not assign $N_{\rm nei}$ to 59 compact groups close to the lower and upper redshift limits because their $N_{\rm nei}$ can be underestimated, resulting in that we assign $N_{\rm nei}$ to 611 compact groups.

The second environmental parameter is the fraction of early-type member galaxies in compact groups ($f_{\rm E}$). Bitsakis et al. (2010, 2011, 2015) used this $f_{\rm E}$ to divide

Table 3.2. *WISE*-related Physical Parameters of Compact Group Galaxies

Group ID	Galaxy ID	$[3.4] - [12]^a$	$(S/N)_{12}^b$	$\log(L_{12}/L_\odot)^c$	AGN^d	$M_{3.4}^e$	$\log(M_{star}/M_{sun})^f$
V1CG001	1237648705657307198	-9.99 ± 0.00	-9.9	-9.99 ± 0.00	0	-9.99 ± 0.00	$0.00^{+0.00}_{-0.00}$
V1CG001	1237648705657307347	0.00 ± 0.00	1.4	8.60 ± 0.00	0	-23.04 ± 0.03	$9.92^{+0.07}_{-0.05}$
V1CG001	1237648705657307315	-0.92 ± 0.00	0.2	8.50 ± 0.00	0	-23.71 ± 0.04	$10.61^{+0.12}_{-0.17}$
V1CG002	1237661126155436166	-0.87 ± 0.05	26.5	8.40 ± 0.02	1	-23.42 ± 0.02	$10.70^{+0.12}_{-0.15}$
V1CG002	1237661126155436169	0.69 ± 0.03	44.9	8.95 ± 0.01	1	-23.22 ± 0.02	$10.63^{+0.08}_{-0.10}$
V1CG002	1237661126155436164	-2.03 ± 0.05	23.2	8.61 ± 0.02	0	-25.10 ± 0.02	$11.59^{+0.07}_{-0.13}$

Note. — The full table is available in the online journal. A portion is shown here for guidance regarding its form and content. [a] The *ALLWISE* profile-fitting AB magnitudes. -9.99 indicates no *ALLWISE* photometry.

[b] The signal-to-ratio at 12 μm. -9.9 indicates no *ALLWISE* photometry. When $(S/N)_{12} \leq 3$, we assign zero errors to $[3.4] - [12]$ and $\log(L_{12}/L_\odot)$.

[c] 12 μm luminosities. -9.99 indicates no *ALLWISE* photometry.

[d] AGN classification (0: non-AGN, 1: optical AGN, 2: MIR AGN, and 3: optical+MIR AGN)

[e] 3.4 μm absolute magnitudes. -9.99 ± 0.000 indicates no *ALLWISE* photometry.

[f] Stellar masses calculated using $H_0 = 70$ km s^{-1} Mpc^{-1}. 0.00 means no measurement.

compact groups into dynamically old and young systems based on the assumption that dynamically old systems are dominated by early-type galaxies that could form through repeated interactions between member galaxies. Thus, f_E is the parameter reflecting the internal environment of compact groups.

The third environmental parameter is the rest-frame velocity dispersions of compact group member galaxies (σ_{CG}). We adopt the σ_{CG} from Table 5 in Sohn et al. (2016). Sohn et al. (2016) found that compact groups with low σ_{CG} ($\lesssim 100$ km s^{-1}) show features of ongoing interactions among member galaxies, but that compact groups with $\sigma_{CG} \gtrsim 300$ km s^{-1} do not. Thus, σ_{CG} is another parameter that reflects the internal environment of compact groups.

We note that we use all the member galaxies regardless of 12 μm detection when we calculate f_E and σ_{CG}. In Table 3.3, we list the ID, R.A., declination, redshift, as well as three environmental parameters of the 670 compact groups. Figure 3.5 shows the relations between the three environmental parameters. We plot only 611 systems with complete N_{nei}. The N_{nei} histogram peaks at $N_{nei} \simeq 3-6$, and stretches out to more than $N_{nei} = 40$. The f_E mainly has discontinuous values (e.g., 0, 1/3, 2/3, and 1) because the majority (495/611, 81%) of our systems have three member galaxies. The σ_{CG} histogram peaks at ~ 80 km s^{-1}, and stretches out to more than 600 km s^{-1}. The median σ_{CG} is ~ 200 km s^{-1}.

To examine the effects of N_{nei} on galaxy properties in compact groups, we investigate how the MIR color distribution of compact group galaxies varies with N_{nei}. Figure 3.6 shows the MIR color histograms of the galaxies in different N_{nei} bins. The left-hand column shows that the fraction of MIR red (i.e., $[3.4]-[12] > -0.3$) galaxies dramatically decreases as N_{nei} increases. The MIR red galaxies are mainly late-type galaxies. The fraction of late-type galaxies gradually decreases from $56.2\% \pm 3.0\%$ (panel a) to $15.9\% \pm 2.6\%$ (panel d) as N_{nei} increases. For comparison, we also plot the MIR color distribution of cluster galaxies as open histograms. We find that the
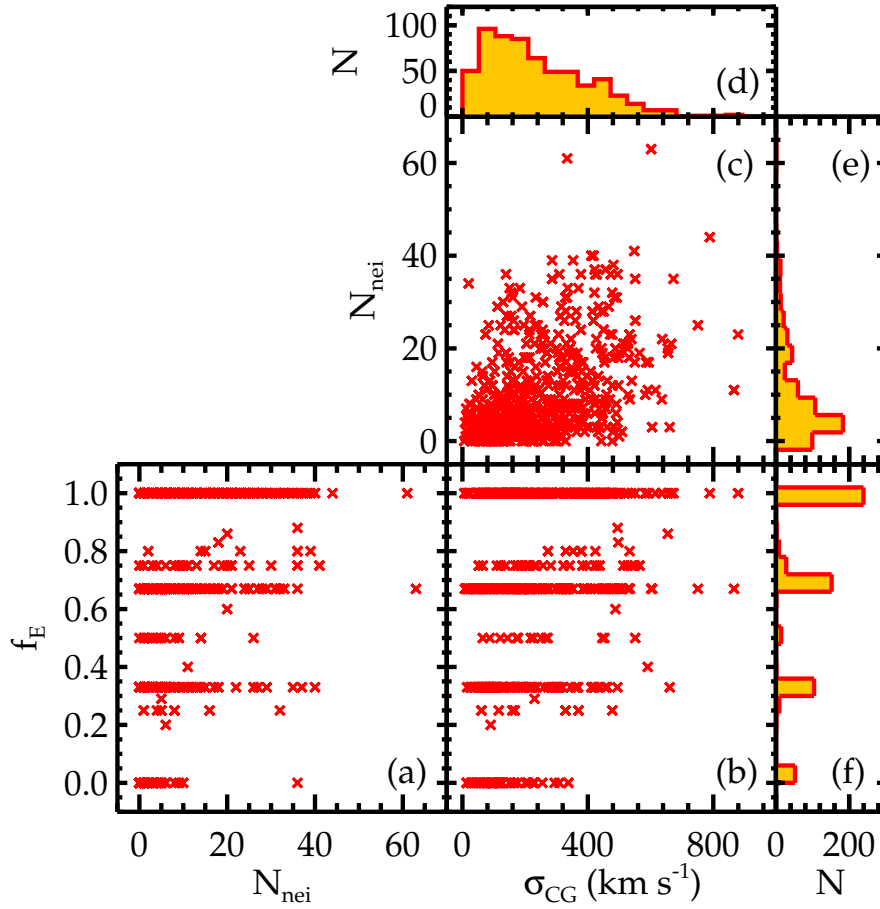
Figure 3.5 Relation between the three environmental parameters for compact groups: (a) f_E vs. N_{nei}, (b) f_E vs. σ_{CG}, and (c) N_{nei} vs. σ_{CG} diagrams. (d−f) Histograms for the three parameters.

Table 3.3.   Environmental Parameters of Compact Groups

Group ID[a]	R.A.[a]	Decl.[a]	Redshift[a]	N_{mem}^{b}	N_{nei}^{c}	f_{E}^{d}	σ_{CG} (km s^{-1})[e]
V1CG001	198.227173	1.012775	0.0723 ± 0.0008	3	-99	0.67	482 ± 122
V1CG002	139.935760	33.744308	0.0202 ± 0.0012	3	11	0.67	866 ± 228
V1CG003	154.741531	37.298065	0.0480 ± 0.0003	3	5	0.00	210 ± 37
V1CG004	158.222275	12.086633	0.0330 ± 0.0004	3	11	0.67	242 ± 69
V1CG005	127.709404	28.573534	0.0657 ± 0.0001	3	1	0.33	26 ± 4
V1CG006	149.408493	37.324886	0.0611 ± 0.0002	3	4	0.33	100 ± 26

Note. — The full table is available in the online journal. A portion is shown here for guidance regarding its form and content.

[a] Group ID from Table 5 of Sohn et al. (2016).

[b] The number of member galaxies in each compact group.

[c] The number of neighboring galaxies ($M_r < -19.77$) in the comoving cylinder. For 59 compact groups near the lower and upper redshift limits, N_{nei} are not assigned ($N_{\mathrm{nei}} = -99$).

[d] The fraction of early-type galaxies among member galaxies of a compact group.

[e] The rest-frame line-of-sight velocity dispersion of galaxies in each compact group and the 1σ error derived from 1000-times bootstrap resamplings, from Table 5 of Sohn et al. (2016).
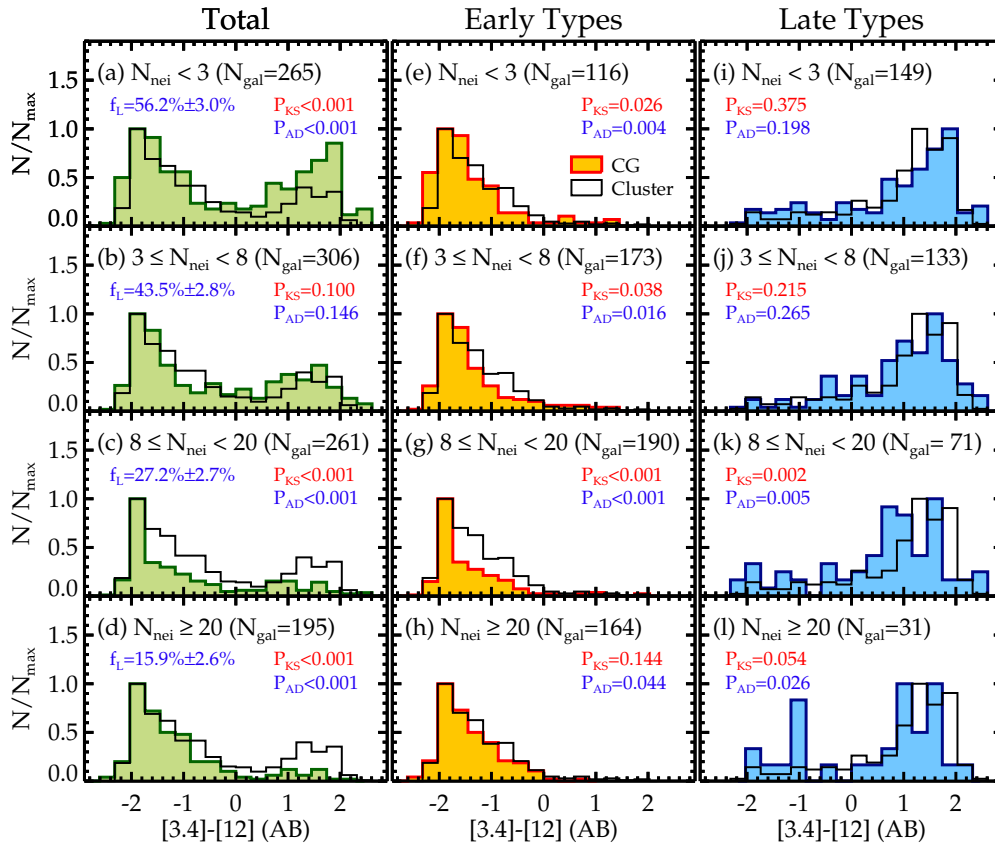
Figure 3.6 Dependence of the $[3.4] - [12]$ color of compact group galaxies on the number of neighboring galaxies (N_{nei}). In the left-hand column, we list the fraction of late-type galaxies (f_L). In the middle and right-hand columns, we plot early-type galaxies and late-type galaxies, separately. For comparison, we also plot the color distributions for cluster galaxies (open histograms).

fraction of late-type galaxies in the $N_{\mathrm{nei}} \geq 8$ compact groups is smaller than the fraction of late-type galaxies $(34.0\% \pm 1.9\%)$ in the cluster galaxy sample.

We investigate the MIR color distributions for early- and late-type galaxies separately in the middle and right columns in Figure 3.6. The KS and AD k-sample tests for early-type galaxy samples in the four different N_{nei} bins (e−h) reject the null hypothesis at the $< 1.3\sigma$ level. They also reject the null hypothesis for late-type galaxy samples in the four different N_{nei} bins (i−l) at the $< 1.8\sigma$ level. These imply that N_{nei} does not affect the MIR colors of early- and late-type galaxies in compact groups directly. Thus, the N_{nei}-dependence of MIR colors shown in the left column (a−d) results from the fact that compact groups located in denser regions (larger N_{nei}) tend to have more early-type member galaxies with MIR blue colors.

The middle column in Figure 3.6 shows that compact group early-type galaxies have MIR colors bluer than cluster early-type galaxies regardless of N_{nei}. The color difference is significant ($\gtrsim 2.1\sigma$) in the $N_{\mathrm{nei}} < 20$ compact groups, but it is marginal ($\sim 1.5\sigma$) in the $N_{\mathrm{nei}} \geq 20$ groups. We find no color difference between cluster late-type galaxies and compact group late-type galaxies at the $N_{\mathrm{nei}} < 8$ groups. However, late-type galaxies at the $N_{\mathrm{nei}} \geq 8$ groups have MIR colors bluer than cluster late-type galaxies. The significance of the color difference is $\sim 2-3\sigma$.

Figure 3.7 shows the MIR color distributions of compact group early-type galaxies in different f_{E} bins: $f_{\mathrm{E}} < 0.5$, $0.5 \leq f_{\mathrm{E}} < 1$, and $f_{\mathrm{E}} = 1$. We find no significant differences in the MIR colors between the three f_{E} bins. The mean $[3.4] - [12]$ value is -1.49 ± 0.08 at $f_{\mathrm{E}} < 0.5$, -1.44 ± 0.04 at $0.5 \leq f_{\mathrm{E}} < 0.1$, and -1.43 ± 0.03 at $f_{\mathrm{E}} = 1$, respectively. These mean values agree well within 1σ errors. The KS and the AD k-sample tests do not reject the null hypothesis, either.

Bitsakis et al. (2011) showed that early-type galaxies in dynamically young ($f_{\mathrm{E}} < 0.25$) compact groups have bluer NUV$-r$ colors than those in dynamically old ($f_{\mathrm{E}} > 0.25$) groups. However, the number of early-type galaxies in their dynamically young

Figure 3.7 MIR color distributions for early-type galaxies in the (a) $f_E < 0.5$, (b) $0.5 \leq f_E < 1$, and (c) $f_E = 1$ compact groups. For comparison, we also plot the (filled) histograms for the early-type galaxies in our cluster sample.

groups is only three. In our sample, there are no early-type galaxies belonging to the $f_E < 0.25$ groups, and only six early-type galaxies belonging to the $f_E < 0.3$ groups. However, we find that the MIR color distribution for the six galaxies is not different significantly from that for early-type galaxies in the $f_E < 0.5$ groups.

On the other hand, we find that in all three f_E bins, compact group early-type galaxies have MIR colors bluer than cluster early-type galaxies. The P_{KS} and P_{AD} are < 0.019, suggesting that the color difference between compact group and cluster early-type galaxy samples is significant ($> 2.4\sigma$). This is consistent with the result in Figure 3.6.

Figure 3.8 shows the MIR color distributions of compact group late-type galaxies in different f_E bins: $f_E = 0$, $0 < f_E < 0.5$, and $0.5 \leq f_E < 1$. For comparison, we also plot the color distributions for the cluster late-type galaxy sample. Late-type galaxies in the $f_E = 0$ compact groups have MIR colors redder than cluster late-type galaxies. However, late-type galaxies in the $f_E > 0$ groups have MIR colors bluer than cluster late-type galaxies. In all three bins, P_{KS} and P_{AD} are ≤ 0.03, indicating that the color differences are significant ($> 3\sigma$). On the other hand, we find that MIR colors of late-type galaxies in the $0 < f_E < 0.5$ groups are not different from those in the $0.5 \leq f_E < 1$ groups ($P_{KS} = 0.835$ and $P_{AD} = 0.664$). The mean $[3.4] - [12]$ values of late-type galaxies in the $0 < f_E < 0.5$ groups (0.58 ± 0.09) and in the $0.5 \leq f_E < 1$ groups (0.64 ± 0.10) are similar, but smaller than the 1.32 ± 0.09 in the $f_E = 0$ groups.

These results suggest that star formation activity of late-type galaxies is suppressed more efficiently in the $f_E > 0$ compact groups than in clusters. However, late-type galaxies in the $f_E = 0$ groups have comparable or higher star formation activity than that of cluster late-type galaxies. It is interesting that late-type member galaxies in compact groups show a hint of star formation quenching only when the compact groups have early-type member galaxies (see Section 3.4.3 for detailed
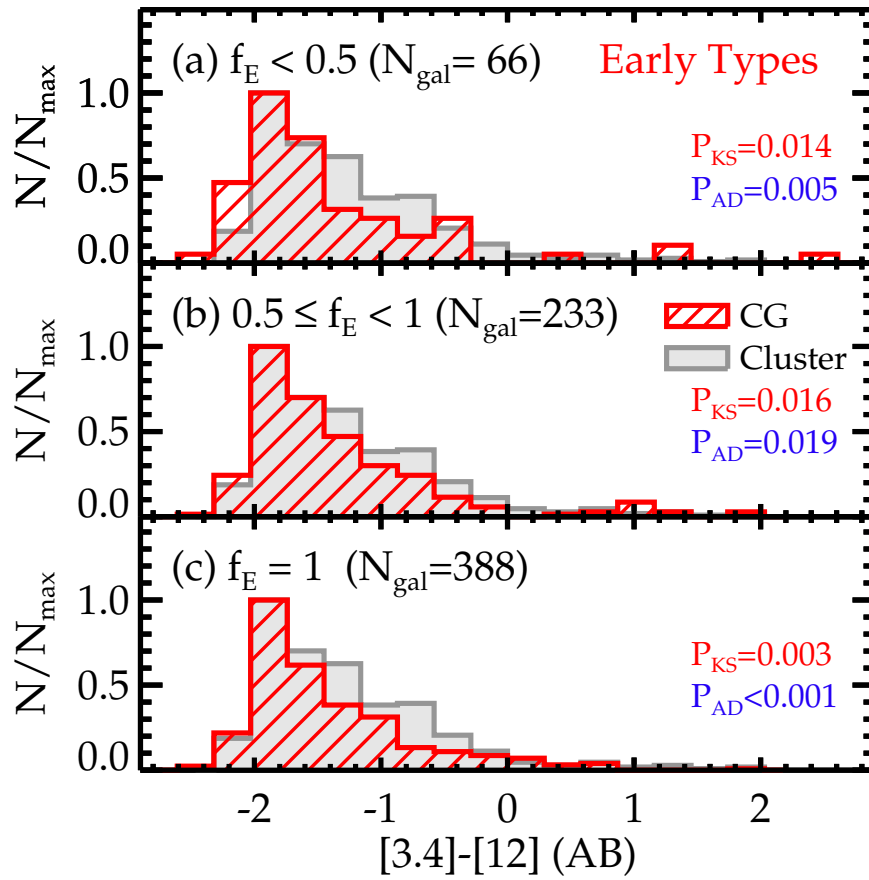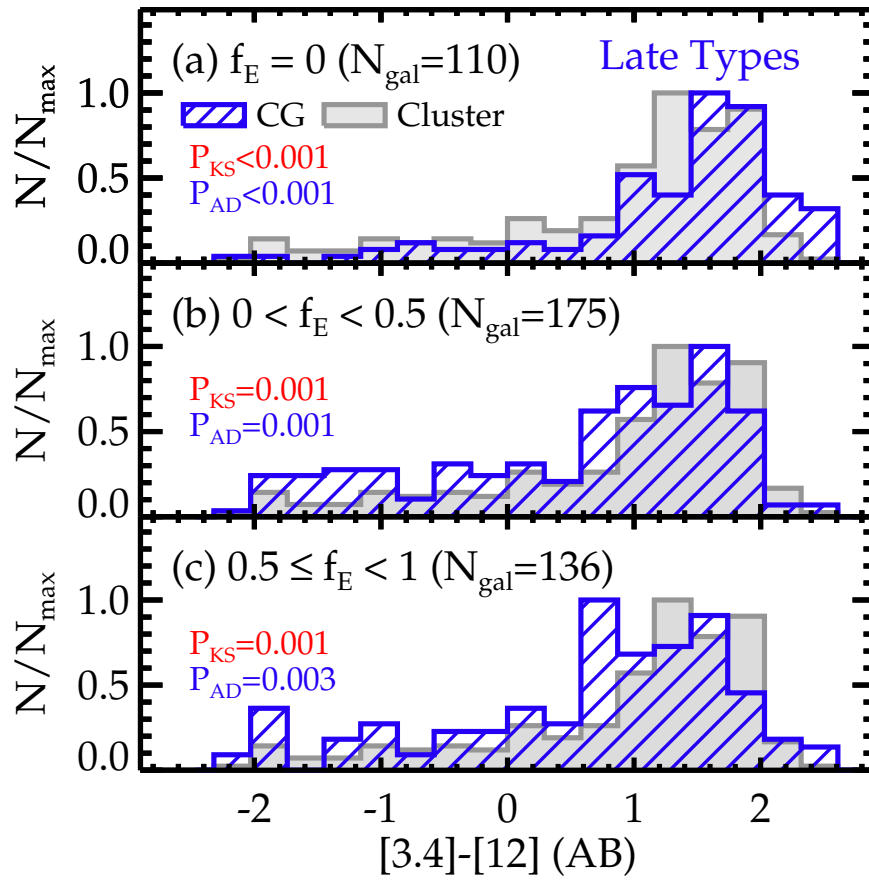
Figure 3.8 MIR color distributions for late-type galaxies in the (a) $f_E = 0$, (b) $0 < f_E < 0.5$, and (c) $0.5 \leq f_E < 1$ compact groups. For comparison, we also plot the (filled) histograms for the late-type galaxies in our cluster sample.
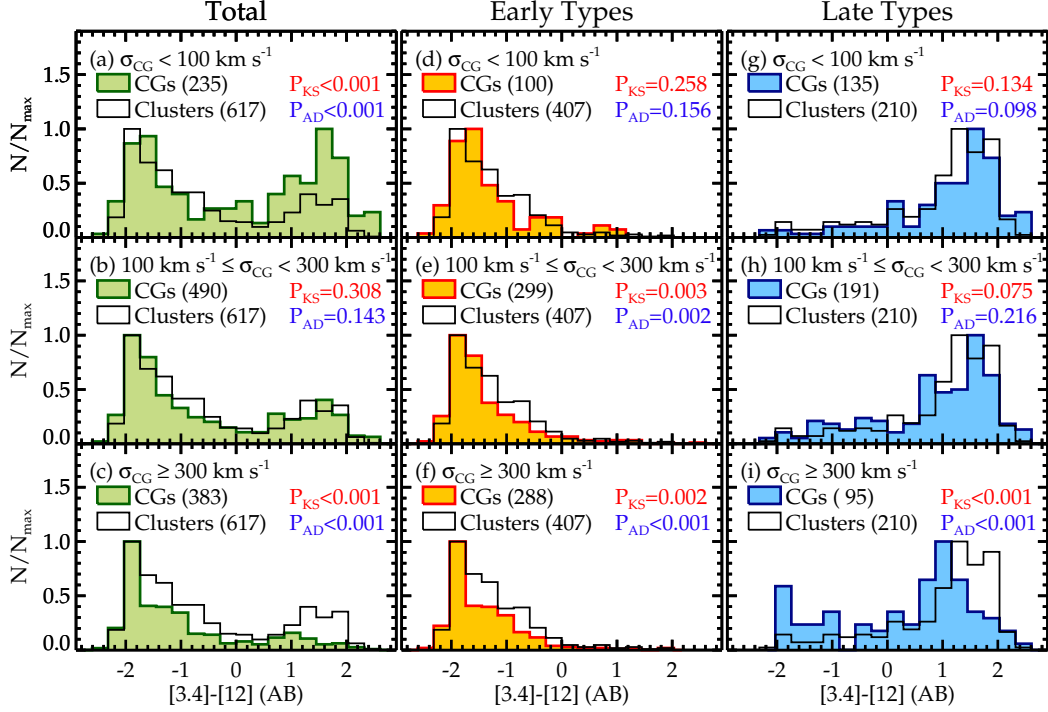
Figure 3.9 Left: MIR color distributions for compact group galaxies (filled histograms) in the (a) $\sigma_{CG} < 100$ km s^{-1}, (b) 100 km s$^{-1} \leq \sigma_{CG} < 300$ km s^{-1}, and (c) $\sigma_{CG} \geq 300$ km s^{-1} compact groups. Open histograms represent cluster galaxies. We plot early-type galaxies in the middle column (d−f) and late-type galaxies in the right column (g−i).

discussion).

Figure 3.9 shows how the MIR colors of compact group galaxies depend on σ_{CG}. We divide compact groups into low (< 100 km s^{-1}), intermediate ($100-300$ km s^{-1}), and high (≥ 300 km s^{-1}) σ_{CG} systems. In the left column, we find that the fraction of MIR red (i.e., $[3.4]-[12] > -0.3$) galaxies decreases as σ_{CG} increases. This is because that the fraction of late-type galaxies is smaller in higher σ_{CG} systems. This trend is similar to the N_{nei}-dependence in Figure 3.6.

The MIR colors of compact group early-type galaxies do not depend on σ_{CG}. The MIR color distribution of early-type galaxies in the $\sigma_{\mathrm{CG}} < 100$ km s^{-1} groups does not differ from that of cluster early-type galaxies. However, the MIR colors of early-type galaxies in the $\sigma_{\mathrm{CG}} \geq 100$ km s^{-1} groups are significantly ($> 3\sigma$) different (bluer) from those of cluster early-type galaxies.

The MIR colors of late-type galaxies are bluer in the $\sigma_{\mathrm{CG}} \geq 300$ km s^{-1} groups than in the $\sigma_{\mathrm{CG}} < 300$ km s^{-1} groups. The P_{KS} and P_{AD} confirm the color difference with a significance $\gtrsim 3\sigma$ level. Furthermore, the MIR colors of late-type galaxies in the $\sigma_{\mathrm{CG}} \geq 300$ km s^{-1} groups are significantly ($> 4\sigma$) bluer than those of cluster late-type galaxies.

In Figures 3.6−3.9, we find that the MIR colors of compact group early-type galaxies do not depend much on the three environmental parameters, and that compact group late-type galaxies depend on f_{E} and σ_{CG}, but not on N_{nei}. In $f_{\mathrm{E}} > 0$ or $\sigma_{\mathrm{CG}} \geq 300$ km s^{-1} compact groups, late-type member galaxies show bluer MIR color distributions. Bitsakis et al. (2011) showed that σ_{CG} tend to be larger in dynamically old ($f_{\mathrm{E}} > 0.25$) compact groups than in dynamically young groups. However, f_{E} and σ_{CG} for our compact groups do not have a significant correlation (Figure 3.5). Spearman's rank correlation coefficient for f_{E} and σ_{CG} is 0.28 and the probability of obtaining the correlation by chance is $\ll 0.001\%$, suggesting that the correlation between the two parameters is weak.

To examine which environmental parameter among f_{E}, σ_{CG}, and N_{nei} most affects the MIR colors of galaxies, we first consider f_{E} and σ_{CG} simultaneously in Figure 3.10. In the left panels we compare MIR colors of late-type galaxies in the $f_{\mathrm{E}} = 0$ compact groups with those of late-type galaxies in the $f_{\mathrm{E}} > 0$ groups in three σ_{CG} bins. We find that MIR colors of late-type galaxies in the $f_{\mathrm{E}} > 0$ groups are bluer than those of late-type galaxies in the $f_{\mathrm{E}} = 0$ groups in all three σ_{CG} bins. The KS and AD k-sample tests reject the null hypothesis at a $\gtrsim 2.3\sigma$ level in the
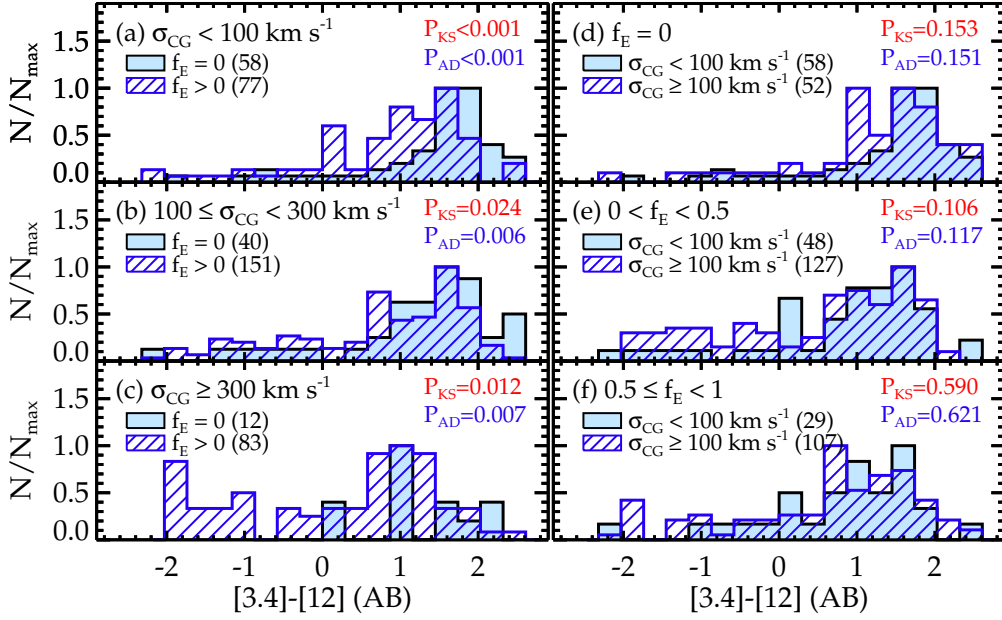
Figure 3.10 Left: MIR color distributions for late-type galaxies in the (a) $\sigma_{CG} < 100$ km s^{-1}, (b) $100 \leq \sigma_{CG} < 300$ km s^{-1}, and (c) $\sigma_{CG} \geq 300$ km s^{-1} compact groups. Filled and hatched histograms represent late-type galaxies in the $f_E = 0$ groups and those in the $f_E > 0$ groups, respectively. Right: The color distributions for late-type galaxies in the (d) $f_E = 0$, (e) $0 < f_E < 0.5$, and (f) $0.5 \leq f_E < 1$ compact groups. Filled and hatched histograms represent late-type galaxies belonging to the $\sigma_{CG} < 100$ km s^{-1} groups and the $\sigma_{CG} \geq 100$ km s^{-1} groups, respectively. We list P_{KS} and P_{AD} for the two histograms in each panel.

three bins. On the other hand, in the right column of Figure 3.10 we compare MIR colors of late-type galaxies in the $\sigma_{\mathrm{CG}} < 100$ km s^{-1} groups with those of late-type galaxies in the $\sigma_{\mathrm{CG}} \geq 100$ km s^{-1} groups in the three f_{E} bins. We find that there is no significant color difference between the two σ_{CG} samples in all three f_{E} bins. These results suggest that the MIR colors of late-type galaxies in compact groups are more sensitive to f_{E} than σ_{CG}.

We conduct a similar analysis to examine whether the f_{E} effects on galaxy colors exist when N_{nei} is fixed. Spearman's rank correlation coefficient for f_{E} and N_{nei} is 0.39, and the probability of obtaining the correlation by chance is $\ll 0.001\%$, suggesting that there is a weak correlation between the two parameters. In the left column of Figure 3.11, we compare MIR colors of late-type galaxies in the $f_{\mathrm{E}} = 0$ groups with those in the $f_{\mathrm{E}} > 0$ groups in three N_{nei} bins. In all three N_{nei} bins, the MIR colors are bluer in the $f_{\mathrm{E}} > 0$ groups than in the $f_{\mathrm{E}} = 0$ groups. The AD k-sample test rejects the null hypothesis at the $\gtrsim 2.5\sigma$ level, and the KS test also rejects the null hypothesis at the $> 2\sigma$ level. On the other hand, the right column shows that there is no significant difference in MIR colors between the late-type galaxy samples in the $N_{\mathrm{nei}} < 6$ groups and those in the $N_{\mathrm{nei}} \geq 6$ groups. Figures 3.10 and 3.11 demonstrate that the MIR colors of late-type galaxies in compact groups change most significantly with f_{E} among the three environmental parameters, suggesting that the f_{E} is the most important parameter in determining the MIR colors of late-type galaxies in compact groups.

3.4 Discussion

3.4.1 Fast Galaxy Evolution in Compact Groups

In Section 3.3, we find that the MIR colors of early-type galaxies are bluer in compact groups than in clusters and the field. This trend also persists when we use several
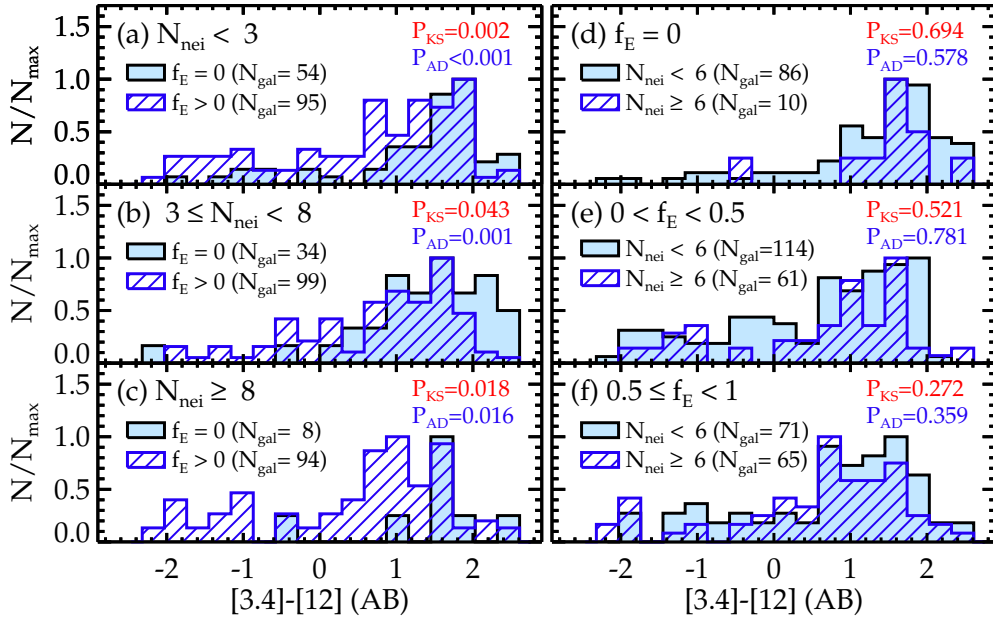
Figure 3.11 Left: MIR color distributions for late-type galaxies in the (a) $N_{nei} < 3$, (b) $3 \leq N_{nei} < 8$, and (c) $N_{nei} \geq 8$ compact groups. Filled and hatched histograms represent late-type galaxies in the $f_E = 0$ groups and those in the $f_E > 0$ groups, respectively. Right: The distributions of late-type galaxies in the (d) $f_E = 0$, (e) $0 < f_E < 0.5$, and $0.5 \leq f_E < 1$ compact groups. Filled and hatched histograms represent late-type galaxies in the $N_{nei} < 6$ compact groups and those in the $N_{nei} \geq 6$ compact groups, respectively.

subsamples with $N_{\rm nei}$, $f_{\rm E}$, and $\sigma_{\rm CG}$. We also find that the late-type galaxies in the $f_{\rm E} > 0$ (or $\sigma_{\rm CG} \geq 300$ km s^{-1}) compact groups have MIR colors bluer than those of cluster late-type galaxies. These results imply that stellar populations in early-type galaxies are on average older in compact groups than in clusters, and that star formation activity of late-type galaxies is suppressed more efficiently in $f_{\rm E} > 0$ compact groups than in clusters. These results suggest that galaxy evolution in compact groups is faster than in the central ($R < 0.5R_{200}$) regions of clusters.

So far, several studies have concluded that galaxy evolution is faster in compact groups than in the field through various analyses (e.g., Proctor et al. 2004; de la Rosa et al. 2007; Bitsakis et al. 2010, 2011, 2016; Tzanavaris et al. 2010; Walker et al. 2010, 2012; Coenda et al. 2012, 2015; Lenkić et al. 2016). Proctor et al. (2004) and Mendes de Oliveira et al. (2005) found that the properties of compact groups (i.e., stellar ages and the early-type galaxy fraction) are more similar to those of cluster galaxies than those of field galaxies. However, previous studies have not found evidence that galaxy evolution is faster in compact groups than in galaxy clusters.

Johnson et al. (2007) and Walker et al. (2010, 2012) showed that compact group galaxies show a strong bimodal *Spitzer* IRAC $3.6 - 8$ μm color distribution with an evident gap at green colors. This gap is not found in comparison samples of isolated galaxies, galaxy pairs, and the center of the Coma cluster. However, they found that the Coma infall region (i.e., $0.4 - 0.6R_{200}$, Jenkins et al. 2007) shows the color distribution statistically similar to that of compact group galaxies. They interpreted these results as that the infall region and compact groups have a similarity in environment. To examine their results with our data, we select 495 galaxies at $R < 0.4R_{200}$ (representing the central regions of clusters) and 231 galaxies at $0.4R_{200} \leq R < 0.6R_{200}$ (representing the infall regions) from the cluster galaxy sample. We compare the MIR color distributions for the two cluster galaxy subsamples with that for the compact group galaxy sample in Figure 3.12(a). The color
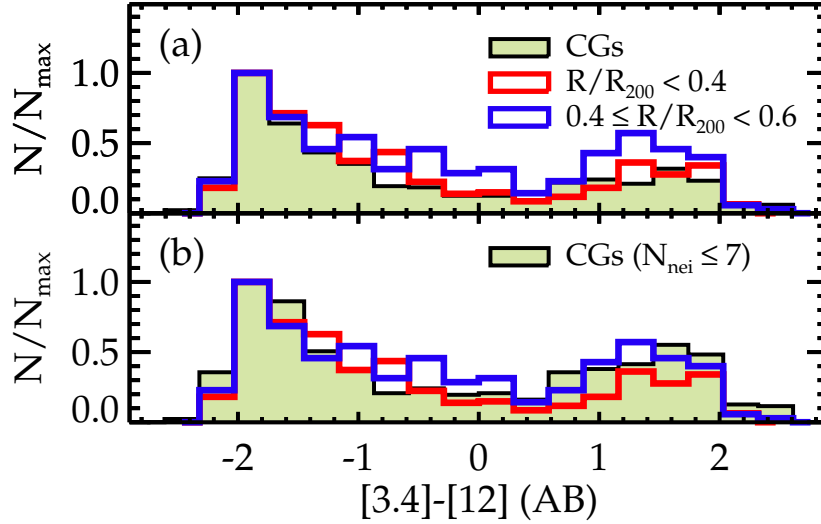
Figure 3.12 (a) Comparison of MIR color distributions for compact group galaxies (filled histograms) and cluster galaxies (open histograms). Red and blue histograms are for cluster galaxies with $R/R_{200} < 0.4$ and $0.4 \leq R/R_{200} < 0.4$, respectively. (b) We only plot galaxies belonging to $N_{\mathrm{nei}} \leq 7$ compact groups.

distribution for the compact group galaxy sample is more similar to that for the $R < 0.4R_{200}$ cluster galaxy sample ($P_{\mathrm{KS}} = 0.211$ and $P_{\mathrm{AD}} = 0.102$) than for the $0.4R_{200} \leq R < 0.6R_{200}$ cluster galaxy sample ($P_{\mathrm{KS}} = 0.001$ and $P_{\mathrm{AD}} = 0.002$). This result is not consistent with the results of Walker et al.

Walker et al. (2010) used a sample of 16 Hickson compact groups. Walker et al. (2012) used not only 21 Hickson compact groups but also 16 Redshift Survey Compact Groups (RSCG, Barton et al. 1996) identified using the friends-of-friends algorithm. However, only 5 of the 16 RSCGs are embedded in larger structures such as clusters. Thus, Walker et al.'s samples could also be dominated by compact groups located in less dense regions. We select 571 galaxies in the $N_{\mathrm{nei}} \leq 7$ compact groups to mimic the Walker et al.'s sample, and show their MIR color distribution in Figure 3.12(b). The MIR color distribution of the 571 galaxies in the $N_{\mathrm{nei}} \leq$

7 compact groups is not statistically different with the color distribution for the $0.4R_{200} \leq R < 0.6R_{200}$ cluster galaxy sample ($P_{KS} = 0.444$ and $P_{AD} = 0.137$), which is consistent with the results of Walker et al. Therefore, the different results between this study and Walker et al. are probably from the use of different methods in identifying compact groups with and without using isolation criterion (see also Figure 10 of Sohn et al. 2016).

One of the reasons why galaxy evolution is faster in compact groups than in clusters is likely because galaxy interactions are more frequent in compact groups than in clusters. The median velocity dispersion for our compact groups is $\sim$200 km s^{-1}, which is much smaller than the median value for galaxy clusters, $\sim$800 km s^{-1} (Rines et al. 2013). Furthermore, the mean size of compact groups is 30.7$\pm$0.4 kpc, which is much smaller than the typical virial radius of galaxy clusters, $\sim$1$-$1.5 Mpc (Park & Hwang 2009; Rines et al. 2013). These characteristics make the interactions have a more significant effect in compact groups than in clusters.

In Figure 3.13, we compare the 3.4 μm absolute magnitude ($M_{3.4}$) distribution of early- and late-type galaxies in compact groups, clusters, and the field. Hwang et al. (2012b) showed that $M_{3.4}$ can be used as a proxy for stellar masses (M_{star}) of galaxies. We confirm the correlation between the $M_{3.4}$ and M_{star} using the compact group galaxies[8]. The stellar masses in this study are based on $H_0 = 70$ km s^{-1} Mpc^{-1}, and are calculated using the LePHARE[9] spectral energy distribution fitting code (Arnouts et al. 1999; Ilbert et al. 2006) with the SDSS *ugriz* photometric data (see Section 2 of Sohn et al. 2016 for details). Table 3.2 lists M_{star} and $M_{3.4}$ of compact group galaxies.

We find that among compact group early-type galaxies, the fraction of massive populations with $M_{3.4} < -24.5$ ($M_{star} \gtrsim 10^{11} M_{sun}$) is 34.9% $\pm$ 1.8%, which is larger than the 24.6% $\pm$ 2.1% for the cluster early-type galaxy sample and the 21.8% $\pm$

---

[8]$\log(M_{star}/M_{sun}) = (-0.48 \pm 0.01) \times M_{3.4} - (0.76 \pm 0.20)$ with rms= 0.27.

[9]http://www.cfht.hawaii.edu/$\sim$arnouts/LEPHARE/lephare.html
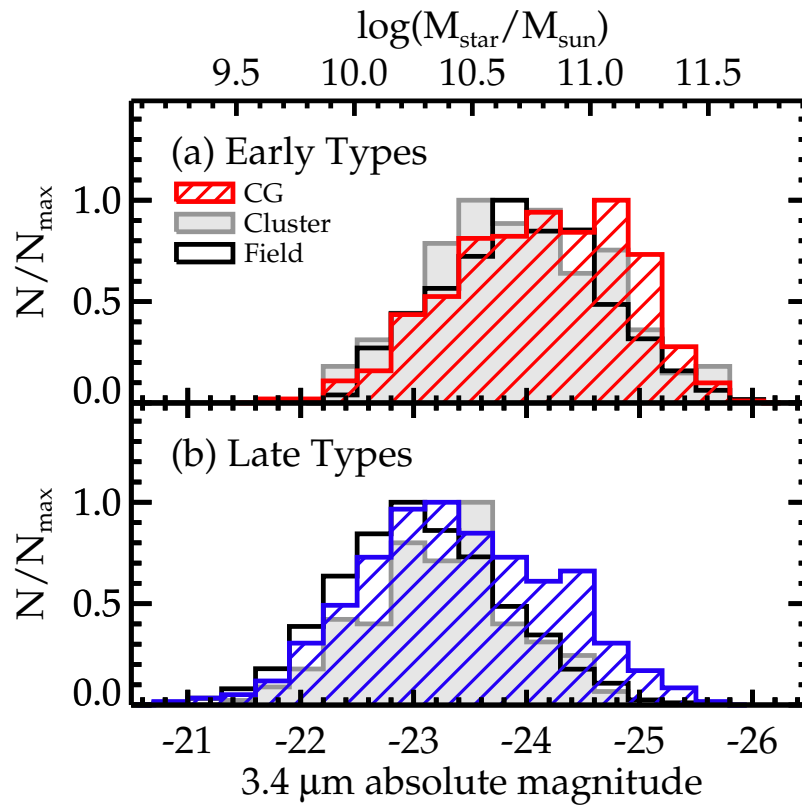
Figure 3.13 Comparison of 3.4 μm absolute magnitude distributions between compact group (hatched histograms) and cluster galaxies (filled histograms). The top panel is for early-type galaxies, while the bottom panel is for late-type galaxies.

1.3% for field early-type galaxy sample. Similarly, among compact group late-type galaxies, the fraction of massive populations with $M_{3.4} < -23.5$ ($M_{\text{star}} \gtrsim 10^{10.5} M_{\text{sun}}$) is 44.4%±2.5%, which is larger than the 32.9%±3.2% for the cluster late-type galaxy sample and the $27.0\% \pm 0.8\%$ for the field late-type galaxy sample. This result suggests that compact groups are an ideal environment for efficient mass build-up of galaxies.

3.4.2 Relation between Compact Group Member Galaxies and Neighboring Galaxies

In Section 3.3.3, as shown in Figure 3.6, we find that compact groups have larger f_{E} and bluer MIR colors as their surrounding environments are denser (larger N_{nei}). To further investigate the effects of the surrounding environments on the physical properties of compact group member galaxies, we compare the properties of neighboring galaxies around each compact group with those of the compact group member galaxies. We calculate f_{E}, mean $u - r$ ($\overline{u - r}$), and mean $[3.4] - [12]$ ($\overline{[3.4] - [12]}$) for neighboring galaxies in the comoving cylinder of each compact group. Figure 3.14 shows f_{E}, $\overline{u - r}$, and $\overline{[3.4] - [12]}$ for neighboring galaxies as a function of N_{nei}. Triangles indicate the mean values of the three parameters in N_{nei} bins. As N_{nei} increases, neighboring galaxies have larger f_{E}, redder optical colors, and bluer MIR colors. For comparison, we compute f_{E}, $\overline{u - r}$, and $\overline{[3.4] - [12]}$ for member galaxies of each compact group. Squares represent the mean values for the three parameters of compact group member galaxies.

We find that the two mean curves show a similar pattern in all three panels. The N_{nei}-dependence of f_{E}, $\overline{u - r}$, and $\overline{[3.4] - [12]}$ for neighboring galaxies is consistent with the morphology-density or the SFR-density relation (e.g., Dressler 1980; Lewis et al. 2002; Park & Hwang 2009). However, it is interesting that the similar trends are also seen for compact group member galaxies. Since compact groups are very small
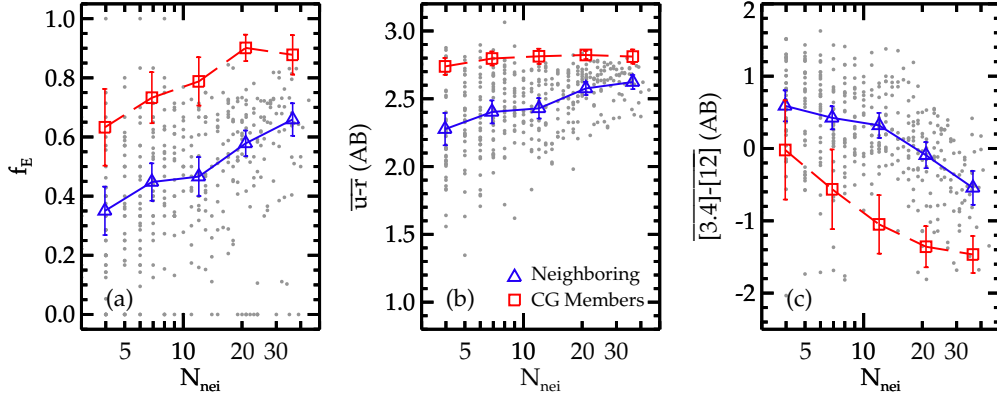
Figure 3.14 N_{nei} dependence of (a) f_{E}, (b) $\overline{u-r}$, and (c) $\overline{[3.4]-[12]}$ for neighboring galaxies within the comoving cylinder around the compact groups, and their mean values (triangles) in N_{nei} bins. For comparison, we also plot the mean values of the three parameters for compact group member galaxies in N_{nei} bins (squares). Error bars represent 3σ deviation in a given N_{nei} bin.

in size (the mean size is 30.7 ± 0.4 kpc), their internal galaxy number densities are much higher than the surrounding densities. The mean internal density of compact groups, measured by the number of members divided by the sizes of the groups, is 1034 ± 18 Mpc^{-2}, which is much higher than the mean surrounding density, 2.54 ± 0.10 Mpc^{-2}, from N_{nei}. Moreover, the internal galaxy number densities of compact groups do not depend on the surrounding galaxy number densities. Thus, the N_{nei}-dependence of the properties of compact group member galaxies can not be explained by the morphology-density or SFR-density relations alone.

The similar N_{nei}-dependence for compact group member galaxies and their neighboring galaxies suggests that the properties of compact group galaxies are related to those of their neighboring galaxies. If the physical properties of compact group galaxies are independent of their neighboring galaxies, the two mean curves would show different behaviors. A plausible scenario would be that the neighboring galaxies

are sources of member galaxies in compact groups. This supports the idea of Diaferio et al. (1994) that compact groups replenish their members from surrounding environments, so that they do not disappear by mergers within a few Gyrs. Previous studies have supported this replenishment model by showing that many ($> 50\%$) compact groups are associated with larger-scale galaxy structures that may supply new members of compact groups. On the other hand, our finding is more direct observational evidence that the replenishment occurs regardless of the surrounding density of compact groups.

An important point is that compact groups are not simply aggregates of captured neighboring galaxies. Figure 3.14 shows that the two mean curves do not overlap, but differ systematically. This result suggests that there are additional environmental effects playing a critical role in morphology transformation and star formation quenching for compact group galaxies, which probably results from frequent interactions among member galaxies. This result also suggests that compact groups are the most suitable environment for the pre-processing (Zabludoff & Mulchaey 1998).

3.4.3 Hydrodynamic Interactions in Compact Groups

We find that the MIR colors of late-type galaxies are bluer in the $f_{\rm E} > 0$ compact groups than in the $f_{\rm E} = 0$ compact groups (Figure 3.8). This $f_{\rm E}$ dependence is still found when $N_{\rm nei}$ or $\sigma_{\rm CG}$ is fixed (see Figures 3.10 and 3.11), indicating that among the three environmental parameters, $f_{\rm E}$ could be the most important parameter in determining the MIR colors of late-type member galaxies. The $[3.4] - [12]$ colors of late-type galaxies are well correlated with specific SFRs (Donoso et al. 2012; Hwang et al. 2012b). Thus, this finding suggests that star formation activity of late-type galaxies is suppressed more efficiently in the $f_{\rm E} > 0$ compact groups than in the $f_{\rm E} = 0$ compact groups. Moreover, the suppression of star formation activity is stronger in the $f_{\rm E} > 0$ compact groups than in the cluster central ($R < 0.5R_{200}$)

regions (Figure 3.8).

Bitsakis et al. (2010, 2011) showed that late-type galaxies in the $f_{\mathrm{E}} > 0.25$ compact groups tend to have smaller specific SFRs than those in the $f_{\mathrm{E}} < 0.25$ compact groups. Their result seems similar to our result. To verify their result with our sample, we divide our compact group sample into the $f_{\mathrm{E}} = 0$, $0 < f_{\mathrm{E}} \leq 0.25$, and $f_{\mathrm{E}} > 0.25$ compact groups. The large values (> 0.85) of P_{KS} and P_{AD} cannot reject the null hypothesis for two MIR color distributions for late-type galaxies in the $0 < f_{\mathrm{E}} \leq 0.25$ compact groups and for late-type galaxies in the $f_{\mathrm{E}} > 0.25$ compact groups. However, the $P_{\mathrm{KS}} = 0.056$ and $P_{\mathrm{AD}} = 0.008$ reject the null hypothesis for two MIR color distributions for late-type galaxies in the $f_{\mathrm{E}} = 0$ compact groups and for late-type galaxies in the $0 < f_{\mathrm{E}} \leq 0.25$ compact groups at a significance $\gtrsim 2\sigma$. These suggest that the $f_{\mathrm{E}} = 0$ and $0 < f_{\mathrm{E}} \leq 0.25$ compact groups in our sample have statistically different MIR color distributions for their late-type member galaxies, which supports again our finding that MIR colors of late-type galaxies are bluer in the $f_{\mathrm{E}} > 0$ compact groups than in the $f_{\mathrm{E}} = 0$ compact groups. The different f_{E} criterion between this study and Bitsakis et al. probably results from different compact group samples.

An important point here is that the star formation activity of late-type galaxies in compact groups is suppressed when the groups contain early-type members. This suppression of star formation activity cannot be explained by gravitational interactions among member galaxies alone. Park et al. (2008) and Park & Choi (2009) found that galaxy properties strongly depend on the distance and morphology of the nearest neighbor galaxy, using spectroscopic samples drawn from the SDSS data. They showed that when a galaxy is located within the virial radius of its nearest neighbor galaxy, the galaxy tends to have a morphological type similar to that of the neighbor galaxy. However, this phenomenon does not manifest if the distance to the neighbor is greater than the virial radius of the neighbor. They suggested

that the phenomenon is due to hydrodynamic interactions, and that the effects of hydrodynamic interactions are significant to change the morphology and star formation activity of galaxies when the galaxies are located within the virial radii of their neighbor galaxies. The sizes of compact groups (the mean value is 30.7 kpc) are significantly smaller than virial radii of member galaxies (i.e., 430 kpc and 340 kpc for early- and late-type galaxies with $M_r = -20.77$, Park & Hwang 2009). This implies that compact group member galaxies are already located within the virial radius of each other, and that they interact hydrodynamically each other.

Park & Hwang (2009) focused on the case of galaxies located within the virial radii of massive galaxy clusters, and found that even in cluster environments the hydrodynamic interactions with early-type neighbor galaxies are the main drivers of star formation quenching of late-type galaxies. They also found that the effects of the cluster hot gas on the star formation quenching of galaxies at $R > 0.1R_{200}$ is insignificant compared to the effects of hydrodynamic interactions with neighbor galaxies. Unlike cluster environments, hot gas of compact groups is not in a hydrostatic equilibrium state, and it is likely to be associated with the individual galaxies or brightest galaxies (Desjardins et al. 2013, 2014), suggesting that hydrodynamic effects from hot gas are insignificant in compact groups. Therefore, we conclude that the suppressed star formation activity of late-type galaxies in the $f_{\rm E} > 0$ compact groups likely results from hydrodynamic interactions with early-type member galaxies.

3.5   Summary and Conclusions

We study the MIR properties of galaxies in compact groups and their environmental dependence using a volume-limited sample of 670 compact groups and their 2175 member galaxies with $M_r < -19.77$ and $0.01 < z < 0.0741$, drawn from the catalog of Sohn et al. (2016). This catalog was derived from nearly complete redshift survey

data, and was constructed by applying a friends-of-friends method without applying Hickson's isolation criterion, which make the catalog include nearby compact groups and embedded compact groups in high-density regions that were often excluded from previous catalogs. Using this unbiased compact group sample, we perform a study comparing the physical properties of galaxies in compact groups with those of galaxies in other environments such as galaxy clusters and the field. We use three environmental parameters including N_{nei}, f_{E}, and σ_{CG} to represent the internal and external environment of the compact groups. Our key findings of this study are summarized as follows.

1. The MIR colors of compact group early-type galaxies are on average bluer than those of cluster ($R < 0.5R_{200}$) early-type galaxies regardless of N_{nei}, f_{E}, and σ. This suggests that early-type galaxies in compact groups are on average older than those of cluster galaxies.

2. The MIR colors of the late-type galaxies in the $f_{\mathrm{E}} > 0$ compact groups tend to be bluer than those of cluster late-type galaxies. These suggests that the star formation activity of late-type galaxies is suppressed more efficiently in $f_{\mathrm{E}} > 0$ compact groups than in clusters.

3. As N_{nei} increases, compact groups have larger f_{E}, redder optical colors, and bluer MIR colors. These trends are also seen for neighboring galaxies around compact groups. Considering the extremely high galaxy number densities in compact group environments, this similar N_{nei}-dependence for compact group member galaxies and their neighboring galaxies is not well explained by the morphology- and SFR-density relations. This result can be explained by the scenario that neighboring galaxies are sources of member galaxies in compact groups, supporting the replenishment model suggested by Diaferio et al. (1994).

4. At a given N_{nei}, compact group members always have on average larger f_{E}

and bluer MIR colors than neighboring galaxies. This suggests that compact groups are not simply aggregates of captured neighboring galaxies, and that compact group environments play a critical role in accelerating morphology transformation and star formation quenching for the member galaxies.

5. In the $f_{\rm E} = 0$ compact groups, the MIR colors of late-type galaxies are on average redder than those of cluster late-type galaxies. However, in the $f_{\rm E} > 0$ compact groups, the MIR colors of late-type galaxies are on average bluer than those in cluster late-type galaxies. This indicates that star formation quenching occurs more effectively in compact groups than in clusters when compact groups have early-type members. This suppressed star formation activity of late-type galaxies likely results from hydrodynamic interactions with early-type member galaxies.

Our results suggest that galaxy evolution is faster in compact groups than in other environments, and that compact groups are likely to be the best place for the pre-processing (Zabludoff & Mulchaey 1998).

Chapter 4

A GMOS-IFU Spectroscopy of E+A Galaxies: On the Spatial Distribution of Young Stellar Population

4.1 Introduction

Post-starburst, or "E+A" galaxies are characterized by unusual optical spectra with strong Balmer absorption lines (e.g., Hδ, Hγ, and Hβ) and the lack of emission lines (e.g., [OII] or Hα). Strong Balmer absorption lines indicate the presence of a large population of A stars, while the lack of significant emission lines indicates the lack of current star formation. These spectral features reveal that a substantial burst of star formation abruptly ended within $1 - 1.5$ Gyr (Dressler & Gunn 1983; Couch & Sharples 1987; Leonardi & Rose 1996; Dressler et al. 1999; Poggianti et al. 1999). This mixture of early- and late-type galaxy characteristics indicates that

E+A galaxies are in a transition phase between star-forming galaxies and quiescent galaxies.

The tidal features common to E+A galaxies (Zabludoff et al. 1996; Yang et al. 2004, 2008) suggest that galaxy mergers are responsible for E+A galaxy formation. Numerical simulations have shown that the E+A phase begins during or after the starburst (and/or active galactic nuclei) phase in major mergers (e.g., Hopkins et al. 2008; Snyder et al. 2011). During a gas-rich major merger, tidal torques drive gas inflows to the galactic center, triggering a compact central starburst (e.g., Barnes & Hernquist 1992, 1996; Mihos & Hernquist 1996). As a result of the compact starbursts, the young stellar population (A stars) is expected to be confined within the galactic center, $\lesssim 1$ kiloparsec (kpc) scales (Bekki et al. 2005; Hopkins et al. 2008, 2009). If this prediction is correct, the Balmer absorption lines should be enhanced at the galactic center, from which a steep radial gradient of the Balmer absorption line strength should be observed.

However, observational studies with spatially resolved spectra, obtained using a long-slit or integral field unit (IFU) spectrograph, of E+A galaxies have presented results that are contrary to the prediction from simulations. Through long-slit spectra analysis of twenty E+A galaxies at $z \leq 0.13$, Norton et al. (2001) found that young ($\lesssim 1$ Gyr) stellar populations in the E+A galaxies are more centrally concentrated than old ($\gtrsim$few Gyr) stellar populations, but found that the young populations are not confined to the $\lesssim 1$ kpc regions. Yagi & Goto (2006) also obtained a similar result using long-slit spectroscopy of three E+A galaxies at $z = 0.04 - 0.09$. Pracy et al. (2005) obtained IFU spectroscopy of 12 E+A galaxies in the AC 114 cluster at $z = 0.32$, with the FLAMES multi-IFU system on the VLT. They found that E+A galaxies exhibit either negative, flat, or positive Hδ absorption line (Hδ_{A}) gradient, from which they suggested that more than one physical mechanism could be responsible for the formation of E+A galaxies. Swinbank et al. (2005) used the Gemini

Multi-Object Spectrograph (GMOS)-South IFU to investigate the spatial distribution of A stars in an E+A galaxy SDSS J101345.39+011613.66 at $z = 0.1055$, and found that the $H\gamma_A$ and $H\delta_A$ are widely distributed in the galaxy, suggesting that A stars is not confined to the nuclear regions. Pracy et al. (2009) and Swinbank et al. (2012) increased the number of E+A galaxies ($z = 0.04 - 0.20$) with the GMOS IFU spectroscopy to 11, and found that the $H\delta_A$ is uniformly distributed over the central few kpc regions ($\sim$33% of the galaxy images). Chilingarian et al. (2009) also found a wide spread of A stars in a nearby ($z \simeq 0.07$) E+A galaxy using the VIMOS IFU spectrograph. These results suggest that A stars have formed not only in the nuclear regions but also in the outer regions.

On the other hand, Pracy et al. (2012) selected seven low-redshift ($z < 0.01$) E+A galaxies from the SDSS DR7 to secure a large angular to physical scale that allows the central 1 kpc region to be resolved spatially. They found that six out of the seven E+A galaxies have centrally concentrated and negative Balmer absorption line gradients within the central 1 kpc regions of the galaxies. Furthermore, Pracy et al. (2013) conducted GMOS IFU observations of four nearby E+A galaxies at $z = 0.019 - 0.034$. They also succeeded in resolving the central 1 kpc regions of the galaxies, and obtained similar results. These results agree well with the expectation from numerical simulations, but is inconsistent with the results for higher-z E+A galaxies (e.g., Swinbank et al. 2012). Pracy et al. (2013) argued that the previous studies failed to detect Balmer line gradients within the central 1 kpc regions because the higher ($z \sim 0.1$) redshift E+A galaxies are too far to resolve the central 1 kpc region spatially given ground-based seeing.

For the four E+A galaxies of Pracy et al. (2013), however, the GMOS IFU field-of-view (FOV) covers only a small part ($\simeq 3 \times 4$ kpc^2) of galactic centers. Thus, the seeing effect does not fully explain the results for high-z E+A galaxies that have widely spread E+A features. Furthermore, Pracy et al. (2012)'s sample

consists of faint galaxies an order of magnitude or more below the characteristic galaxy luminosity (L^*) and fundamentally different from the high-z E+A galaxies with $\sim L^*$. We note that the number (4) of nearby $\sim L^*$ E+A galaxies with IFU data is insufficient compared to the number (11) of high-z counterparts.

Thus, additional nearby E+A galaxy sample with IFU data is required to test Pracy et al.'s results and to verify the expectation from numerical simulations. In this paper, we present a study of the spatial distribution of E+A features of nearby five E+A galaxies at $0.03 < z < 0.05$, which is based on the GMOS IFU data from our observations.

Section 4.2 describes the target selection, the observations and data reduction. In Section 4.3, we present the spatial distribution of E+A features of E+A galaxies we observed, and compare the results with Pracy et al. (2013)'s results. We discuss implications of our results in Section 4.4. In Section 4.5, we summarize our main results and present conclusions.

4.2 Observations and Data Reduction

4.2.1 Target Selection

The motivation of this study is that we have conflicting previous results on the spatial distribution of E+A signature obtained by IFU and long-slit observations. Swinbank et al. (2012) and Pracy et al. (2013) presented conflicting results despite using the same GMOS IFU. To test Pracy et al. (2013)'s results, we need to obtain spatially resolved spectra of galactic centers of E+A galaxies, especially at low redshifts. Thus, we selected five E+A galaxies at a redshift range $0.03 < z < 0.05$, similar to Pracy et al. (2013)'s targets, as the targets for our GMOS IFU observations. Table 4.1 shows basic parameters of the five E+A galaxies. These five E+A galaxies were selected from a parent sample of 568 E+A galaxies ($z < 0.15$) drawn from SDSS

Table 4.1.   Target Information

Target	R.A. (h:m:s)	Decl. (d:m:s)	Redshift	M_r^a	$u-r^b$	$[3.4]-[12]$
EA1	08:34:33.71	17:20:46.3	0.047930	$-21.32_{\pm0.02}$	$2.37_{\pm0.05}$	$1.37_{\pm0.04}$
EA2	10:42:21.92	15:21:34.6	0.049137	$-22.45_{\pm0.01}$	$2.55_{\pm0.05}$	$0.01_{\pm0.06}$
EA3	11:11:17.96	11:33:15.8	0.038106	$-21.97_{\pm0.02}$	$2.18_{\pm0.03}$	$-0.19_{\pm0.04}$
EA4	11:19:07.63	58:03:14.3	0.032604	$-21.30_{\pm0.01}$	$2.32_{\pm0.01}$	$-1.49_{\pm0.07}$
EA5	12:39:36.05	12:26:20.0	0.040856	$-21.66_{\pm0.01}$	$2.21_{\pm0.04}$	$-0.98_{\pm0.14}$

Note. — [a] The SDSS $k_{z=0.1}$, and evolution-corrected r-band Petrosian absolute magnitudes.

[b] The extinction- and k-corrected model magnitudes.

DR7 spectroscopic data. The E+A galaxies in the parent sample were selected by following criterion introduced by French et al. (2015): Hα equivalent width (EW) < 3 Å and H$\delta_A - \sigma(\mathrm{H}\delta_A) > 4$ Å, where $\sigma(\mathrm{H}\delta_A)$ is the measurement error of the Lick index of Hδ absorption line (Worthey & Ottaviani 1997).

Figure 4.1(a) shows the r-band absolute magnitudes (M_r) as a function of redshifts for E+A galaxies including our five E+As and those of previous IFU studies. The M_r was computed using the Galactic reddening correction (Schlegel et al. 1998), $K_{z=0.1}$-corrections (Blanton & Roweis 2007), and evolution correction, $E(z) = 1.6(z - 0.1)$ (Tegmark et al. 2004). Pracy et al. (2012)'s E+A galaxies are very close ($z < 0.01$), but have lower luminosities ($M_r > -20$) than the other samples. Our five E+A galaxies have M_r ranging from -21.3 to -22.4, which is comparable to those of Swinbank et al. (2012)'s sample, but on average one magnitude

brighter than Pracy et al. (2013)'s sample.

Figure 4.1(b) display the $u - r$ versus $[3.4] - [12]$ color-color distribution of E+A galaxies. E+A galaxies in the parent sample are mainly found in the optical green valley (e.g., $u - r \simeq 2.3$), which suggests that E+A galaxies mark a transition from blue cloud to red sequence. However, the E+A galaxies in the parent sample have a wide $[3.4] - [12]$ range, which implies that those galaxies have various dust contents. Thus, the five E+A galaxies in our sample were chosen to have various $[3.4] - [12]$ colors.

Except the brightest galaxy (EA2), the four E+A galaxies in our sample have CO data obtained from a CO survey of French et al. (2015) with the IRAM 30m and SMT 10m telescopes. Among the four E+A galaxies, EA1 is an CO detected ($> 3\sigma$) galaxies, but the other three are not. On the other hand, four E+A galaxies in Pracy et al. (2013)'s sample consist of three CO detected galaxies and an undetected one.

4.2.2   Observations

Spectroscopic observations of five E+A galaxies were taken with the GMOS-North IFU in the queue mode under the program ID GN-2015B-Q-15 (PI: Gwang-Ho Lee). The observations were executed for a total five nights, in December 2015 and March 2016, with sub-arcsecond seeing condition of $0''.57 - 0''.89$. We summarize our GMOS observations in Tabe 4.2. All five targets were observed in two-slit mode with $5'' \times 7''$ field-of-view (FOV) with $0.''07 \times 0.''07$ spatial pixels (spaxels). Given the redshift range ($0.03 < z < 0.05$) of the targets, the FOV covers from the nucleus to $2.1 - 3.4$ kpc radii. Using the B600 grating and g-filter configuration, we obtained spectra covering $\lambda \simeq 4000 - 5500$ Å that cover Balmer lines (Hδ, Hγ, and Hβ) and several metal sensitive lines such as Ca4455, C4668, and Fe5015. To increase the signal-to-noise (S/N) ratio, we used 2 pixel binning in spectral direction (a binned pixel= 0.9 Å). The spectral resolution of $\Delta\lambda \simeq 2.8$ Å for spectra we obtained is
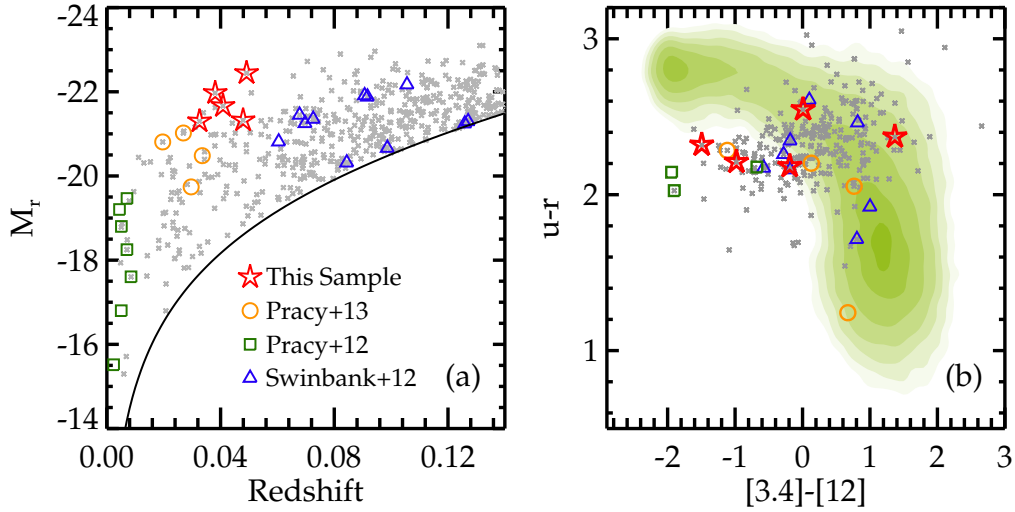
Figure 4.1 (a) Comparison of the r-band absolute magnitude (M_r) and redshift distributions for the E+A galaxy sample in this study (stars) with those for E+A galaxy samples of previous IFU studies such as Pracy et al. (2013, circles), Pracy et al. (2012, squares), and Swinbank et al. (2012, triangles). Small crosses represent the parent sample of 568 E+A galaxies selected from the SDSS DR7 using selection criteria with Hα EW < 3 Å and H$\delta_A - \sigma(H\delta_A) > 4$ Å. The bottom curve indicates the M_r limit as a function of redshifts for the spectroscopic sample $(m_r < 17.77)$. (b) $u-r$ versus $[3.4]-[12]$ color-color distribution for different E+A galaxy samples. Contours represent the number density distribution for SDSS galaxies at $z < 0.05$. In this panel, we only plot galaxies with S/N> 5 at 12μm.

Table 4.2.   Observation Log

Target	Date	μ_r^a [mag arcsec^{-2}]	T_{exp} [min]	Seeing [$''$]	AM
EA1	2015 Oct 24	21.8	96	0.89	1.13
EA2	2016 Feb 11	20.8	180	0.70	1.11
EA3	2016 Mar 5	19.7	110	0.57	1.17
EA4	2016 Mar 6	20.9	180	0.73	1.27
EA5	2016 Mar 7	20.3	180	0.60	1.19

Note. — ^{a} r-band surface brightness at 2.5$''$ radii.

sufficient to measure the Lick line indices that requires a resolution of $\Delta\lambda \simeq 8$ Å.

4.2.3   Data Reduction

Data reduction was performed using the Gemini *IRAF* package and the GMOS example reduction script for the IFU 2 slit mode[1]. We constructed a master bias, and subtracted the master bias from all exposure images. The GCAL flat images were used to identify apertures for fibers. We made a response curve for each fiber with the twilight flat images. The wavelength calibration was established using CuAr arc images. After removing cosmic rays from the science images using the PyCosmic (Husemann et al. 2012), we extracted spectra from the processed science data, and applied flat-fielding, wavelength calibration and sky subtraction to the extracted spectra. The flux calibration was conducted using the sensitivity function obtained

---

[1]http://www.gemini.edu/sciops/data/IRAFdoc/

from the reduction of standard stars. Finally, we made a 3D (x, y, λ) datacube for each target through $0.''1 \times 0.''1$ spaxels sampling.

4.3 Spatial Distribution of the E+A Signatures

4.3.1 2D Image Construction from the 3D Datacube

The first column on the left in Figure 4.2 shows SDSS $g+r+i$ color images ($72'' \times 72''$) of the our five E+A galaxies. The lest is north, and the bottom is east. All of these five E+As have tidally disturbed shapes, which is consistent with the picture that galaxy interactions and mergers are responsible for the E+A phase (Zabludoff et al. 1996; Yang et al. 2004, 2008). Squares superimposed on the SDSS images indicate the GMOS IFU FOV with $5'' \times 7''$. The FOV covered only central regions of the E+As. For the farthest target, EA2, the FOV covers about 4.8×6.7 kpc^2. EA1 overlaps with an foreground galaxy. However, the foreground galaxy is rarely covered in the FOV.

The second column of Figure 4.2 shows the continuum maps. To increase signal-to-noise ratio (S/N), we performed 5×5 spaxel^2 ($0.''5 \times 0.''5$) boxcar smoothing for each spaxel. The continuum level for each spaxel is the 3σ-clipping median value of the combined spectrum with $\lambda = 4200 - 5000$ Å in the rest frame. We overplot a circle with a radius of 1 kpc. For all five E+As, their continuum profiles exhibit a sharply decrease with increasing radius within the 1 kpc region.

To investigate the spatial distribution of A stars within the GMOS FOV, we will construct the Hδ_A maps in the third column of Figure 4.2. To measure the Hδ_A for each spaxel, we used stellar population models of Schiavon (2007) and EZ_Ages code (Graves & Schiavon 2008). We applied stellar velocity dispersion (σ_s) corrections to the Hδ_A measurements. We measured σ_s from 3, 4, and $5''$ annular binned spectra using the pPXF code (Cappellari & Emsellem 2004) with MILES model spectra
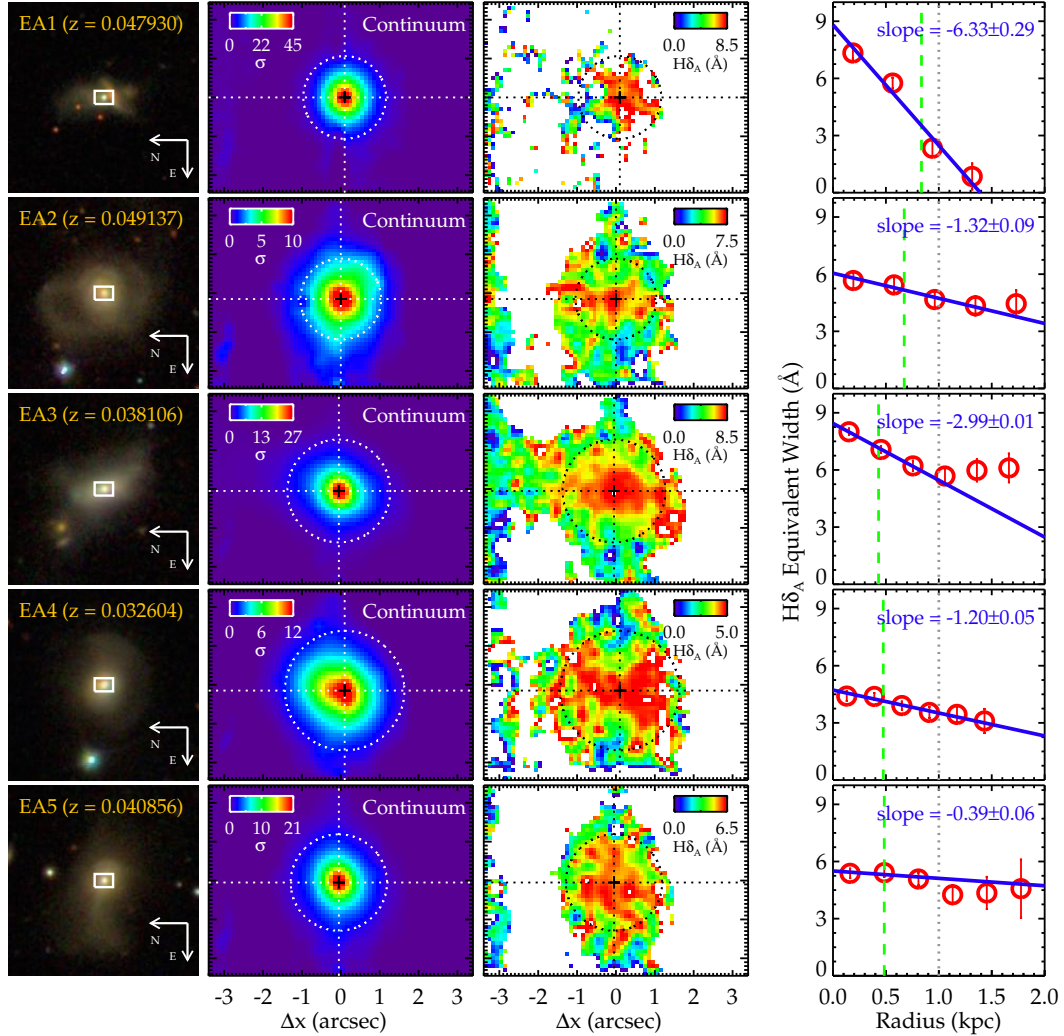
Figure 4.2 The first column: SDSS $g+r+i$ combined images of our targets. Squares indicate the GMOS IFU FOV ($5'' \times 7''$). The second column: Continuum ($4200 - 5000$ Å) map. The third column: Hδ_A map. We only plot the regions with errors of Hδ_A less than 1 Å. To increase signal-to-noise ratio of each spaxel, we used boxcar smoothing of $5{\times}5$ spaxel^2 ($0.''5 \times 0.''5$) in the second and third columns. Crosses represent the galactic center determined in the continuum maps. Circles indicate the 1 kpc radii. The final column shows the Hδ_A equivalent width gradients. Solid lines represent the linear fit for the data within the 1 kpc radii, and the estimated slopes are listed. Vertical dashed lines indicate the seeing sizes, while vertical dotted lines represent the 1 kpc radii.

templates (Vazdekis et al. 2010).

Figure 4.3 shows the σ_s-variation as a function of galactocentric radius. We note that our σ_s measurements based on the GMOS spectra with $3''$ aperture agree well with the SDSS values (stars) obtained with the $3''$ aperture fibers. We performed linear fits using the σ_s derived from the $5''$-binned spectra (circles). This figure also shows that σ_s derived from the $3''$- and $4''$-binned spectra also follow the linear fit well. Using the linear fit for each target, we assigned an expected σ_s to each spaxel depending on the distance of the spaxel from the galaxy center. Finally, the σ_s-corrected Hδ_A for each spaxel can be measured.

While continuum maps show centrally concentration distributions, Hδ_A maps shows complex spatial distributions. In four E+As except EA1, strong Hδ_A ($\gtrsim 5$ Å) is distributed even beyond the 1 kpc radii. We only plot the regions with Hδ_A errors less than 1 Å. At most spaxels outside the 1 kpc radius region, we cannot obtain the Hδ_A with small errors. In the case of EA1, it is difficult to see the Hδ_A spatial distribution even in the galactic center due to low signal.

In order to secure the Hδ_A even at the $R > 1$ kpc region, we extracted central region ($R < 0.''4$) spectra and $0.''4$ annular binned spectra from the IFU data cube. Figure 4.4 shows an example of extracted spectra from the IFU data cube for the EA3. The S/N around the Hβ line ($\lambda = 4000 - 4200$ Å) decreases from 50 to 18 from the top spectrum ($0.'' - 0.''4$) to the bottom spectrum ($2.''0 - 2.''4$).

The fourth column of Figure 4.2 shows the radial profile of the Hδ_A measured using the annular binned spectra. For all five E+As, the Hδ_A tends to decreases with radius. We measured the slope of the Hδ_A gradient for each target using data within $R = 1$ kpc. Depending on the redshifts of the targets, the number of data within $R = 1$ kpc is changed to three or four. The slope of the Hδ_A radial gradient within $R = 1$ kpc is the steepest for the EA1 (-6.33 ± 0.12), while for others it ranges from -0.39 ± 0.02 to -2.99 ± 0.01. We also determined the slopes of the
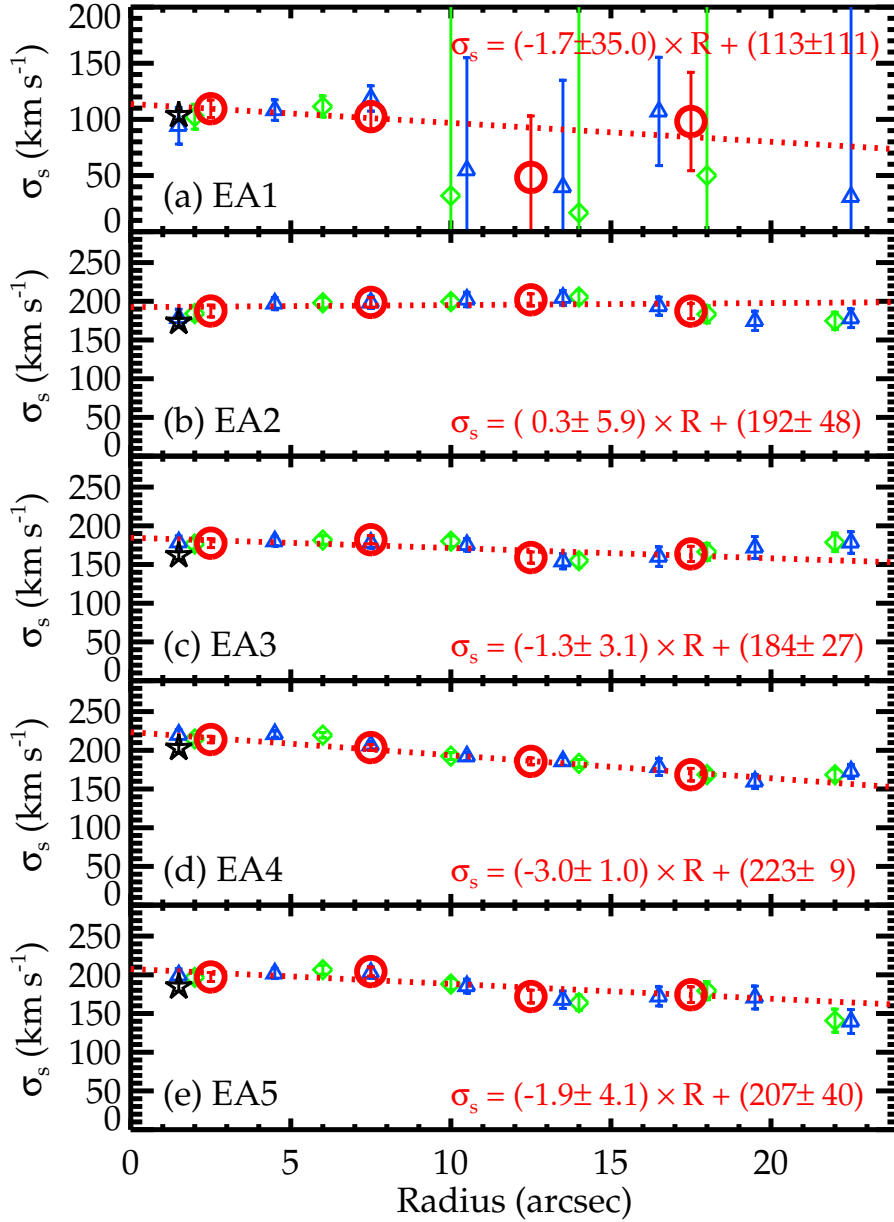
Figure 4.3 Stellar velocity dispersions (σ_s) derived from annular binned spectra as a function of radius. Different symbols represent velocity dispersions derived from spectra with different annular bin sizes (circle: $5''$, diamonds: $4''$, triangles: $3''$). Dotted lines represent the linear fit with the $5''$ annular binned data, and the slopes and intercepts are listed. Stars represent velocity dispersions drawn from the MPA-JHU DR7 value-added galaxy catalog.
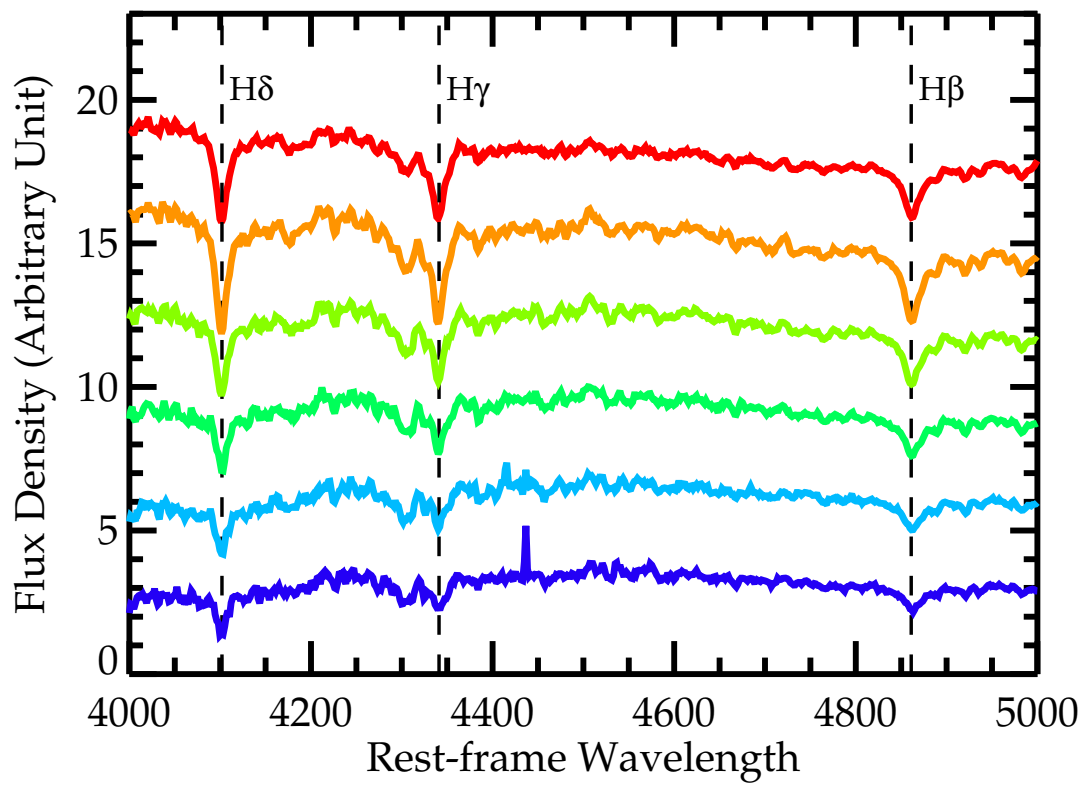
Figure 4.4 Extracted spectra of EA3 with different annular bins: $0.''0 - 0.''4$ (top), $0.''4 - 0.''8$, $0.''8 - 1.''2$, $1.''2 - 1.''6$, $1.''6 - 2.''0$, and $2.''0 - 2.''4$ (bottom).

Table 4.3.   H$\delta_{\rm A}$ Gradient Slope

| Target | 0.″3-Sampling | | 0.″4-Sampling | | 0.″5-Sampling | |
	$N_{\rm data}^a$	Slope	$N_{\rm data}^a$	Slope	$N_{\rm data}^a$	Slope
EA1	4	-6.02 ± 1.47	3	-6.33 ± 0.29	2	-9.05 ± 0.01
EA2	4	-1.05 ± 0.18	3	-1.32 ± 0.09	2	-1.11 ± 0.01
EA3	5	-3.09 ± 0.08	3	-2.99 ± 0.01	3	-2.75 ± 0.08
EA4	5	-1.06 ± 0.04	4	-1.20 ± 0.05	3	-0.93 ± 0.03
EA5	4	-0.41 ± 0.09	3	-0.39 ± 0.06	2	-0.26 ± 0.01

Note. — ^{a} Number of data within $R = 1$ kpc.

H$\delta_{\rm A}$ radial gradients using the H$\delta_{\rm A}$ values taken from 0.″3 and 0.″5 annular binned spectra. Regardless of the bin size for spectra sampling, the EA1 always exhibits the steepest H$\delta_{\rm A}$ gradient slope. These slope measurements are listed in Table 4.3.

4.3.2   Comparison with Pracy et al. (2013)'s E+A Sample

To compare our results with Pracy et al. (2013)'s results, we used another GMOS IFU data taken from GN-2006B-Q-48 observations (PI: Turner). Data reduction and analysis were performed in the same manner we described in Sections 4.2.3 and 4.3.1. Table 4.4 shows basic parameters of the four E+A galaxies in Pracy et al. (2013).

Figure 4.5 shows the H$\delta_{\rm A}$ radial profiles for four E+As of Pracy et al. (2013). This figure shows both our H$\delta_{\rm A}$ measurements (circles) and Pracy et al. (2013)'s measurements (squares). Our H$\delta_{\rm A}$ measurements are based on 0.″4 annular binned

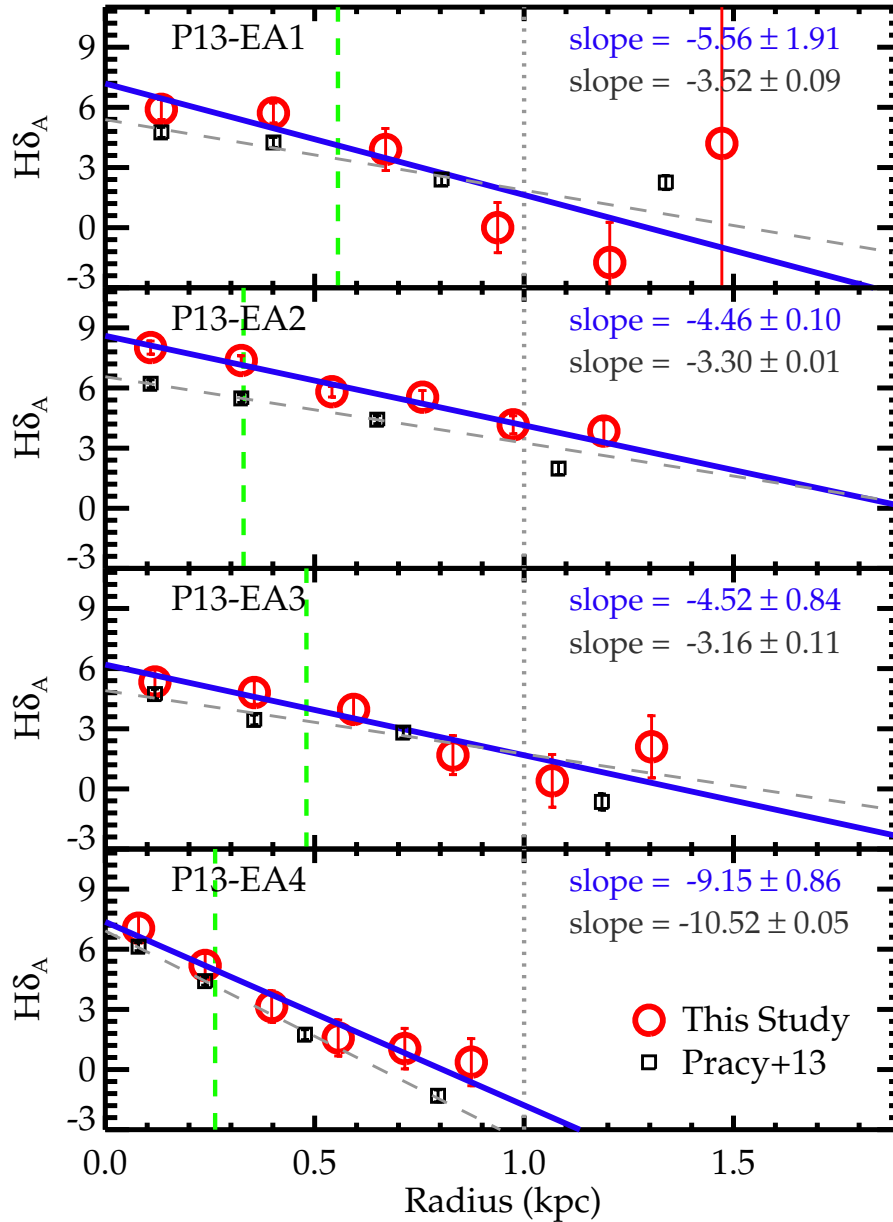Figure 4.5 Hδ_A radial profiles for E+As of Pracy et al. (2013). Circles and squares represent our and Pracy et al. (2013)'s measurements. Solid lines are the linear fit to our measurements, while dashed lines are the linear fit to Pracy et al. (2013)'s measurements. In the linear fit, we used data at $R = 1$ kpc (dotted line). Slopes of the linear fits are listed. Vertical dashed lines indicate seeing sizes.

Table 4.4.   Pracy et al. (2013)'s Target Information

Target	R.A. (h:m:s)	Decl. (d:m:s)	Redshift	SDSS ID
P13-EA1	16:13:30.18	51:03:35.6	0.033566	587729227690475600
P13-EA2	21:14:00.54	00:32:06.4	0.026927	587730847963545655
P13-EA3	17:18:07.86	30:07:44.5	0.029599	587729408621609096
P13-EA4	00:44:59.24	−08:53:23.0	0.019594	587727227842461731

spectra, while Pracy et al. (2013)'s measurements are based on $0.''-0.''4$, $0.''4-0.''8$, $0.''8-1.''6$, and $1.''6-2.''4$ binned spectra. For all four E+As, two measurements agree within 2σ errors. Using data within $R = 1$ kpc, we determined the Hδ_A gradient slopes for our and Pracy et al. (2013)'s measurements, respectively. The Hδ_A gradient slopes determined with our measurements range from -4.46 ± 0.10 to -9.15 ± 0.86, while those determined with Pracy et al. (2013)'s measurements range from -10.52 ± 0.05 to -3.16 ± 0.11. We find that these Hδ_A gradient slopes are steeper than those for EA2−EA5 in our sample.

For Pracy et al. (2013)'s sample, three out of four E+As have Hδ_A close to 0 Å near the 1 kpc radii. Whereas, in our sample, four E+As except EA1 have Hδ_A greater than 3 Å near the 1 kpc radii. Considering the E+A selection criterion H$\delta_A - \sigma($H$\delta_A) > 4$ Å, the H$\delta_A > 3$ Å is not negligible. Between our sample and Pracy et al. (2013)'s sample, there is no significant difference in the Hδ_A in the $0.''0 - 0.''4$ bin. Therefore, the difference in the Hδ_A gradient slopes between two samples is mainly results from the difference in the Hδ_A near the 1 kpc radii.

As shown in Figure 4.2, the Hδ_A radial profiles of EA2-EA5 are nearly flat at $R = 1 - 2$ kpc. This result suggests that these four E+As have E+A signatures

extending beyond the central 1 kpc regions, which is consistent with previous results reported by several studies (Pracy et al. 2005, 2009; Swinbank et al. 2005, 2012; Yagi & Goto 2006; Goto et al. 2008; Chilingarian et al. 2009). These results are in contrast to the steep $H\delta_A$ radial gradients of Pracy et al. (2013)'s sample, as shown in Figure 4.5. However, Pracy et al. (2013) also showed that their $H\delta_A$ gradients become flattened when they smoothed out their data to $z = 0.1$ (see their Figure 3). They were concerned that these degraded profiles could be interpreted as a widespread E+A signature, and argued that the previous studies failed to detect the central concentration of $H\delta_A$ because the E+A samples in the previous studies are too far ($z \simeq 0.1$) to resolve the central kpc regions.

However, this redshift effect does not apply to our E+As because our five E+As are at $z = 0.03 - 0.05$ similar to the targets of Pracy et al. (2013). In other word, the extended $H\delta_A$ distributions found in our E+As cannot be explained by the redshift effect. As shown in Figure 4.2, the seeing sizes for our targets are sub-kpc scales. Thus, the extended $H\delta_A$ distributions are actual characters for the EA2-EA5, which suggests that E+A signatures are not always confined to the central kpc regions.

In Figure 4.6 we inspect the $H\delta_A$ profile for each target as a function of effective radius (R_{eff}). We ran GALFIT version 3.0.5 (Peng et al. 2010b) on the SDSS r-band images for the nine E+As to measure R_{eff}. When radial bins are normalized by R_{eff}, the $H\delta_A$ profiles reach $\sim 0.4 - 0.8$ in unit of R/R_{eff}. For fair comparison, we measure the slopes of the $H\delta_A$ profiles through linear fits using data within $R = 0.4R_{\mathrm{eff}}$. The $H\delta_A$ profiles of the EA1, P13-EA1, and P13-EA4 drops rapidly to ~ 0 Å within $R = 0.4R_{\mathrm{eff}}$. Whereas, the other E+As show slowly declining $H\delta_A$ profiles. The $H\delta_A$ profiles of the EA4, P13-EA2, and P13-EA3 extend beyond $R = 0.4R_{\mathrm{eff}}$. However, those profiles beyond $R = 0.4R_{\mathrm{eff}}$ are all different. This result suggests that the spatial distribution of E+A signatures varies from E+A galaxy to E+A galaxy.
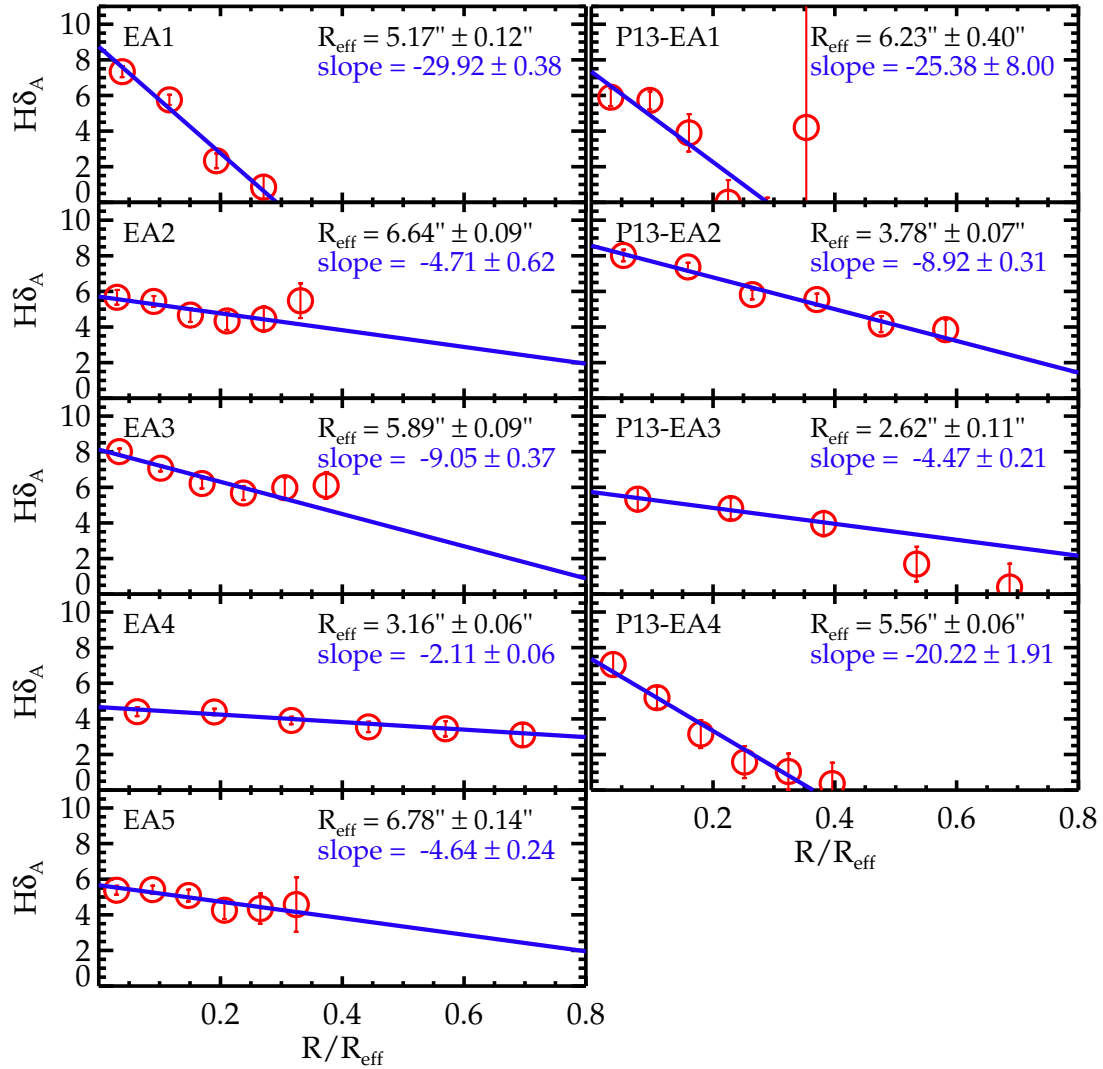
Figure 4.6 The Hδ_A profile as a function of radius normalized by effective radius ($R/R_{\rm eff}$). Solid lines represent a linear fit using data within $R/R_{\rm eff} \leq 0.4$. The $R_{\rm eff}$ and the slopes of the linear fits are listed.
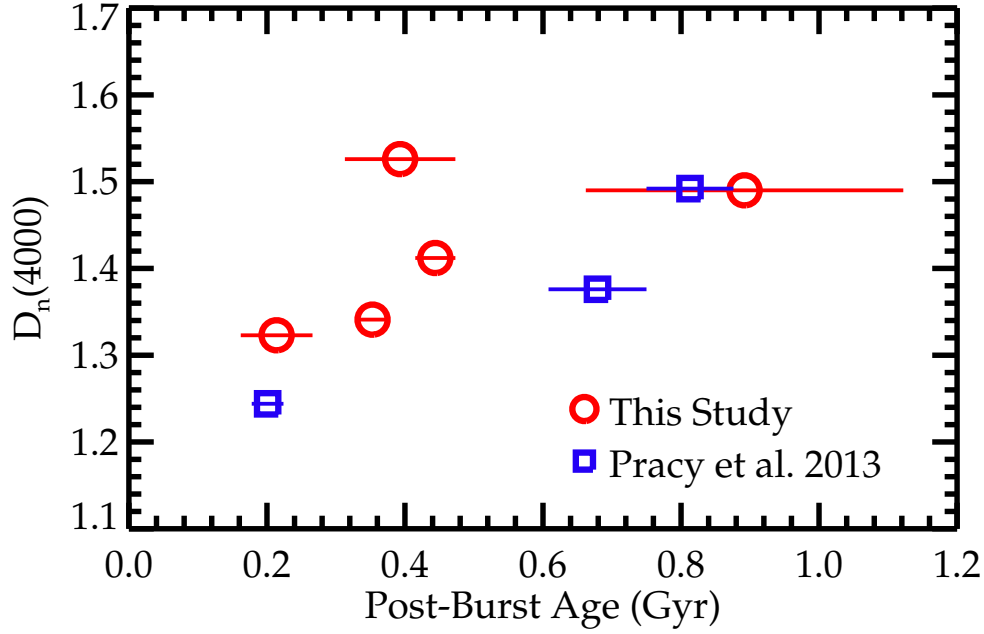
Figure 4.7 D_n4000 vs. post-burst age distribution for E+As in our sample (circles) and Pracy et al. (2013)'s sample.

4.4 Discussion

Recently, French et al. (ApJ-submitted) combined *GALEX*/SDSS photometry, SDSS spectra, and flexible stellar population synthesis models (Conroy et al. 2009; Conroy & Gunn 2010) to fit the SFH of 516 E+As at $0.01 < z < 0.13$. They adopted an extinction law of Calzetti et al. (2000) and Chabrier (2003)'s IMF. They succeeded in breaking the degeneracy between the time elapsed since the end of starburst (post-starburst age), the fraction of stellar mass produced in the burst (burst mass fraction), and the starburst duration. Details for the age-dating technique are described in Section 2 of French et al.

In Figure 4.7 we investigate the relation between D_n4000 and post-burst age for E+As in our and Pracy et al. (2013)'s sample. We adopt D_n4000 values for 8 E+As

except P13-EA1 from the MPA-JHU DR7 value-added galaxy catalog. The D_n4000 is a useful parameter to represent the mean stellar age of galaxies (Balogh et al. 1999). This figure shows that D_n4000 increases as post-burst age increases with a large scatter. The Spearman's rank coefficient for this positive correlation is 0.8 and the probability of obtaining the correlation by chance is less than 1%.

The galaxy merger simulation of Pracy et al. (2005) shows the Hδ_A radial profiles at times 0.2, 0.75, and 1.5 Gyr after the peak of the starburst ($T_{\rm PSB}$, see their Figure 9). AT $T_{\rm PSB} = 0.2$ Gyr, the Hδ_A profile peaks at the galactic center, decreases significantly with radius, and becomes flat at the $R > 2$ kpc region. At $T_{\rm PSB} = 0.75$ Gyr, the peak value of the Hδ_A profile becomes lowered, which makes the Hδ_A gradient slope less steep. At $T_{\rm PSB} = 1.5$ Gyr, Hδ_A has a very small value (nearly zero) in all area because young stars contributing to the Balmer lines are gone, and the host galaxy is no longer E+A galaxy. Pracy et al. (2013) compared their observed Hδ_A profiles of the four E+As with the simulated Hδ_A profiles, and mentioned that the four E+As are post-starburst systems with $T_{\rm PSB} \simeq 0.75$ Gyr.

The post-burst age derived by French et al. means the time elapsed since the starburst ended (since 90% of the starburst stars formed), whereas $T_{\rm PSB}$ is the time after the starburst peak. Considering the burst duration $\tau = 25 - 200$ Myr of E+As, calculated by French et al., the difference between $T_{\rm PSB}$ and the post-burst age used in this study is expected to be less than 100 Myr.

In Figure 4.8(a) we investigate the relation between the post-burst age and the Hδ_A profile slope determined within $R = 1$ kpc. We do not find a clear correlation between the two parameters. In Figure 4.8(c) we use the Hδ_A profile slopes determined within $R = 0.4R_{\rm eff}$ instead. The Spearman's rank coefficient between the slopes and post-burst ages is 0.4, and the probability of obtaining the correlation by chance is 29%. This means that it seems to be a positive correlation between the two parameters, but that it is not significant statistically. This result is inconsistent

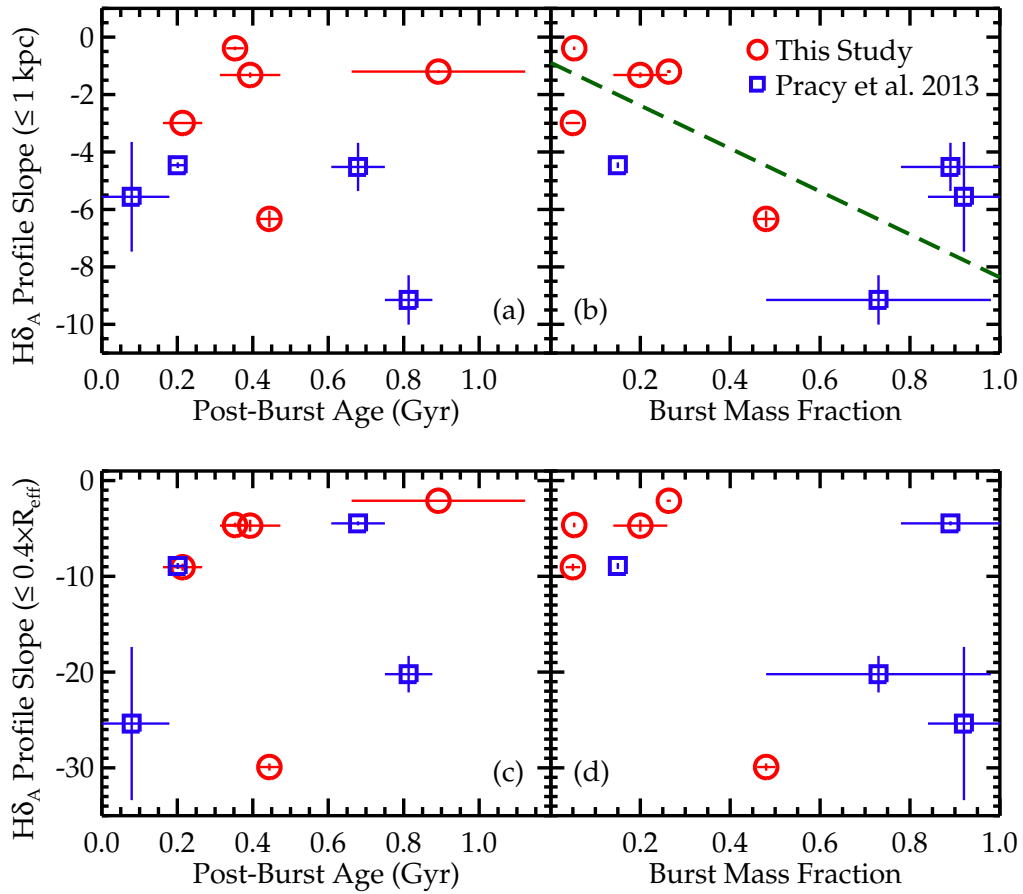Figure 4.8 (a) Hδ_A gradient slope vs. post-burst age and (b) Hδ_A gradient slope vs. burst mass fraction diagram for E+As in our sample (circles) and Pracy et al. (2013)'s sample. The dashed line in panel (b) indicates a linear fit.

with what Pracy et al. (2005)'s simulation expects.

Figure 4.8(b) shows the relation between the burst mass fraction and the Hδ_A profile slope determined within $R = 1$ kpc. The Spearman's rank coefficient between two parameters is -0.67, and the probability of obtaining the correlation by chance is 5%. This suggests that two parameters have a strong negative correlation. However, when we use the Hδ_A slopes determined within $R = 0.4R_{\text{eff}}$, the correlation with the burst mass fractions becomes less clear (the Spearman's rank coefficient is -0.23, and the probability of obtaining the correlation by chance is 55%), as shown in Figure 4.8(d).

We note that the correlation between the Hδ_A profile slopes and burst mass fractions is still tentative. This correlation can arise from just the three most extreme points, which have large errors, at > 0.7 burst mass fractions. In order to verify this tentative correlation, more IFU data of E+A galaxies with intermediate and high burst mass fractions are needed. Even though the correlation is still provisional and subject to confirmation, but if true, it can be understood if E+As with stronger starburst have more centrally-concentrated bursts. It seems like that we are witnessing the "compaction" process in action, occurring in high-z "red nuggets" galaxies which have very centrally concentrated young stellar populations (Barro et al. 2016).

To verify this tentative correlation between the Hδ_A profile slopes and burst mass fractions, we tried to observe two nearby E+A galaxies with high burst mass fractions of $\sim$0.6-0.8 using Gemini-South GMOS/IFU spectroscopy. Unfortunately, all allocated 9.2 hours were lost because of bad weather. We again submitted another proposal of GMOS-North IFU observations of four E+As with high ($0.48-1.0$) burst mass fractions and one E+A with a small (0.05) burst mass fraction.

4.5   Summary and Conclusions

we investigate the spatial distribution of stellar populations in nearby five E+A galaxies ($z \simeq 0.04$) using IFU data from GMOS observations. Numerical simulations expect that the E+A signature tends to be localized within the central (< 1 kpc) regions. Indeed, the findings of Pracy et al. (2013) corroborate this prediction. However, several other past studies suggested show that this is not always the case. Our results also show that all five E+A galaxies in our sample show negative Hδ_A gradients, but that the slopes of the Hδ_A gradients are significantly flatter than those reported in Pracy et al. (2013). This result suggests that A stars are not always confined to the central 1 kpc regions. Furthermore, we found a negative correlation between the slope of these Hδ_A gradients and the fractions of stellar mass produced during starburst. This correlation can be understood if E+A galaxies with stronger starbursts have more centrally-concentrated bursts, or can arise from just small statistics. In order to verify this tentative correlation, we will obtain more IFU data of nearby E+As with full range of burst mass fractions.

Chapter 5

Do Bars Trigger AGN Activity?

(This chapter is published in the Astrophysical Journal.)[1]

5.1 Introduction

Galactic bars are believed to play a crucial role in galaxy evolution. By reducing angular momentum, galactic bars can efficiently transport gas from outer disk to the central kiloparsec scale (Lynden-Bell 1979; Sellwood 1981; van Albada & Roberts 1981; Combes & Gerin 1985; Pfenniger & Friedli 1991; Heller & Shlosman 1994; Bournaud & Combes 2002; Athanassoula 2003; Jogee 2006), as demonstrated by a number of numerical simulations (e.g., Roberts et al. 1979; Athanassoula 1992; Friedli & Benz 1993; Maciejewski et al. 2002; Regan & Teuben 2004). The bar-driven gas can cause a mass accumulation within the Inner Lindblad Resonance (ILR), leading to the destruction of bars and the formation of psuedo-bulges (Hasan & Norman 1990; Pfenniger & Norman 1990; Hasan et al. 1993; Norman et al. 1996; Das et al. 2003; Shen & Sellwood 2004; Athanassoula et al. 2005; Bournaud et al. 2005). Numerous observational studies have found the characteristics of the bar-

---

[1]Lee, G.-H., Woo, J.-H., Lee, M. G., et al. 2012b, ApJ, 750, 141

driven gas: i.e., inflow velocities from CO emission (e.g., Quillen et al. 1995; Benedict et al. 1996) and from Hα emission (e.g., Regan et al. 1997), higher Hα luminosities in barred galaxies than in non-barred galaxies (e.g., Ho et al. 1997), and higher molecular gas concentrations in the central kiloparsec region of barred galaxies (e.g., Sakamoto et al. 1999; Sheth et al. 2005).

Because of the high efficiency of gas inflow toward the central region of galaxies, bars are often invoked as a trigger of nuclear star formation. Enhanced nuclear star formation has been found in the central regions of barred spiral galaxies (e.g., Heckman 1980; Hawarden et al. 1986; Devereux 1987; Arsenault 1989; Huang et al. 1996; Ho et al. 1997; Martinet & Friedli 1997; Emsellem et al. 2001; Knapen et al. 2002; Jogee et al. 2005; Hunt et al. 2008). Some statistical studies presented high bar fractions among star-forming galaxies: e.g., 61% in Ho et al. (1997), 82%-85% in Hunt & Malkan (1999), and 95% in Laurikainen et al. (2004).

Bar-driven gas inflow has been also considered as a mechanism for triggering active galactic nucleus (AGN) activity (Combes 2003). For the past three decades, much effort has been devoted to understand the connection between the presence of bars and AGN activity. However, it is not yet clear whether bars transport gas down to the vicinity of supermassive black holes (SMBHs). Several observational studies claimed that the fraction of barred galaxies is higher in AGN-host galaxies than in non-AGN galaxies (Arsenault 1989; Knapen et al. 2000; Laine et al. 2002), while many others found no significant excess of barred galaxies in AGN-host galaxies (Moles et al. 1995; McLeod & Rieke 1995; Mulchaey & Regan 1997; Ho et al. 1997; Laurikainen et al. 2004; Hao et al. 2009).

Shlosman et al. (1989) suggested the "bars within bars" scenario as a mechanism for fueling AGNs. In this model, large-scale stellar bars transport gas into their rotating disks of a few hundred parsec scale. When a critical amount of gas is accumulated, the disks undergo gravitational instability, triggering a gaseous secondary

bar, which enables gas to approach closer to SMBHs (Mulchaey & Regan 1997; Maciejewski & Sparke 1997; Ho et al. 1997). Some studies suggested that nuclear spirals, instead of secondary bars, are responsible for triggering AGNs (Martini & Pogge 1999; Márquez et al. 2000; Martini et al. 2003). In a recent high-resolution smoothed particle hydrodynamics simulation, Hopkins & Quataert (2010) showed that disk instabilities (for $10 - 100$ pc scales) driven by primary bars exhibit various morphologies as well as bar-like shapes. Several observational studies confirmed the presence of secondary bars by detecting nuclear bars embedded in large-scale bars, using the ISAAC/VLT spectroscopic data (Emsellem et al. 2001), the Hubble Space Telescope (HST) images (Malkan et al. 1998; Laine et al. 2002; Carollo et al. 2002; Erwin & Sparke 2002), and the integral field spectrograph SAURON data (Emsellem et al. 2006). It is found, however, that the fraction of secondary bars in AGNs is similar to that in non-AGNs (Martini et al. 2003), implying that secondary bars do not play a critical role in fueling AGNs. Although there have been many attempts, the nature of the AGN-bar connection is still unclear. The presence of secondary bars or nuclear spirals in non-AGN galaxies suggests that bars are not a universal fueling mechanism (Márquez et al. 2000; Laine et al. 2002; Martini et al. 2003).

In this paper, we investigate the connection between the presence of bars and AGN activity using a large sample of galaxies from the SDSS DR7 data. SDSS data have been used by several previous studies in revealing the dependence of the bar fraction either on internal galaxy properties or on environmental properties (Barazza et al. 2008; Aguerri et al. 2009; Li et al. 2009; Nair & Abraham 2010b; Masters et al. 2011; Lee et al. 2012a). However, the AGN-bar connection has not been studied in detail using the SDSS data. Hao et al. (2009) found no excess of bars in AGN-host galaxies using SDSS data. However, the galaxy sample in their study was relatively small and biased to blue galaxies (see Masters et al. 2011; Lee et al. 2012a). Therefore, it is needed to investigate the connection between bars and

AGN activity using a homogeneous and large galaxy sample. Following our detailed study on the relation between the presence of bars and galaxy properties (Lee et al. 2012a), we investigate the AGN-bar connection using a homogeneous sample of late-type galaxies, selected from the SDSS.

This paper is organized as follows. We describe the volume-limited sample and the method for identifying bars and spectral types in Section 5.2. Section 5.3 presents the main results including the dependence of the bar fraction on spectral types, the dependence of the AGN fraction on the presence of bars, and the comparison of Eddington ratio distributions between barred and non-barred AGN-host galaxies. We discuss the implication of primary results in Section 5.4, and present summary and conclusions in Section 5.5.

5.2   Data and Methods

5.2.1   SDSS Galaxy Sample

We use a volume-limited sample of 33,391 galaxies with the r-band absolute magnitude $M_r \leq -19.5 + 5\log h$ mag (hereafter, we drop the $+5\log h$ term in the absolute magnitude) at redshift $0.02 \leq z \leq 0.05489$, from the SDSS DR7. These galaxies are extracted from the KIAS VAGC that is based on the Large Scale Structure (LSS) sample of New York University Value-Added Galaxy Catalog (NYU VAGC; Blanton et al. 2005). The rest-frame absolute magnitudes of individual galaxies are computed in fixed bandpass, shifted to $z = 0.1$, using the Galactic reddening correction of Schlegel et al. (1998) and K-corrections as described by Blanton et al. (2003). The mean evolution correction given by Tegmark et al. (2004), $E(z) = 1.6(z - 0.1)$, is also applied. The spectroscopic parameters (i.e., stellar velocity dispersions and strength of various emission lines) are obtained from NYU VAGC and MPA/JHU DR7 VAGC (Tremonti et al. 2004; Brinchmann et al. 2004). Stellar masses are

also from the MPA/JHU DR7 VAGC, which are based on fits to the SDSS five-band photometry (Kauffmann et al. 2003a). We adopt a flat ΛCDM cosmology with $\Omega_\Lambda = 0.74$ and $\Omega_m = 0.26$ from *Wilkinson Microwave Anisotropy Probe* five-year data (Komatsu et al. 2009).

The detailed description of the morphological classification and the identification of bars of the sample, and the comparison with previous classifications (de Vaucouleurs et al. 1991; Nair & Abraham 2010a) can be found in Section 3 of Lee et al. (2012a). We summarize the sample selection and classification schemes as follows. First, after dividing all galaxies into early- and late-type galaxies using the automated classification method (Park & Choi 2005) and visual inspection, we selected 19,431 late-type galaxies out of 33,391 galaxies (see Table 1 of Lee et al. 2012a). To avoid the internal extinction effects, we selected only galaxies with the minor-to-major axis ratio $b/a > 0.6$, obtaining a sample of 10,674 late-type galaxies. Then, we classified these late-type galaxies into three groups based on the presence (and the length) of bars: 2542 strong-barred (23.8%), 698 weak-barred (6.5%), and 7434 non-barred galaxies. When the size of bars is larger (shorter) than a quarter of the size of their host galaxies, we classified these galaxies as strong-barred (weak-barred) galaxies. As described in Lee et al. (2012a), our classification shows a good agreement with Nair & Abraham (2010a)'s classification.

In this study we classify the sample galaxies into AGNs and non-AGNs using the spectral features. To determine the spectral types and to investigate the dependence of the bar fraction on spectral types, we select galaxies whose spectra show strong emission-lines of Hα, Hβ, [OIII] λ5007, and [NII] λ6584 with signal-to-noise ratio S/N ≥ 3 (Kewley et al. 2006). By excluding 2019 galaxies that do not satisfy the S/N criterion, we make a final the sample of 8655 late-type galaxies for the following analysis.

We perform the aperture correction to the velocity dispersion of the target galax-

ies using the equation suggested by Cappellari et al. (2006),

$$\sigma_{\mathrm{corr}} = \sigma_{\mathrm{fib}} \times (R_{\mathrm{fib}}/R_{\mathrm{eff}})^{(0.066\pm0.035)}, \qquad\qquad (5.1)$$

where σ_{fib} is the velocity dispersion obtained from a fiber with $R_{\mathrm{fib}} = 1''.5$. R_{eff} is an effective radius calculated by $R_{\mathrm{eff}} = r_{\mathrm{deV}} \times (b/a)_{\mathrm{deV}}^{0.5}$ (Bernardi et al. 2003), where r_{deV} and $(b/a)_{\mathrm{deV}}$ are, respectively, scale radius and b/a axis ratio in i-band in the de Vaucouleurs fit. Hereafter, the velocity dispersion means σ_{corr}, and its subscript corr will be omitted.

5.2.2   Classification of Spectral Types

To determine the spectral types, we use the [NII]/Hα versus [OIII]/Hβ diagnostic diagram that is known as Baldwin-Phillips-Terlevish (BPT) diagram (Baldwin et al. 1981; Veilleux & Osterbrock 1987). We categorize the sample galaxies into three spectral types: star-forming, composite, and AGN-host galaxies. As shown in Figure 5.1, Kewley et al. (2001) drew theoretical "maximum starburst lines" (solid lines) to define the upper boundary of star-forming galaxies, and Kauffmann et al. (2003b) added an empirical demarcation line (dashed line) to distinguish pure star-forming galaxies from composite galaxies whose spectra are affected by both star forming nuclei and AGNs.

We perform spectral classification using two criteria of S/N (for Hα, Hβ, [NII], and [OIII] emission lines): S/N $\geq$ 3 and S/N $\geq$ 6. When S/N $\geq$ 3 is adopted, we find that the fractions of star-forming, composite, and AGN-host galaxies are 57.1% (4940 galaxies), 22.8% (1973 galaxies), and 20.1% (1742 galaxies), respectively. On the other hand, in the case of S/N $\geq$ 6, the sample galaxies consist of 60.3% (3600 galaxies) of star-forming, 23.7% (1411 galaxies) of composite, and 16.0% (957 galaxies) of AGN-host galaxies. The result of spectral classification is summarized in Table 5.1. As the threshold of S/N increases from 3 to 6, the fraction of AGN-host
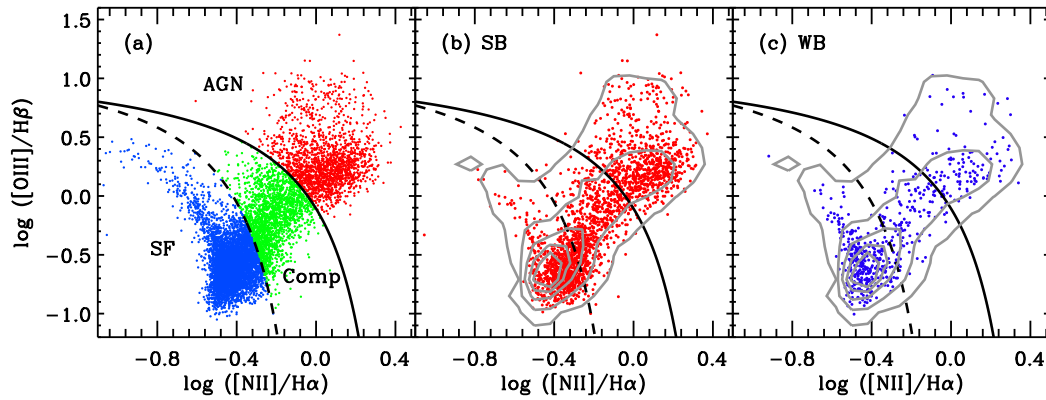
Figure 5.1 (a) Classification of spectral types for 8,655 late-type galaxies in the [NII]/Hα versus [OIII]/Hβ diagram. There are three types of galaxies (red: AGN-host galaxies, green: composite galaxies, and blue: star-forming galaxies) classified by two separate lines, the extreme starburst classification line (Kewley et al. 2001, solid line) and the pure star formation line (Kauffmann et al. 2003b, dashed line). In panels (b) and (c), dots represent strong-barred (SB) and weak-barred (WB) galaxies, respectively. Contours show the distribution for all late-type galaxies shown in panel (a).

Table 5.1.   Spectral Types of the Sample Galaxies

Spectral type	S/N[a]$\geq$ 3		S/N $\geq$ 6	
	Number	Fraction	Number	Fraction
Star-forming	4,940	57.1 %	3,600	60.3 %
Composite	1,973	22.8 %	1,411	23.7 %
AGN-host	1,742	20.1 %	957	16.0 %
Total	8,655	100 %	5,968	100 %

[a]S/N for four emission lines such as Hα, Hβ, [NII] λ6584, and [OIII] λ5007

galaxies decreases 20.1% to 16.0%. This is because a significant fraction of LINERs in the low S/N sample is not included in the high S/N sample, since LINERs tend to dominate the low S/N sample (Cid Fernandes et al. 2010, 2011).

5.3   Results

To investigate the connection between AGN activity and the presence of bars, first, we compare the bar fractions in AGN-host and non-AGN galaxies in Section 5.3.1. Then, we examine the AGN fraction between barred and non-barred galaxies in Section 5.3.2. Finally, using AGN host galaxies, we investigate whether the Eddington ratio distribution is different depending on the presence of bars in Section 5.3.3.

5.3.1 Dependence of Bar Fraction on AGN Activity

Figure 5.1 shows the distributions of strong-barred (panel b) and weak-barred galaxies (panel c) in emission-line ratio diagrams ([NII]/Hα versus [OIII]/Hβ). Strong-barred galaxies are widely distributed over the star-forming, composite, and AGN-host galaxy regions, while the majority of weak-barred galaxies lie in the star-forming galaxy region. Some weak bars are found in the composite and AGN-host galaxy region, but the number of those galaxies is relatively small.

We investigate how the bar fraction varies depending on the spectral types using two S/N criteria as summarized in Table 5.2. In the sample of 8655 galaxies with S/N $\geq$ 3, the fraction of strong-barred galaxies (f_{SB}) is 15.6%$\pm$0.5% in star-forming galaxies, 32.4%$\pm$1.1% in composite galaxies, and 42.6%$\pm$1.1% in AGN-host galaxies. Among 5968 galaxies with S/N $\geq$ 6, f_{SB} is 18.3%$\pm$0.6% in star-forming galaxies, 36.4% $\pm$ 1.3% in composite galaxies, and 43.8% $\pm$ 1.6% in AGN-host galaxies, respectively. In the low S/N case we find that f_{SB} is $\sim$2.5 times higher in AGN-host galaxies than in star-forming galaxies. On the other hand, the fraction of weak-barred galaxies (f_{WB}) does not vary significantly with spectral types, from 6.0% to 7.0%. The result for the high S/N case is not different from that for the low S/N case.

Figure 5.2 presents the change of f_{SB} for the sample of galaxies with S/N $\geq$ 3 in three BPT diagnostic diagrams such as (a) [NII]/Hα versus [OIII]/Hβ, (b) [SII]/Hα versus [OIII]/Hβ, and (c) [OI]/Hα versus [OIII]/Hβ. In panel (b) we use 8508 galaxies with S/N$_{\mathrm{[SII]}}$ $\geq$ 3, while only 5622 galaxies with S/N$_{\mathrm{[OI]}}$ $\geq$ 3 are used in panel (c). We find a noticeable trend that f_{SB} increases continuously from the star-forming galaxy region (lower left) to the AGN-host galaxy region (upper right) in all diagnostic diagrams, showing that the presence of bars is more frequent in AGN-host galaxies than non-AGN galaxies. We check that this trend does not change significantly even when we use the high S/N sample.

Table 5.2. Dependence of Bar Fraction on Spectral Types

(1) S/N[a]$\geq$ 3

Spectral type	Total	SB[b]	f_{SB} (%)[c]	WB[d]	f_{WB} (%)	SB+WB	$f_{\mathrm{SB+WB}}$ (%)
Star-forming	4,940	770	15.6 ± 0.5	348	7.0 ± 0.4	1,118	22.6 ± 0.6
Composite	1,973	639	32.4 ± 1.1	118	6.0 ± 0.5	757	38.4 ± 1.1
AGN-host	1,742	742	42.6 ± 1.1	109	6.3 ± 0.6	851	48.9 ± 1.2

(2) S/N $\geq$ 6

Spectral type	Total	SB	f_{SB} (%)	WB	f_{WB} (%)	SB+WB	$f_{\mathrm{SB+WB}}$ (%)
Star-forming	3,600	659	18.3 ± 0.6	265	7.4 ± 0.4	924	25.7 ± 0.7
Composite	1,411	513	36.4 ± 1.3	67	4.7 ± 0.5	580	41.1 ± 1.3
AGN-host	957	419	43.8 ± 1.6	52	5.4 ± 0.7	471	49.2 ± 1.6

[a]S/N for four emission lines such as Hα, Hβ, [NII] λ6584, and [OIII] λ5007

[b]Strong-barred galaxies

[c]The errors of the bar fraction are obtained by calculating the standard deviation in 1,000-times-repetitive sampling method.

[d]Weak-barred galaxies
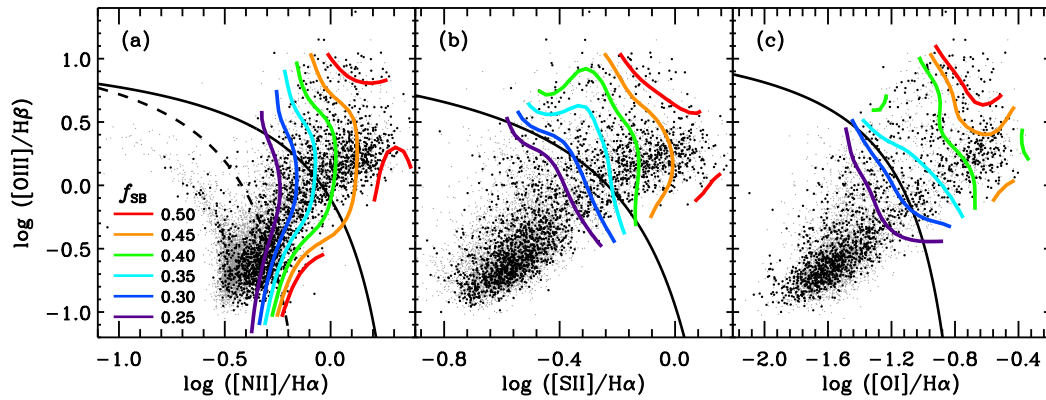
Figure 5.2 The fraction of strong-barred galaxies ($f_{\rm SB}$) in the three BPT diagnostic diagrams: (a) [NII]/Hα versus [OIII]/Hβ, (b) [SII]/Hα versus [OIII]/Hβ, (c) [NII]/Hα versus [OIII]/Hβ. Black dots and grey dots represent strong-barred galaxies and non-SB galaxies, respectively. Contours represent constant $f_{\rm SB}$. In panels (b) and (c) we use only 8,508 galaxies with S/N$_{\rm [SII]} \geq 3$ and 5,622 galaxies with S/N$_{\rm [OI]} \geq 3$.

In the view of the results we obtained above, it is seen that AGN activity is related to the presence of strong bars. However, we will see below that these results do not directly indicate a connection between the presence of strong bars and AGN activity. This is because f_{SB} is also a strong function of galaxy properties, i.e., $u - r$ color, velocity dispersion (σ) and stellar mass (M_{star}). In Lee et al. (2012a), we found that $u - r$ and σ are more influential parameters in determining the bar fraction. Therefore, we need to compare AGN-host and non-AGN galaxies with fixed $u - r$ and σ in order to separate the effect of the two parameters on f_{SB}.

In Figure 5.3 we show the dependence of the bar fraction on three parameters: $u - r$, σ, and M_{star}. M_{star} is another important parameter affecting the bar fraction (e.g., Sheth et al. 2008; Cameron et al. 2010; Méndez-Abreu et al. 2010; Nair & Abraham 2010b). The fraction of strong-barred galaxies increases significantly as $u - r$ color becomes redder, and it has a maximum value at intermediate velocity dispersion of $\sim$130 km s^{-1}. It has a constant value ($\sim$10%) until $\log{(M/M_\odot)} = 10.2$, but increases with M_{star} thereafter. On the other hand, the fraction of weak-barred galaxies shows a different dependency on the three parameters. It has a peak value at a bluer color of $u - r \simeq 1.4$, and becomes larger as σ or M_{star} decreases. This result on M_{star} is consistent with the result of Nair & Abraham (2010b).

Figure 5.4 shows how f_{SB} varies in the $u-r$ versus M_{star} and in the σ versus M_{star} diagrams. It shows that M_{star} has a strong correlation with both $u - r$ and σ. It also shows that f_{SB} increases with the three parameters. However, at $\sigma \gtrsim 120$ km s^{-1} it decreases with σ at a given M_{star} bin. Particularly, contours are neither vertical nor horizontal, suggesting that f_{SB} depends on the three parameters simultaneously. Therefore, we conclude that $u - r$, σ, and M_{star} are all important parameters in determining the bar fraction.

Because f_{SB} is strongly correlated with three parameters, we need to check whether the trend of f_{SB} in Figure 5.2 is originated from the effect of the three
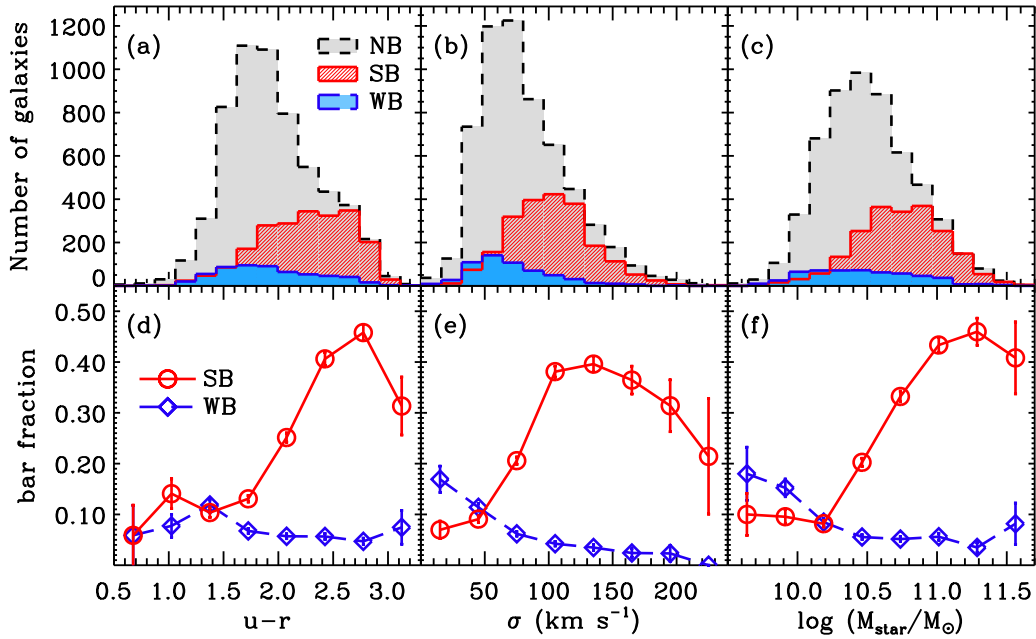
Figure 5.3 (Upper) The number of galaxies as a function of (a) $u - r$ color, (b) velocity dispersion (σ), and (c) stellar mass ($M_{\rm star}$) for strong-barred (SB), weak-barred (WB), and non-barred (NB) galaxies. (Lower) The dependence of the bar fraction on (d) $u - r$, (e) σ, and (f) $M_{\rm star}$. Circles and diamonds represent fractions of SB and WB galaxies, respectively. Error bars mean 1-σ sampling errors estimated by calculating the standard deviation of the bar fraction in 1,000-times-repetitive sampling.

Figure 5.4 The fraction of strong-barred galaxies (f_{SB}) in (a) $u - r$ versus M_{star} diagram and (b) σ versus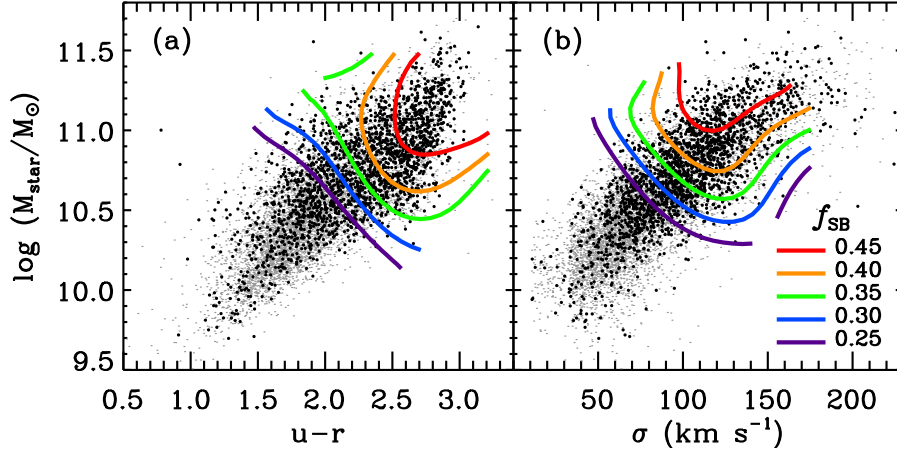 M_{star} diagram. Black dots and grey dots represent strong-barred galaxies and non-SB galaxies, respectively. Contours represent constant strong-barred galaxy fractions.

parameters on f_{SB}. To investigate the difference of $u - r$ and σ between AGN-host and non-AGN galaxies, we examine how $u - r$ and σ vary in the [NII]/Hα versus [OIII]/Hβ diagnostic diagram as shown in Figure 5.5. We use 20×20 bins in this diagram to measure median values of $u - r$ and σ for late-type galaxies at each bin. After excluding bins that contain less than five galaxies, we display representative symbols with various colors and sizes, corresponding to the median values of $u - r$ and σ, respectively. From the star-forming galaxy region toward the AGN-host galaxy region, it seems obvious that $u - r$ color becomes redder. At the same time, σ increases along the same direction. The median values of $u - r$ are 1.77 ± 0.01, 2.20 ± 0.01 and 2.59 ± 0.01, respectively for star-forming, composite, and AGN-host galaxies. In the case of σ, the median values for star-forming, composite, and AGN-host galaxies are 66.2 ± 0.5, 95.1 ± 0.7, and 118.3 ± 0.9 km s^{-1}, respectively. Considering the dependence of f_{SB} on $u - r$ and σ, it is clear that the trend shown

in Figure 5.2 is caused by the fact that f_{SB} increases with $u - r$ and σ (or M_{star}).

To remove the effect of $u - r$, σ, and M_{star}, we investigate the bar fraction in AGN-host and non-AGN galaxies at fixed $u-r$ and σ (or M_{star}), as shown in Figure 5.6. First, we divide our sample into 17 bins with fixed $u-r$ and σ ranges. Note that each bin contains more than fifty galaxies. Then we measure f_{SB} of each spectral type in each bin. An obvious excess of f_{SB} in AGN-host galaxies is found only in one bin with $u - r = 2.1 - 2.4$ and $\sigma = 40 - 80$ km s^{-1}. In contrast, at all other $u-r$ and σ bins, f_{SB} of AGN-host galaxies is similar to that of star-forming galaxies. Second, we perform similar analysis at fixed $u-r$ and M_{star} ranges. We do not found any clear or significant excess of f_{SB} in AGN-host galaxies in all bins. These results clearly demonstrate that the f_{SB} excess in AGN-host galaxies shown in Figure 5.2 is caused by the fact that on average AGN-host galaxies are redder and and more massive than non-AGN galaxies. These results suggest that the bar fraction do not depend on AGN activity.

5.3.2   Dependence of AGN Fraction on Bar Presence

In this section we investigate how AGN fraction changes depending on the presence of bars. Among non-barred or weak-barred galaxies, the fraction of star-forming galaxies ($> 60\%$) is much larger than that of AGN-host galaxies ($< 20\%$) while composite galaxies occupy $\sim 20\%$. In contrast, the AGN fraction increases by a factor of two when galaxies have strong bars. For example, among galaxies with S/N ≥ 3 (S/N ≥ 6), the AGN fraction is 34.5% (26.3%). AGN fractions in strong-barred, weak-barred, and non-barred galaxy samples are summarized in Table 5.3.

To demonstrate the dependence on galaxy properties, we present AGN fraction of barred (combining strong and weak bars) and non-barred galaxies, as a function of $u-r$, σ, and M_{star} in Figure 5.7. In both barred and non-barred galaxy samples, the AGN fraction increases with redder color, higher σ or larger M_{star} while the fraction
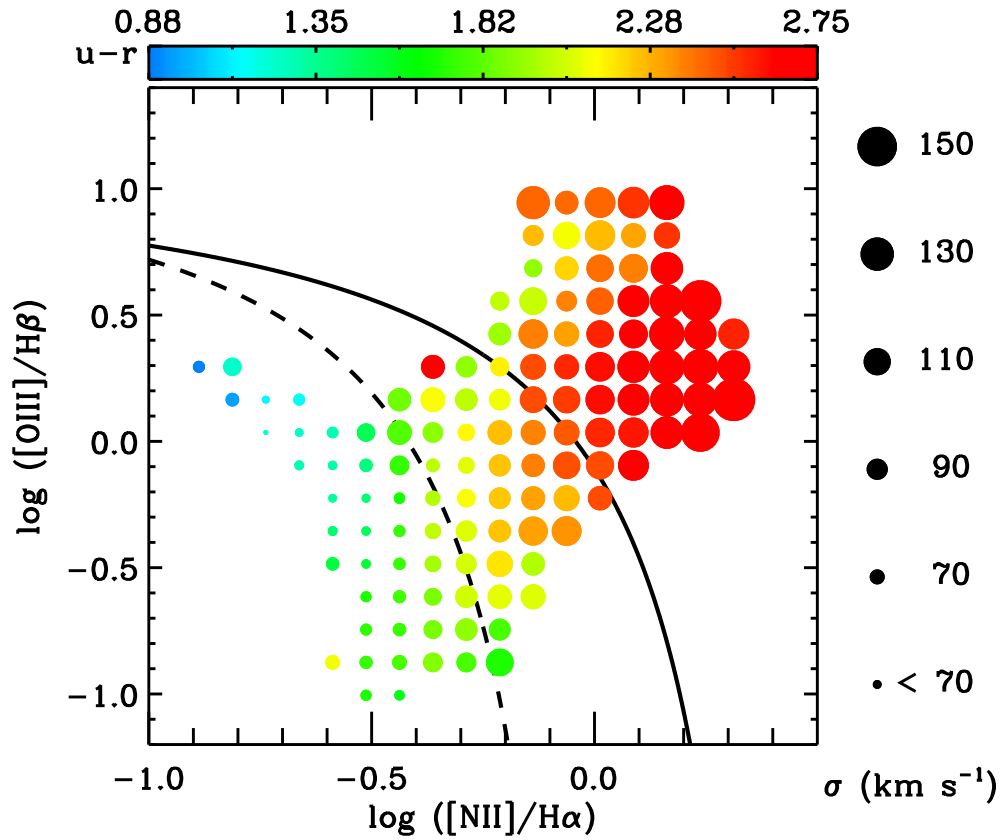
Figure 5.5 Distribution of $u - r$ and σ for 8,655 late-type galaxies in [NII]/Hα versus [OIII]/Hβ diagnostic diagram. We divide this diagram into 20×20 bins and measure median values of $u - r$ and σ for galaxies at each bin. After excluding bins that contain less than five galaxies, we display representative symbols with various colors and sizes, corresponding to the median values of $u - r$ and σ, respectively.
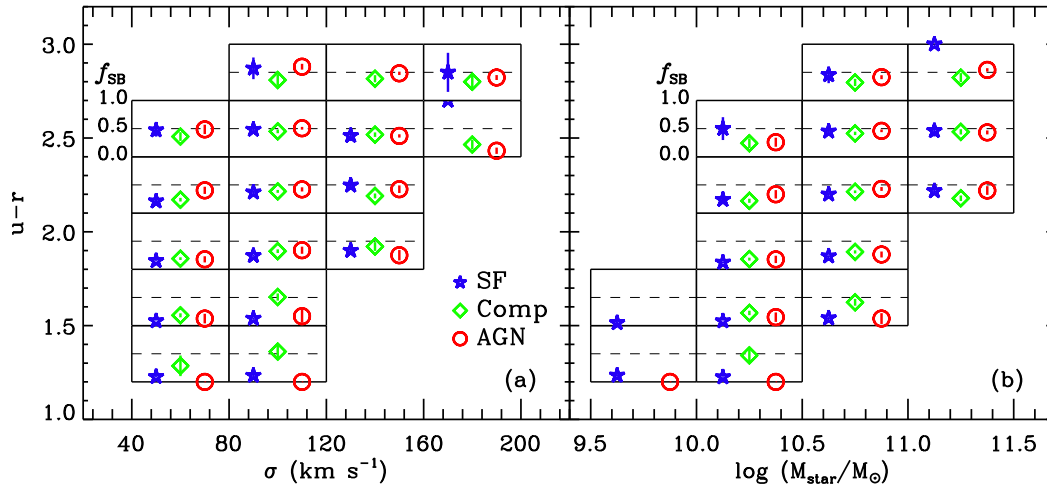
Figure 5.6 Dependence of the fraction of strong-barred galaxies ($f_{\rm SB}$) on spectral types for late-type galaxies with fixed ranges of (a) $u-r$ ($\Delta(u-r) = 0.3$) and velocity dispersion ($\Delta\sigma = 40$ km s^{-1}). (b) Same as (a), but x-axis is log ($M_{\rm star}/M_\odot$) instead of σ. Stars, diamonds, and circles with error bars represent $f_{\rm SB}$ for star-forming, composite, and AGN-host galaxies, respectively.

Table 5.3.   Spectral Classification in Different Bar Types

(1) S/N[a] $\geq$ 3

Spectral type	NB[b]		SB[c]		WB[d]	
	Number	Fraction	Number	Fraction	Number	Fraction
Star-forming	3,822	64.5%	770	35.8%	348	60.5%
Composite	1,216	20.5%	639	29.7%	118	20.5%
AGN-host	891	15.0%	742	34.5%	109	19.0%
Total	5,929	100.0%	2,151	100.0%	575	100.0%

(2) S/N $\geq$ 6

Spectral type	NB		SB		WB	
	Number	Fraction	Number	Fraction	Number	Fraction
Star-forming	2,676	67.0%	659	41.4%	265	69.0%
Composite	831	20.8%	513	32.2%	67	17.4%
AGN-host	486	12.2%	419	26.3%	52	13.5%
Total	3,993	100.0%	1,591	100.0%	384	100.0%

[a]S/N for four emission lines such as Hα, Hβ, [NII] λ6584, and [OIII] λ5007

[b]Non-barred galaxies

[c]Strong-barred galaxies

[d]Weak-barred galaxies

of star-forming galaxies shows an opposite trend. At fixed σ or M_{star}, AGN fraction is significantly higher in barred galaxies than in non-barred galaxies. At fixed $u - r$ color, however, the excess of AGN fraction in barred galaxies is marginal. These results do not significantly change even if we exclude weak bars from the barred galaxy sample. The results presented in Figure 5.7 are similar to the finding of Oh et al. (2011, see their Figure 8), which appeared in the literature during the review process of our manuscript. We note that the sample size in this study is much larger than that in Oh et al. (8655 galaxies versus 3934 galaxies), and that we classify composite galaxies separately instead of including them in the AGN sample.

The results in Figures 5.3, 5.4, and 5.7 show that both bar fraction and AGN fraction increase as galaxy color becomes redder. This leads naturally to an expectation that AGN and bars may be related. However, this does not necessarily mean that both are related. We need to investigate whether AGN is directly connected to bars or not.

For this we investigate whether AGN fraction is different between barred and non-barred galaxies in multi-dimensional spaces as shown in Figure 5.8. When we compare galaxies at fixed ranges of $u - r$ and σ (or M_{star}), the excess of AGN fraction in barred galaxies disappears or weakens. Within the sampling errors, there is no significant difference of AGN fraction between barred and non-barred galaxies. These results are dramatically different from those in Figure 5.7 due to the fact that AGN fraction is dependent of color and σ (or M_{star}). Figure 5.4 shows that $u - r$ has a large dispersion even when M_{star} is fixed. Similarly large color dispersion is also seen when σ is fixed (see Figure 9 in Lee et al. 2012a). Therefore an excess of the AGN fraction in barred galaxies shown in Figure 5.7 is an "apparent" trend, which is caused by the residual dependence on $u - r$ color in σ (or M_{star}) bins. Thus, in order to remove the effect of $u - r$ and σ (or M_{star}), AGN fraction has to be compared using galaxies at fixed $u - r$ and σ (or M_{star}). We find no significant
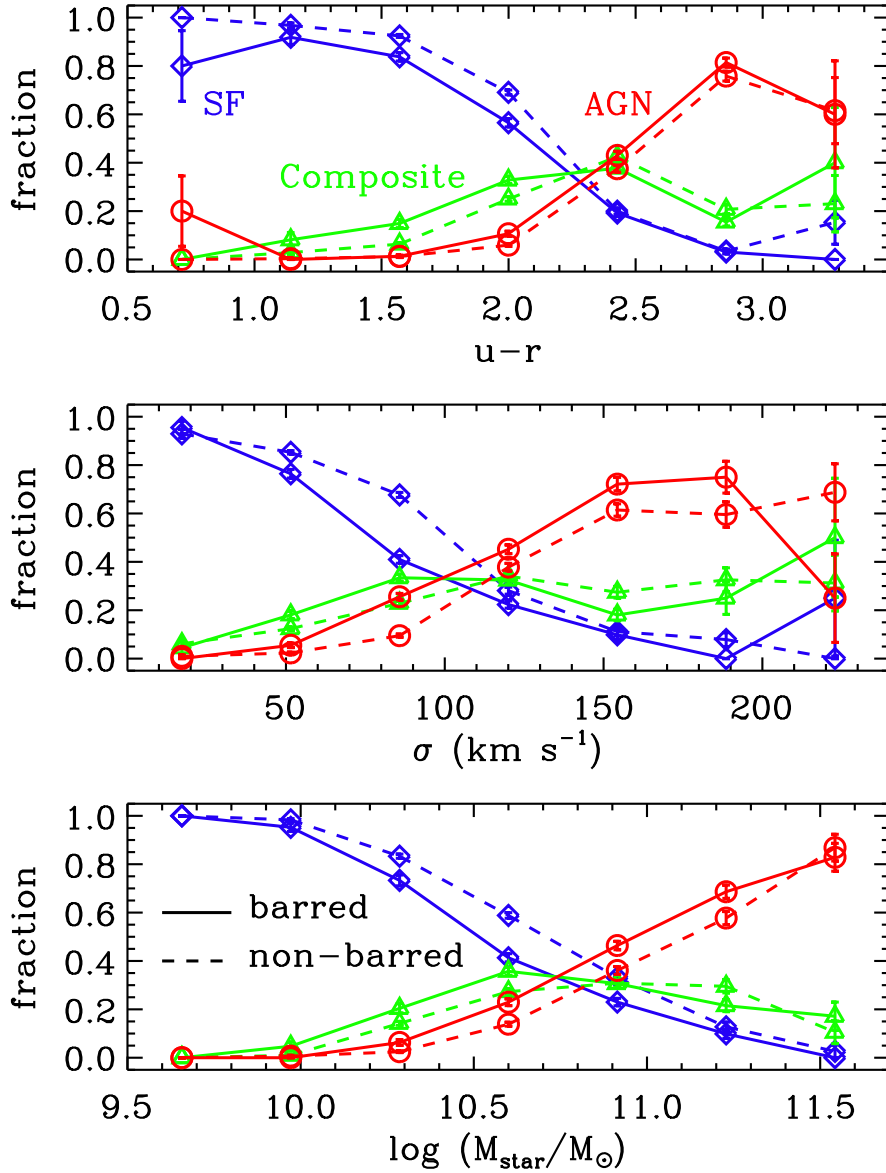
Figure 5.7 The fraction of AGN-host (circles), composite (triangles), and star-forming galaxies (diamonds) as a function of $u - r$ (top), σ (middle), and M_{star} (bottom). Solid lines and dashed lines represent barred (strong and weak-barred) and non-barred galaxies, respectively. Error bars mean 1-σ sampling errors.
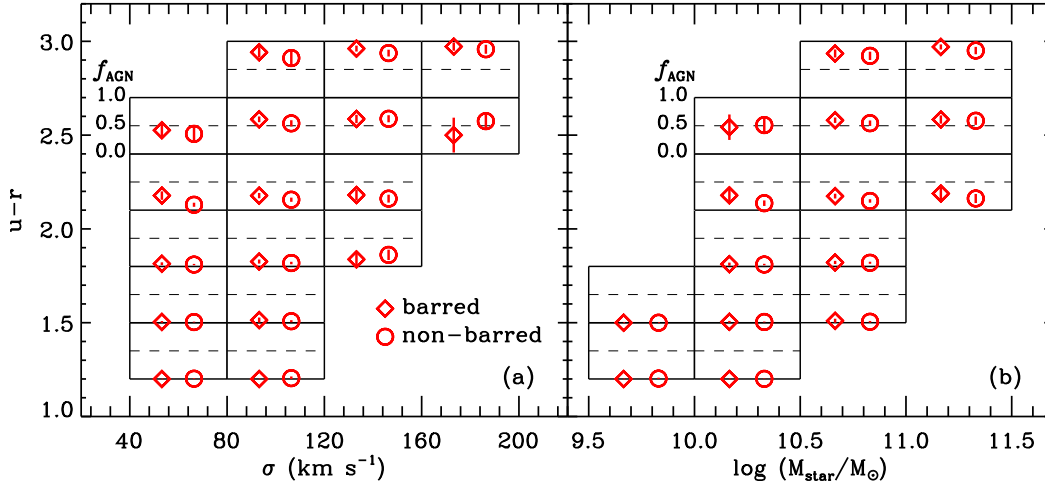
Figure 5.8 The dependence of the AGN fraction ($f_{\rm AGN}$) on the presence of bars at fixed ranges of (a) $u-r$ and σ and (b) $u-r$ and $M_{\rm star}$. Diamonds and circles represent $f_{\rm AGN}$ for barred (strong and weak-barred) and non-barred galaxies, respectively. Error bars represent 1-σ sampling errors.

dependence of AGN fraction on the presence of bars, suggesting that AGN activity is not dominated by bars.

5.3.3   Comparison of Eddington Ratio between Barred and Non-barred AGN-host Galaxies

If AGN activity is triggered by bars, barred galaxies may have higher accretion rates than non-barred galaxies. We exclusively use AGN-host galaxies to examine whether there is any difference in AGN power between barred and non-barred galaxies.

We use the [OIII] luminosity ($L_{\rm [OIII]}$) as a proxy for the bolometric luminosity and infer black hole mass ($M_{\rm BH}$) from σ using Eq. (2) as described below. Thus, $L_{\rm [OIII]}$ to $M_{\rm BH}$ ratio can be used as an approximate Eddington ratio indicator. We adopt a reddening curve of $R_V = A_V/E(B-V) = 3.1$ (Cardelli et al. 1989) and an

intrinsic Balmer decrement of $H\alpha/H\beta = 3.1$ for AGN-host galaxies (Osterbrock & Ferland 2006) to correct for internal dust extinction. To estimate M_{BH}, we adopt a $M_{BH} - \sigma$ relation for late-type galaxies suggested by McConnell et al. (2011):

$$\log\ (M_{BH}/M_\odot) = 7.97 + 4.58 \times \log\ (\sigma/200 \text{km s}^{-1}). \qquad (5.2)$$

We exclude galaxies with velocity dispersion values lower than the instrumental resolution of the SDSS spectra ($\sigma < 70$ km s^{-1}) since these measurements are not reliable (Choi et al. 2009). In the following analysis we use two samples: 1647 AGN-host galaxies with S/N $\geq$ 3 and 893 ones with S/N $\geq$ 6. The low S/N sample contains 718 strong-barred, 97 weak-barred, and 832 non-barred galaxies. On the other hand, the high S/N sample consists of 407 strong-barred, 46 weak-barred, and 440 non-barred galaxies. The black hole mass of AGN-host galaxies spans $5.9 < \log$ $(M_{BH}/M_\odot)< 8.3$, while $L_{[OIII]}/M_{BH}$ ranges over four order of magnitude, $10^{-2} - 10^2$ $L_\odot/M_\odot$.

In Figure 5.9 we present the Eddington ratio indicator (hereafter Eddington ratio) distributions as a function of $u - r$, σ, and M_{star}, respectively, for strong-barred, weak-barred, and non-barred galaxies. The AGN power (i.e., Eddington ratio) appears to decrease with M_{star} (or σ) as previously seen by Hwang et al. (2012c). This trend can be interpreted as "Eddington incompleteness", which reflects the observational selection effect that for given flux (or luminosity limits) lower Eddington ratio AGNs can be detected at higher mass scales. Since at a fixed Eddington ratio it is harder to detect [OIII] lines for lower mass black holes, the Eddington ratios can be distributed down to a much lower values for higher mass black holes and galaxies as shown in Figure 5.9. In addition, we find that the AGN power is correlated with $u - r$ of galaxies. Blue AGN-host galaxies show significantly higher Eddington ratio than red AGN-host galaxies, implying that gas-rich systems generally have higher Eddington ratio than gas-poor systems. However, we note that this correlation can be also caused by the Eddington incompleteness since bluer color galaxies have on

average lower galaxy (hence black hole) mass.

Nevertheless, we can compare the distributions of the Eddington ratio among strong-barred, weak-barred, and non-barred galaxies. We measure median values of $\log (L_{[OIII]}/M_{BH})$ as a function of $u - r$, σ, and M_{star} for each bar class. In panel (a) and (d), it is shown that median curves for strong-barred and weak-barred galaxies lie slightly above those for non-barred galaxies, although the differences between barred and non-barred galaxies are not significant and the median Eddington ratios are consistent within the error. In other panels there is no difference between barred and non-barred AGN-host galaxies over the whole ranges of σ and M_{star}.

To avoid the effect of Eddington incompleteness, we plot the Eddington ratio versus $u - r$ diagram at two fixed σ ranges in Figure 5.10. The anti-correlation between the Eddington ratio and $u - r$ is still present for both 70 km s^{-1} $< \sigma \leq$ 120 km s^{-1} and 120 km s^{-1} $< \sigma \leq$ 170 km s^{-1} ranges, indicating that AGN power is correlated with the amount of cold gas in galaxies. Choi et al. (2009) also found a similar result among late-type AGN-host galaxies with $7 < \log M_{BH}/M_\odot < 8$. We note that the contributions to the [OIII] lines from star formation can systematically increase the $L_{[OIII]}/M_{BH}$ ratio in bluer galaxies. Thus, further analysis is required to explore the connection between the presence of gas in large scales and the Eddington ratio.

When we compare the Eddington ratio distributions of barred and non-barred galaxies in Figure 5.10, the median values of the Eddington ratio are not significantly different, implying that AGN power is not strongly affected by the presence of bars. Considering the scatter in each bin, and the uncertainty and systematic errors in estimating black hole masses from the $M_{BH} - \sigma$ relation, we conclude that there is no strong difference of the Eddington ratios between barred and non-barred galaxies.
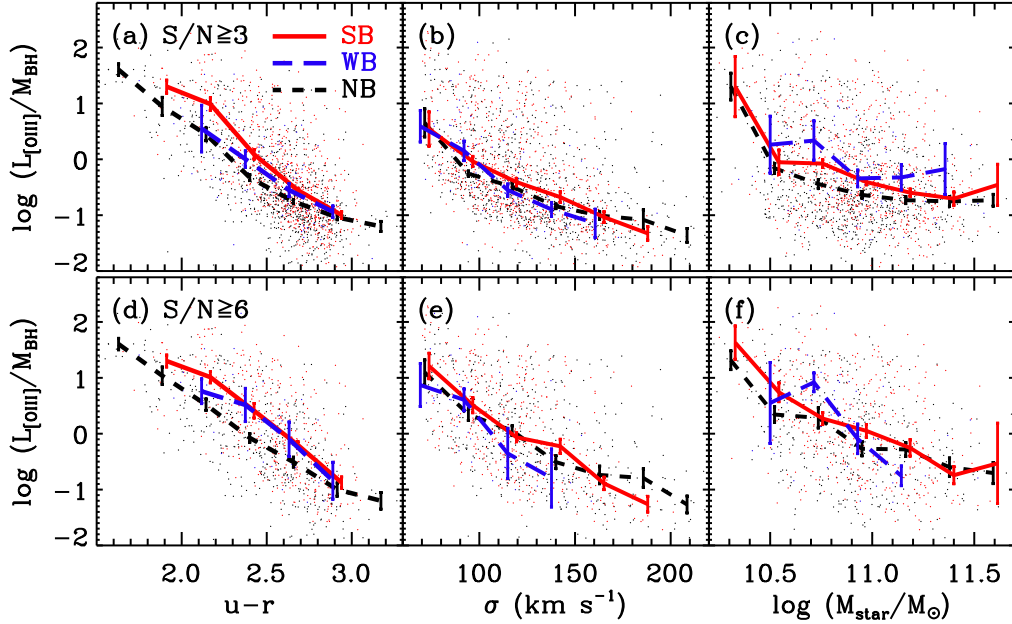
Figure 5.9 Eddington ratio as a function of (left) $u-r$, (middle) σ, and (right) M_{star} for 1,647 (upper, S/N $\geq$ 3) and 893 (lower, S/N $\geq$ 6) late-type AGN-host galaxies with $\sigma > 70$ km s^{-1}. Solid lines, long-dashed lines, and short-dashed lines represent median curves of Eddington ratio for strong-barred (SB), weak-barred (WB), and non-barred (NB) AGN-host galaxies, respectively. The size of bins corresponds to 1/7 of x-axis of each panel, and only when bins contain more than five galaxies median values of Eddington ratio are drawn. Error bars are calculated using 1,000-times resampling method. Error bars for strong-barred and weak-barred galaxies are slightly shifted respect to ones of non-barred galaxies in order to avoid overlap each other.
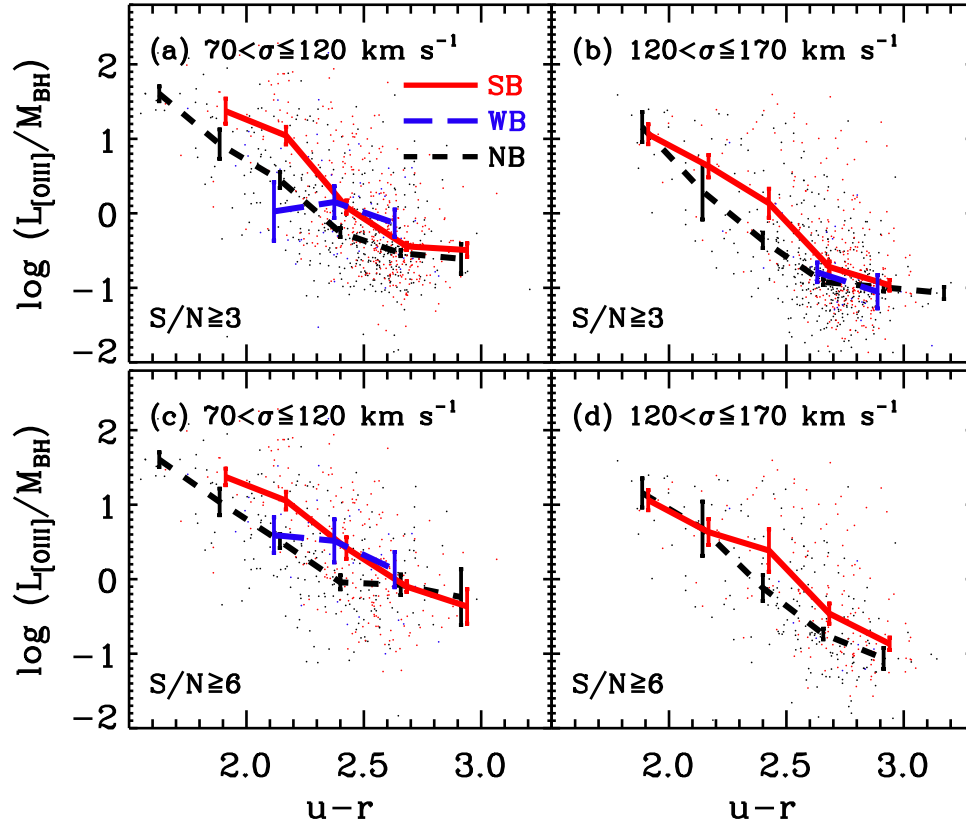
Figure 5.10 Eddington ratio versus $u-r$ for late-type AGN-host galaxies with (upper) S/N $\geq$ 3, (lower) S/N $\geq$ 6, (left) 70 km s^{-1} < σ $\leq$ 120 km s^{-1}, and (right) 120 km s^{-1} < σ $\leq$ 170 km s^{-1}. Solid lines, long-dashed lines, and short-dashed lines represent median curves of Eddington ratio for strong-barred (SB), weak-barred (WB), and non-barred (NB) galaxies, respectively. The size of bins corresponds to 1/7 of x-axis of each panel, and only when bins contain more than five galaxies median values of Eddington ratio are drawn. Error bars are calculated using 1,000-times resampling method. Error bars for strong-barred and weak-barred galaxies are slightly shifted respect to ones of non-barred galaxies in order to avoid overlap each other.

5.4   Discussion

5.4.1   Do AGNs Favor Barred Galaxies?

Over the last three decades, bars have been invoked as a mechanism for fueling SMBHs. Although some studies claimed that AGNs are more frequently found in barred galaxies (Arsenault 1989; Knapen et al. 2000; Laine et al. 2002), no excess of bars in AGN-host galaxies has been reported by many other statistical studies (Moles et al. 1995; McLeod & Rieke 1995; Mulchaey & Regan 1997; Ho et al. 1997; Laurikainen et al. 2004; Hao et al. 2009). This discrepancy was at least in part caused by the small sample size, selection effect, and contamination owing to the correlation between bars and other galaxy properties, i.e., color and stellar mass.

In this study we find that the fraction of strong bars is $\sim$2.5 times higher in AGN-host galaxies than in non-AGN galaxies. This result is clearly different from the findings by Hao et al. (2009), who claimed no excess of bar fraction in AGN-host galaxies based on a sample of 1,144 SDSS disk galaxies with $-18.5 > M_g > -22.0$ at $0.01 < z < 0.03$. The discrepancy is due to the combination of two effects. First, by using a color cut (Bell et al. 2004; Barazza et al. 2008) in selecting disk galaxies, Hao et al. (2009) inevitably excluded red disk galaxies, leading to a much lower AGN fraction in their sample (11.1%) than that in our sample (17.0%). Second, they used the ellipse fitting method to identify bars. In general the bar fraction based on the ellipse fitting (e.g., $\sim$50% in r-band: Barazza et al. 2008) is much higher than that obtained by visual inspection (e.g., $\sim$33% in B-band: de Vaucouleurs et al. 1991, 26% $\pm$ 0.5% in $g + r + i$ color images: Nair & Abraham 2010a, 29.4% $\pm$ 0.5% from Galaxy Zoo: Masters et al. 2010, 30.4%: Lee et al. 2012a, 36%: Oh et al. 2011). Thus, the combined effects of differences in sample selection and the classification method between Hao et al. and ours result in different findings.

We also find that the AGN fraction is twice higher in strong-barred galaxies

than in non-barred galaxies as previous studies similarly reported (Arsenault 1989; Knapen et al. 2000; Laine et al. 2002). As shown in Figure 5.7, the higher AGN fraction in barred systems is present over a large ranges of M_{star}. This result is consistent with those of recent studies (Coelho & Gadotti 2011; Oh et al. 2011).

However, the excess of the bar fraction in AGN-host galaxies and the excess of the AGN fraction in barred galaxies do not indicate that the presence of bars and AGN activity are directly connected since the excess of the bar fraction in AGN-host galaxies and the excess of the AGN fraction in barred galaxies disappear when we compare galaxies with the same $u - r$ and σ (or M_{star}) (see Figure 5.6 and Figure 5.8). Thus, we conclude that AGN activity is not dominated by the presence of bars.

Comparing the Eddington ratios among AGN-host galaxies, we find no significant difference between barred and non-barred galaxies at fixed $u - r$, σ and M_{star} bins (see Figure 5.9), indicating that AGN power is not enhanced by the presence of bars.

Among AGN host galaxies with $2.0 < u - r < 2.5$, the Eddington ratios are marginally higher in strong-barred galaxies than in non-barred galaxies (see Figure 5.10), possibly implying that strong bars can boost AGN activity when their host galaxies lie in green valley. However, the number of AGN-host galaxies in our sample is not enough to draw a clear conclusion.

5.4.2 Dependence on the $M_{\mathrm{BH}} - \sigma$ Relation

Since we estimate black hole masses from stellar velocity dispersion utilizing the $M_{\mathrm{BH}} - \sigma$ relation, the derived Eddington ratios depend on the slope and intercept of the $M_{\mathrm{BH}} - \sigma$ relation. Thus, it is necessary to investigate whether the Eddington ratio difference between barred and non-barred galaxies depends on the adopted $M_{\mathrm{BH}} - \sigma$ relation.

Over the last decade, empirical scaling relations between M_{BH} and σ have been improved as the number of galaxies with M_{BH} measurements increased (e.g., Fer-

rarese & Merritt 2000; Gebhardt et al. 2000; Tremaine et al. 2002; Gültekin et al. 2009b; Graham & Li 2009; Woo et al. 2010). By combining two new M_{BH} measurements with the literature data published before August 2011, a recent study by McConnell et al. (2011) provided two $M_{\mathrm{BH}} - \sigma$ relations; log $(M_{\mathrm{BH}}/M_\odot) = \alpha + \beta$ log $(\sigma/200\mathrm{km\ s}^{-1})$ with $(\alpha, \beta) = (8.38 \pm 0.06, 4.53 \pm 0.40)$ for elliptical/S0 galaxies and $(7.97 \pm 0.22, 4.58 \pm 1.25)$ for spiral galaxies. In this study we adopt the second equation for estimating M_{BH} since our sample is composed of late-type galaxies.

A few studies separately derived $M_{\mathrm{BH}} - \sigma$ relations for barred and non-barred galaxies (Gültekin et al. 2009b; Graham & Li 2009; Graham et al. 2011). For example, Gültekin et al. (2009b) reported $(\alpha, \beta) = (8.19 \pm 0.087, 4.21 \pm 0.446)$ for non-barred and $(7.67 \pm 0.115, 1.08 \pm 0.751)$ for barred galaxies while Graham & Li (2009) derived $(8.15 \pm 0.05, 3.89 \pm 0.18)$ for non-barred galaxies, and $(8.03 \pm 0.05, 3.94 \pm 0.19)$ for the combined sample of barred and non-barred galaxies. Graham et al. (2011) reported steeper $M_{\mathrm{BH}} - \sigma$ relations with $(8.25 \pm 0.06, 4.57 \pm 0.35)$ for non-barred galaxies and $(7.80 \pm 0.10, 4.34 \pm 0.56)$ for barred galaxies.

To demonstrate the dependence of Eddington ratios on the adopted $M_{\mathrm{BH}} - \sigma$ relation, in Figure 5.11 we compare Eddington ratios between barred and non-barred galaxies using three different pairs of $M_{\mathrm{BH}} - \sigma$ relations mentioned above. When the $M_{\mathrm{BH}} - \sigma$ relations from Gültekin et al. (2009b) are used, barred and non-barred galaxies show no significant difference in Eddington ratios as similarly shown in Figure 5.9. In contrast, Eddington ratios tend to be higher in barred galaxies than in non-barred galaxies when the $M_{\mathrm{BH}} - \sigma$ relations are taken from Graham & Li (2009). The enhanced Eddington ratios in barred galaxies is particularly noticeable when using Graham et al. (2011)'s $M_{\mathrm{BH}} - \sigma$ relations. since M in barred galaxies are significantly reduced due to the lower intercept of the $M_{\mathrm{BH}} - \sigma$ relation.

If we adopt different $M_{\mathrm{BH}} - \sigma$ relations respectively for barred and non-barred
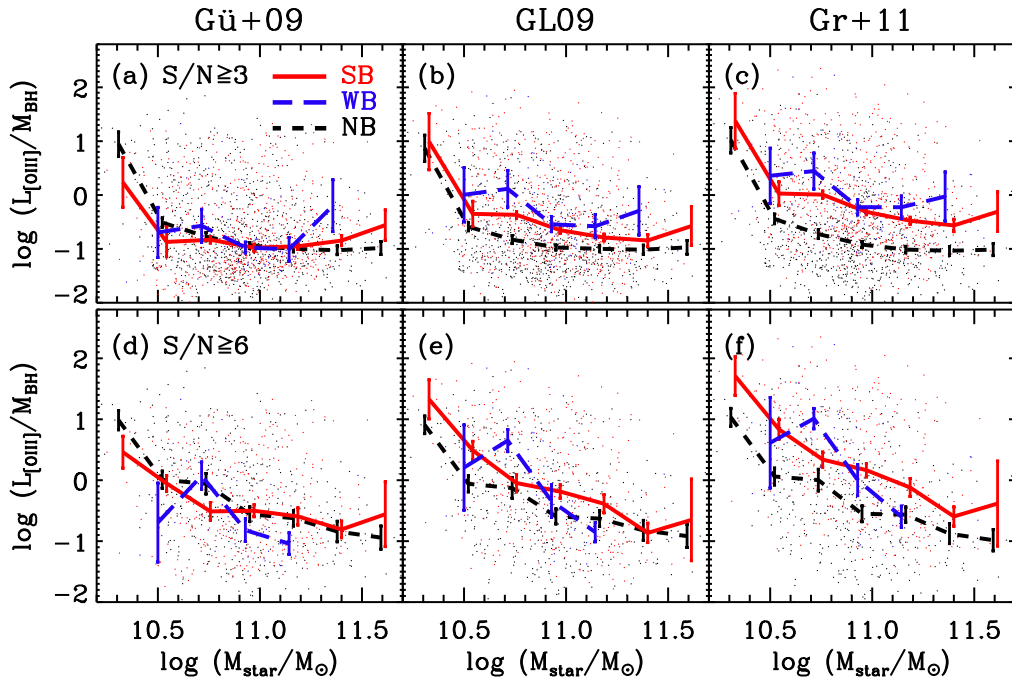
Figure 5.11 Comparison of Eddington ratio as a function of M_{star} between strong-barred (SB), weak-barred (WB), and non-barred (NB) AGN-host galaxies with (upper) S/N $\geq$ 3, (lower) S/N $\geq$ 6, when adopting $M_{BH} - \sigma$ relations given by (left) Gültekin et al. (2009b): $(\alpha, \beta) = (7.67, 1.08)$ for barred and (8.19,4.21) for non-barred, (middle) Graham & Li (2009): (8.03,3.94) for barred and (8.15,3.89) for non-barred, and (right) Graham et al. (2011): (7.80,4.34) for barred and (8.25,4.57) for non-barred galaxies, respectively.

galaxies, AGN power appears to be enhanced by bars. Oh et al. (2011) used the $M_{BH} - \sigma$ relations taken from Graham & Li (2009), and they argued that AGN strength is enhanced by the presence bars. However, there are several limitations in adopting two different relations for barred and non-barred. First, the $M_{BH} - \sigma$ relation of barred galaxies is not well defined since the relation has been derived with a small number of barred galaxies. For example, Gültekin et al. (2009b) used only 8 measurements (and 11 upper limits of M_{BH}) of barred galaxies while Graham et al. (2011) also used only 20 barred galaxies. Second, the $M_{BH} - \sigma$ relation of non-barred galaxies are biased to early-type galaxies since early-type galaxies are dominant in the sample. Third, dynamical mass measurements of black holes in barred galaxies are much more uncertain since no stellar dynamical model truly accounts for stellar bars (Gültekin et al. 2009a). Therefore, we decide to use only one $M_{BH} - \sigma$ relation for late-type galaxies as given in McConnell et al. (2011), in order to avoid any systematic uncertainties of the $M_{BH} - \sigma$ relations between barred and non-barred galaxies. It is necessary to investigate whether barred galaxies have higher Eddington ratios than non-barred galaxies when more robust $M_{BH} - \sigma$ relations of barred and non-barred late-type galaxies become available in the future.

5.4.3   What Triggers AGNs?

Based on the statistical analysis using a large sample of $\sim$9000 late-type galaxies, we find that AGN activity is not dominated by the presence of bars. Then, what triggers AGNs?

Several numerical simulations suggested that interactions and mergers between galaxies are main triggers for AGN activity (Noguchi 1987; Hernquist 1989; Barnes & Hernquist 1992, 1991; Mihos & Hernquist 1996; Di Matteo et al. 2005; Hopkins et al. 2006; Debuhr et al. 2011). This scenario is supported by several observational studies. For example, Sanders et al. (1988) showed that ultra-luminous infrared galaxies

(ULIRG) and quasars are formed through the strong interaction or merger between gas-rich spirals. Bahcall et al. (1997) found that twenty nearby luminous quasars ($z < 0.3$) in their sample have galaxy companions that are closer than 25 kpc. In the case of lower luminosity AGNs, i.e., Seyfert galaxies, minor mergers between gas rich galaxies and with their satellite galaxies are proposed as a mechanism for triggering AGN activity (e.g., De Robertis et al. 1998). However, some observational studies showed conflicting results. Fuentes-Williams & Stocke (1988) found a marginal evidence that Seyfert galaxies interact with their companions that have comparable sizes. In addition, by investigating the environmental dependence of AGN fraction using the SDSS sample, Miller et al. (2003) claimed that the fraction of AGN-host galaxies is independent on environment (see also, Coziol et al. 1998b; Shimada et al. 2000; Schmitt 2001).

Recently, Martínez et al. (2010) reported that AGN-host galaxies (45%) are more frequent than composite (23%) or star-forming galaxies (32%) in the Hickson compact group environment where galaxy-galaxy interactions occur violently. Hwang et al. (2012c) and Choi et al. (in prep.) also found, using the SDSS data, that the AGN fraction increases as the distance to a nearest late-type neighbor galaxy decreases in both cluster and field environments, and concluded that AGN activity can be triggered through mergers and interactions between galaxies when gas supply for AGN is available. In contrast, da Silva et al. (2011) claimed that merging galaxies with signatures of recent starburst, found in the green valley, had no detectable AGN activity. Although it is theoretically clear that mergers and interactions between galaxies can provide advantages for AGN activity by reducing angular momentum of interstellar medium and by generating gas inflows to the center of galaxies, observational studies do not clearly show the connection between galaxy interaction and AGN activity.

Additional mechanisms are expected to occur at subkiloparsec scales in order

to influence the central black hole directly. Secondary bars residing in the nuclear region, which are often called as nested bars, nuclear bars or inner bars, have been a strong candidate. Some observational works (Shaw et al. 1995; Wozniak et al. 1995; Friedli et al. 1996; Mulchaey & Regan 1997; Jungwiert et al. 1997; Greusard et al. 2000; Emsellem et al. 2001, 2006; Laurikainen et al. 2007) found secondary bars in the central region of galaxies. These secondary bars are predicted by the "bars within bars" scenario (Shlosman et al. 1989). The dynamical and kinematical properties of secondary bars are investigated by simulations (Englmaier & Shlosman 2004; Maciejewski & Athanassoula 2008; Shen & Debattista 2009, 2011) and by observations (Garcia-Burillo et al. 1998; Schinnerer et al. 2006; de Lorenzo-Cáceres et al. 2008). Similarly, nuclear dust spirals are invoked as a means to transport material from kiloparsec scales down to sub-kpc scales. High resolution images from HST provided a close look at dusty structures in nuclear regions (Malkan et al. 1998; Regan & Mulchaey 1999; Martini & Pogge 1999; Pogge & Martini 2002). Martini et al. (2003) classified nuclear spirals into several morphological types: grand-design, tightly wound, loosely wound, chaotic nuclear spirals. Recently, Hopkins & Quataert (2010) showed that gas structures formed by gravitational instabilities at several parsec scale have diverse morphologies: spirals, rings, clumps and also bars. So, they proposed "stuff within stuff" model that is a revised version of Shlosman et al. (1989)'s model. However, there is another argument that the presence of nuclear spirals is not also directly connected with current AGN activity, because the frequency of nuclear spirals in AGN-host galaxies is comparable with that in non-AGN galaxies (Martini et al. 2003). Thus, further studies are needed to investigate any relation between nuclear spirals (or secondary bars) and activity in galactic nuclei.

5.5 Summary and Conclusions

We investigate the relation between the presence of bars and AGN activity, using a sample of 8655 late-type galaxies with $b/a > 0.6$ and $M_r < -19.5$ at $0.02 \leq z \leq 0.05489$, selected from the SDSS DR7. We divide these galaxies into three spectral types: star-forming, composite, and AGN-host galaxies, and classified them into barred (storng & weak) and non-barred galaxies by visual inspection. We summarize our main findings as follows.

1. The strong bar fraction is ∼2.5 times higher in AGN-host galaxies than in star-forming galaxies. However, the excess of f_{SB} is caused by the fact that AGN-host galaxies have on average redder $u-r$ color and higher σ than non-AGN galaxies since f_{SB} is higher for redder and more massive (higher σ) galaxies. The excess of f_{SB} in AGN-host galaxies disappears when galaxies with the same $u - r$ and σ (or M_{star}) are compared, indicating that f_{SB} do not depend on AGN activity.

2. Strong-barred galaxies have higher AGN fraction than weak-barred or non-barred galaxies. However, we find no difference of the AGN fraction between barred and non-barred galaxies, when we compare galaxies with the same $u - r$ color and σ (or M_{star}), indicating that AGN activity is not dominated by the presence of bars.

3. Among AGN-host galaxies, barred and non-barred systems show similar Eddington ratio distributions as a function of $u - r$, σ, and M_{star}, implying that AGN power is not enhanced by bars.

In conclusion we do not find any evidence that bars trigger AGN activity. Thus we argue that there is no direct connection between AGN activity and the presence of bars.

Chapter 6

Summary and Conclusions

In this thesis, we presented four studies on environmental mechanisms that trigger galaxy transition from star-forming into quiescent, and what happens during the galaxy transition phase. We used multi-wavelength (from NUV to MIR) data of galaxies in different environments and different evolutionary stages.

In Chapter 2 we presented MIR properties of galaxies in the A2199 supercluster and their environmental dependence. We calculated $\Sigma\mathrm{SFR}/M_{200}$ of the groups and clusters in the A2199 supercluster, and found that $\Sigma\mathrm{SFR}/M_{200}$ does not depend on the virial mass M_{200} of the system. This result suggests that group/cluster mass does not play an important role in controlling the global star formation activity of the galaxy systems. There could be other mechanisms affecting the global star formation activity of the galaxy systems.

On the other hand, in the *WISE* $[3.4] - [12]$ color versus 12 μm luminosity diagram, we defined the MIR green valley, and classified galaxies into three MIR classes: MIR blue cloud galaxies, MIR star-forming sequence galaxies, and MIR green valley galaxies. The MIR blue cloud galaxies are dominated by early-type galaxies, while the MIR star-forming sequence galaxies are predominantly late types. The MIR green valley galaxies consist of 68% of early types and 32% of late types. Both

the MIR blue cloud galaxies and the MIR green valley galaxies are mostly located in the optical red sequence, which indicates that the two MIR classes can not be distinguished from each other in optical color-magnitude (or color-mass) diagram, and that the MIR green valley galaxies are not the same as the optical green valley galaxies.

We compare the cumulative distribution of Σ_5 and R/R_{200} for the three MIR classes. The MIR green valley galaxies show the distribution between the MIR blue cloud galaxies and the MIR star-forming sequence galaxies. When considering only early-type galaxies, the difference in the distribution between the MIR green valley galaxies and the MIR blue cloud galaxies disappears. However, the difference is still found when considering only late-type galaxies. Thus, we conclude that the MIR green valley is the site where morphology transformation mainly appears to occur, and that environment affects the morphology transformation.

In Chapter 3, we presented a MIR study of compact group galaxies and their environmental dependence. In this study, we used a volume-limited sample of 670 compact groups and their 2175 member galaxies with $M_r < -19.77$ and $0.01 < z < 0.0741$, which is drawn from the catalog of Sohn et al. (2016). This catalog was constructed by applying a friends-of-friends algorithm without applying Hickson's isolation criterion, which makes this catalog include both nearby compact groups and embedded compact groups in high-density regions that were excluded from previous catalog. Using this catalog, we studied the relation between compact groups and their surrounding environments without any sample bias.

We used three environmental parameters such as N_{nei}, f_{E}, and σ_{CG} to represent the internal and external environment of the compact groups. We found that regardless of the three environmental parameters the MIR colors of compact group early-type galaxies are on average bluer than those of cluster ($R < 0.5R_{200}$) early-type galaxies. This suggests that early-type galaxies in compact groups are on av-

erage older than those in cluster environment. Compact group late-type galaxies are also on average bluer in MIR colors than cluster late-type galaxies. This implies that star formation activity of late-type galaxies is suppressed more efficiently in compact groups than in clusters. However, in the case of compact groups with $f_{\rm E} = 0$, MIR colors of late-type galaxies are not bluer than those of cluster late-type galaxies, which suggests that suppressed star formation activity of late-type galaxies in the $f_{\rm E} > 0$ compact groups likely results from hydrodynamic interactions with early-type member galaxies.

As compact groups are located in denser regions (as $N_{\rm nei}$ increases), compact groups exhibit larger $f_{\rm E}$, redder optical colors, and bluer MIR colors. These trends are also seen for neighboring galaxies around compact groups. This similar $N_{\rm nei}$-dependence for compact group member galaxies and their neighboring galaxies is not well explained by the morphology-density or SFR-density relations. It is because that compact groups are extremely dense environments. This result can be explained by the scenario that neighboring galaxies are sources of compact group member galaxies, which is consistent with the replenishment model suggested by Diaferio et al. (1994). We presented the first observational evidence supporting the replenishment model.

Even though compact group member galaxies and their neighboring galaxies show the similar $N_{\rm nei}$-dependence, the member galaxies always have larger $f_{\rm E}$ and bluer MIR colors than neighboring galaxies. This means that compact groups are not simply aggregates of captured neighboring galaxies. Furthermore, it suggests that compact group environment plays a critical role in accelerating morphology transformation and star formation quenching for their member galaxies.

In Chapter 4, we studied the spatial distribution of stellar populations in nearby five E+A galaxies ($z \simeq 0.04$) using IFU data from GMOS observations. Numerical simulations expect that the E+A signature tends to be localized within the central (< 1 kpc) regions. Indeed, the findings of Pracy et al. (2013) corroborate this pre-

diction. However, several other past studies suggested show that this is not always the case. Our results also show that all five E+A galaxies in our sample show negative $H\delta_A$ gradients, but that the slopes of the $H\delta_A$ gradients are significantly flatter than those reported in Pracy et al. (2013). This result suggests that A stars are not always confined to the central 1 kpc regions. Furthermore, we found a negative correlation between the slope of these $H\delta_A$ gradients and the fractions of stellar mass produced during starburst. This correlation can be understood if E+A galaxies with stronger starbursts have more centrally-concentrated bursts, or can arise from just small statistics. In order to verify this tentative correlation, we will obtain more IFU data of nearby E+As with full range of burst mass fractions.

In Chapter 5, we investigated the relation between the presence of bars and AGN activity. We used a sample of ∼9000 late-type galaxies with $M_r < -19.5$ and $0.02 \leq z \leq 0.05489$, drawn from the SDSS DR7. We found that the bar fraction is more than two times higher in AGN than in star-forming galaxies. However, when $u-r$ or velocity dispersion (or stellar mass) is fixed, the difference in the bar fraction between AGN and star-forming galaxies disappears. On the other hand, the AGN fraction is higher in barred galaxies than in non-barred galaxies. However, this AGN enhancement in barred galaxies also disappears if we compare the AGN fraction in a fixed $u - r$ or velocity dispersion bin. These results suggest that AGN do not prefer barred galaxies. Among AGN galaxies, barred galaxies and non-barred galaxies show similar Eddington ratio distributions as a function of $u - r$, velocity dispersion, or stellar mass. This implies that there is no difference in AGN power between barred and non-barred galaxies. In conclusion, we did not find clear evidence that bars trigger AGN activity. Therefore, our answer to the question "Do bars trigger activity in galactic nuclei?" is "No".

Bibliography

Abazajian, K. N., Adelman-McCarthy, J. K., Agüeros, M. A., et al. 2009, ApJS, 182, 543

Abell, G. O. 1965, ARA&A, 3, 1

Adelman-McCarthy, J. K., Agüeros, M. A., Allam, S. S., et al. 2008, ApJS, 175, 297

Aguerri, J. A. L., & González-García, A. C. 2009, A&A, 494, 891

Aguerri, J. A. L., Méndez-Abreu, J., & Corsini, E. M. 2009, A&A, 495, 491

Alam, S., Albareti, F. D., Allende Prieto, C., et al. 2015, ApJS, 219, 12

Alatalo, K., Cales, S. L., Appleton, P. N., et al. 2014, ApJ, 794, L13

Amram, P., Mendes de Oliveira, C., Plana, H., Balkowski, C., & Hernandez, O. 2007, A&A, 471, 753

Ann, H. B., & Lee, H.-R. 2013, Journal of Korean Astronomical Society, 46, 141

Appleton, P. N., Xu, K. C., Reach, W., et al. 2006, ApJ, 639, L51

Arnouts, S., Cristiani, S., Moscardini, L., et al. 1999, MNRAS, 310, 540

Arsenault, R. 1989, A&A, 217, 66

Athanassoula, E. 2003, MNRAS, 341, 1179

Athanassoula, E. 2002, ApJ, 569, L83

Athanassoula, E. 1992, MNRAS, 259, 345

Athanassoula, E., Lambert, J. C., & Dehnen, W. 2005, MNRAS, 363, 496

Athanassoula, E., & Misiriotis, A. 2002, MNRAS, 330, 35

Bahé, Y. M., & McCarthy, I. G. 2015, MNRAS, 447, 969

Bahcall, J. N., Kirhakos, S., Saxe, D. H., & Schneider, D. P. 1997, ApJ, 479, 642

Bai, L., Marcillac, D., Rieke, G. H., et al. 2007, ApJ, 664, 181

Bai, L., Rasmussen, J., Mulchaey, J. S., et al. 2010, ApJ, 713, 637

Bai, L., Rieke, G. H., Rieke, M. J., Christlein, D., & Zabludoff, A. I. 2009, ApJ, 693, 1840

Baldry, I. K., Glazebrook, K., Brinkmann, J., et al. 2004, ApJ, 600, 681

Baldwin, J. A., Phillips, M. M., & Terlevich, R. 1981, PASP, 93, 5

Balogh, M., Eke, V., Miller, C., et al. 2004, MNRAS, 348, 1355

Balogh, M. L., & McGee, S. L. 2010, MNRAS, 402, L59

Balogh, M. L., Morris, S. L., Yee, H. K. C., Carlberg, R. G., & Ellingson, E. 1999, ApJ, 527, 54

Bamford, S. P., Nichol, R. C., Baldry, I. K., et al. 2009, MNRAS, 393, 1324

Barazza, F. D., Jogee, S., & Marinova, I. 2008, ApJ, 675, 1194

Barnes, J. E. 1985, MNRAS, 215, 517

Barnes, J. E. 1989, Nature, 338, 123

Barnes, J. E., & Hernquist, L. E. 1996, ApJ, 471, 115

Barnes, J. E., & Hernquist, L. E. 1992, ARA&A, 30, 705

Barnes, J. E., & Hernquist, L. E. 1991, ApJ, 370, L65

Barro, G., Kriek, M., Pérez-González, P. G., et al. 2016, ApJ, 827, L32

Barton, E., Geller, M., Ramella, M., Marzke, R. O., & da Costa, L. N. 1996, AJ, 112, 871

Barway, S., Wadadekar, Y., & Kembhavi, A. K. 2011, MNRAS, 410, L18

Beers, T. C., Flynn, K., & Gebhardt, K. 1990, AJ, 100, 32

Bekki, K., Couch, W. J., Shioya, Y., & Vazdekis, A. 2005, MNRAS, 359, 949

Bekki, K. 1999, ApJ, 510, L15

Bekki, K., & Couch, W. J. 2011, MNRAS, 415, 1783

Bekki, K., Couch, W. J., & Shioya, Y. 2002, ApJ, 577, 651

Bell, E. F., et al. 2004, ApJ, 608, 752

Benedict, F. G., Smith, B. J., & Kenney, J. D. P. 1996, AJ, 111, 1861

Berentzen, I., Athanassoula, E., Heller, C. H., & Fricke, K. J. 2004, MNRAS, 347, 220

Bernardi, M., et al. 2003, AJ, 125, 1817

Bitsakis, T., Charmandaris, V., da Cunha, E., et al. 2011, A&A, 533, A142

Bitsakis, T., Charmandaris, V., Le Floc'h, E., et al. 2010, A&A, 517, A75

Bitsakis, T., Dultzin, D., Ciesla, L., et al. 2016, MNRAS, 459, 957

Bitsakis, T., Dultzin, D., Ciesla, L., et al. 2015, MNRAS, 450, 3114

Biviano, A., Fadda, D., Durret, F., Edwards, L. O. V., & Marleau, F. 2011, A&A, 532, A77

Blake, C., Pracy, M. B., Couch, W. J., et al. 2004, MNRAS, 355, 713

Blanton, M. R., et al. 2003, AJ, 125, 2348

Blanton, M. R., & Moustakas, J. 2009, ARA&A, 47, 159

Blanton, M. R., & Roweis, S. 2007, AJ, 133, 734

Blanton, M. R., et al. 2005, AJ, 129, 2562

Bolzonella, M., Kovač, K., Pozzetti, L., et al. 2010, A&A, 524, A76

Boselli, A., & Gavazzi, G. 2006, PASP, 118, 517

Bournaud, F., & Combes, F. 2002, A&A, 392, 83

Bournaud, F., Combes, F., & Semelin, B. 2005, MNRAS, 364, L18

Brammer, G. B., Whitaker, K. E., van Dokkum, P. G., et al. 2009, ApJ, 706, L173

Brand, K., Moustakas, J., Armus, L., et al. 2009, ApJ, 693, 340

Brinchmann, J., Charlot, S., White, S. D. M., et al. 2004, MNRAS, 351, 1151

Bruzual, G., & Charlot, S. 2003, MNRAS, 344, 1000

Butcher, H., & Oemler, A., Jr. 1978, ApJ, 219, 18

Byrd, G., & Valtonen, M. 1990, ApJ, 350, 89

Calzetti, D., Armus, L., Bohlin, R. C., et al. 2000, ApJ, 533, 682

Cameron, E., Carollo, C. M., Oesch, P., et al. 2010, MNRAS, 409, 346

Cappellari, M., Bacon, R., Bureau, M., et al. 2006, MNRAS, 366, 1126

Cappellari, M., & Emsellem, E. 2004, PASP, 116, 138

Cardelli, J. A., Clayton, G. C., & Mathis, J. S. 1989, ApJ, 345, 245

Carlberg, R. G., Yee, H. K. C., & Ellingson, E. 1997, ApJ, 478, 462

Carollo, C. M., Stiavelli, M., Seigar, M., de Zeeuw, P. T., & Dejonghe, H. 2002, AJ, 123, 159

Casey, C. M., Narayanan, D., & Cooray, A. 2014, Phys. Rep., 541, 45

Cassarà, L. P., Piovan, L., Weiss, A., Salaris, M., & Chiosi, C. 2013, MNRAS, 436, 2824

Casteels, K. R. V., Bamford, S. P., Skibba, R. A., et al. 2013, MNRAS, 429, 1051

Cervantes Sodi, B. 2017, ApJ, 835, 80

Cervantes Sodi, B., Li, C., & Park, C. 2015, ApJ, 807, 111

Cervantes-Sodi, B., Hernandez, X., Hwang, H. S., Park, C., & Le Borgne, D. 2012, MNRAS, 426, 1606

Cervantes-Sodi, B., Li, C., Park, C., & Wang, L. 2013, ApJ, 775, 19

Chabrier, G. 2003, PASP, 115, 763

Chary, R., & Elbaz, D. 2001, ApJ, 556, 562

Chilingarian, I. V., De Rijcke, S., & Buyle, P. 2009, ApJ, 697, L111

Chincarini, G., Thompson, L. A., & Rood, H. J. 1981, ApJ, 249, L47

Choi, Y.-Y., Han, D.-H., & Kim, S. S. 2010, Journal of Korean Astronomical Society, 43, 191

Choi, Y.-Y., Park, C., & Vogeley, M. S. 2007, ApJ, 658, 884

Choi, Y.-Y., Woo, J.-H., & Park, C. 2009, ApJ, 699, 1679

Chung, S. M., Eisenhardt, P. R., Gonzalez, A. H., et al. 2011, ApJ, 743, 34

Chung, S. M., Gonzalez, A. H., Clowe, D., Markevitch, M., & Zaritsky, D. 2010, ApJ, 725, 1536

Cid Fernandes, R., Stasińska, G., Mateus, A., & Vale Asari, N. 2011, MNRAS, 413, 1687

Cid Fernandes, R., Stasińska, G., Schlickmann, M. S., et al. 2010, MNRAS, 403, 1036

Cluver, M. E., Appleton, P. N., Boulanger, F., et al. 2010, ApJ, 710, 248

Cluver, M. E., Appleton, P. N., Ogle, P., et al. 2013, ApJ, 765, 93

Coelho, P., & Gadotti, D. A. 2011, ApJ, 743, L13

Coenda, V., Muriel, H., & Martínez, H. J. 2012, A&A, 543, A119

Coenda, V., Muriel, H., & Martínez, H. J. 2015, A&A, 573, A96

Cohen, S. A., Hickox, R. C., Wegner, G. A., Einasto, M., & Vennik, J. 2017, ApJ, 835, 56

Combes, F. 2003, Active Galactic Nuclei: From Central Engine to Host Galaxy, 290, 411

Combes, F., & , M. 1985, A&A, 150, 327

Combes, F., & Sanders, R. H. 1981, A&A, 96, 164

Conroy, C., & Gunn, J. E. 2010, ApJ, 712, 833

Conroy, C., Gunn, J. E., & White, M. 2009, ApJ, 699, 486

Couch, W. J., & Sharples, R. M. 1987, MNRAS, 229, 423

Cowie, L. L., & Songaila, A. 1977, Nature, 266, 501

Coziol, R., & Plauchu-Frayn, I. 2007, AJ, 133, 2630

Coziol, R., Ribeiro, A. L. B., de Carvalho, R. R., & Capelato, H. V. 1998a, ApJ, 493, 563

Coziol, R., de Carvalho, R. R., Capelato, H. V., & Ribeiro, A. L. B. 1998b, ApJ, 506, 545

Cucciati, O., Iovino, A., Kovač, K., et al. 2010, A&A, 524, A2

Díaz-Giménez, E., Mamon, G. A., Pacheco, M., Mendes de Oliveira, C., & Alonso, M. V. 2012, MNRAS, 426, 296

Díaz-Giménez, E., & Zandivarez, A. 2015, A&A, 578, A61

da Cunha, E., Charlot, S., & Elbaz, D. 2008, MNRAS, 388, 1595

da Silva, R. L., Prochaska, J. X., Rosario, D., Tumlinson, J., & Tripp, T. M. 2011, ApJ, 735, 54

Daddi, E., Alexander, D. M., Dickinson, M., et al. 2007, ApJ, 670, 173

Das, M., Teuben, P. J., Vogel, S. N., Regan, M. W., Sheth, K., Harris, A. I., & Jefferys, W. H. 2003, ApJ, 582, 190

de Carvalho, R. R., Gonçalves, T. S., Iovino, A., et al. 2005, AJ, 130, 425

de Carvalho, R. R., Ribeiro, A. L. B., & Zepf, S. E. 1994, ApJS, 93, 47

de la Rosa, I. G., de Carvalho, R. R., Vazdekis, A., & Barbuy, B. 2007, AJ, 133, 330

de Lorenzo-Cáceres, A., Falcón-Barroso, J., Vazdekis, A., & Martínez-Valpuesta, I. 2008, ApJ, 684, L83

De Lucia, G., Fontanot, F., & Wilman, D. 2012, MNRAS, 419, 1324

De Robertis, M. M., Yee, H. K. C., & Hayhoe, K. 1998, ApJ, 496, 93

de Vaucouleurs, G., de Vaucouleurs, A., Corwin, H. G., Jr., Buta, R. J., Paturel, G., & Fouqué, P. 1991, Third Reference Catalog of Bright Galaxies (Berlin: Springer)

Debuhr, J., Quataert, E., & Ma, C.-P. 2011, MNRAS, 412, 1341

Desjardins, T. D., Gallagher, S. C., Hornschemeier, A. E., et al. 2014, ApJ, 790, 132

Desjardins, T. D., Gallagher, S. C., Tzanavaris, P., et al. 2013, ApJ, 763, 121

Devereux, N. 1987, ApJ, 323, 91

Di Matteo, T., Johnstone, R. M., Allen, S. W., & Fabian, A. C. 2001, ApJ, 550, L19

Di Matteo, T., Springel, V., & Hernquist, L. 2005, Nature, 433, 604

Diaferio, A. 1999, MNRAS, 309, 610

Diaferio, A., & Geller, M. J. 1997, ApJ, 481, 633

Diaferio, A., Geller, M. J., & Ramella, M. 1994, AJ, 107, 868

Dixon, K. L., Godwin, J. G., & Peach, J. V. 1989, MNRAS, 239, 459

Donoso, E., Yan, L., Tsai, C., et al. 2012, ApJ, 748, 80

Dressler, A. 1980, ApJ, 236, 351

Dressler, A., & Gunn, J. E. 1983, ApJ, 270, 7

Dressler, A., Oemler, A., Jr., Couch, W. J., et al. 1997, ApJ, 490, 577

Dressler, A., Smail, I., Poggianti, B. M., et al. 1999, ApJS, 122, 51

Duc, P.-A., Poggianti, B. M., Fadda, D., et al. 2002, A&A, 382, 60

Einasto, M., Lietzen, H., Tempel, E., et al. 2014, A&A, 562, A87

Elbaz, D., Dickinson, M., Hwang, H. S., et al. 2011, A&A, 533, A119

Elmegreen, B. G. 2005, in Island Universe: Structure and Evolution of Disk Galaxies, ed. R. S. de Jong (Springer), 163

Emsellem, E., Greusard, D., Combes, F., Friedli, D., Leon, S., Pécontal, E., & Wozniak, H. 2001, A&A, 368, 52

Emsellem, E., Fathi, K., Wozniak, H., Ferruit, P., Mundell, C. G., & Schinnerer, E. 2006, MNRAS, 365, 367

Englmaier, P., & Shlosman, I. 2004, ApJ, 617, L115

Erwin, P., & Sparke, L. S. 2002, AJ, 124, 65

Eskridge, P. B., Frogel, J. A., Pogge, R. W., et al. 2000, AJ, 119, 536

Faber, S. M., Willmer, C. N. A., Wolf, C., et al. 2007, ApJ, 665, 265

Falco, E. E., Kurtz, M. J., Geller, M. J., et al. 1999, PASP, 111, 438

Ferrarese, L., & Merritt, D. 2000, ApJ, 539, L9

Ferrari, C., Benoist, C., Maurogordato, S., Cappi, A., & Slezak, E. 2005, A&A, 430, 19

Finn, R. A., Zaritsky, D., McCarthy, D. W., Jr., et al. 2005, ApJ, 630, 206

French, K. D., Yang, Y., Zabludoff, A., et al. 2015, ApJ, 801, 1

Friedli, D., & Benz, W. 1993, A&A, 268, 65

Friedli, D., Wozniak, H., Rieke, M., Martinet, L., & Bratschi, P. 1996, A&AS, 118, 461

Fuentes-Williams, T., & Stocke, J. T. 1988, AJ, 96, 1235

Fujita, Y. 2004, PASJ, 56, 29

Gómez, P. L., Nichol, R. C., Miller, C. J., et al. 2003, ApJ, 584, 210

Gültekin, K., Richstone, D. O., Gebhardt, K., et al. 2009a, ApJ, 695, 1577

Gültekin, K., Richstone, D. O., Gebhardt, K., et al. 2009b, ApJ, 698, 198

Gallagher, S. C., Durrell, P. R., Elmegreen, D. M., et al. 2010, AJ, 139, 545

Garcia-Burillo, S., Sempere, M. J., Combes, F., & Neri, R. 1998, A&A, 333, 864

Geach, J. E., Smail, I., Ellis, R. S., et al. 2006, ApJ, 649, 661

Gebhardt, K., Bender, R., Bower, G., et al. 2000, ApJ, 539, L13

Geller, M. J., & Huchra, J. P. 1989, Science, 246, 897

George, M. R., Ma, C.-P., Bundy, K., et al. 2013, ApJ, 770, 113

Gerin, M., Combes, F., & Athanassoula, E. 1990, A&A, 230, 37

Giovannini, G., Cotton, W. D., Feretti, L., Lara, L., & Venturi, T. 1998, ApJ, 493, 632

Goto, T. 2005, MNRAS, 356, L6

Goto, T., Yagi, M., & Yamauchi, C. 2008, MNRAS, 391, 700

Graham, A. W., & Li, I.-h. 2009, ApJ, 698, 812

Graham, A. W., Onken, C. A., Athanassoula, E., & Combes, F. 2011, MNRAS, 412, 2211

Graves, G. J., & Schiavon, R. P. 2008, ApJS, 177, 446-464

Gregory, S. A., & Thompson, L. A. 1984, ApJ, 286, 422

Greusard, D., Friedli, D., Wozniak, H., Martinet, L., & Martin, P. 2000, A&AS, 145, 425

Gunn, J. E., & Gott, J. R., III 1972, ApJ, 176, 1

Haines, C. P., Busarello, G., Merluzzi, P., et al. 2011, MNRAS, 412, 127

Haines, C. P., Gargiulo, A., La Barbera, F., et al. 2007, MNRAS, 381, 7

Hao, L., Jogee, S., Barazza, F. D., Marinova, I., & Shen, J. 2009, Galaxy Evolution: Emerging Insights and Future Challenges, 419, 402

Hasan, H., & Norman, C. 1990, ApJ, 361, 69

Hasan, H., Pfenniger, D., & Norman, C. 1993, ApJ, 409, 91

Hawarden, T. G., Mountain, C. M., Leggett, S. K., & Puxley, P. J. 1986, MNRAS, 221, 41P

Heckman, T. M. 1980, A&A, 88, 365

Heller, C. H., & Shlosman, I. 1994, ApJ, 424, 84

Hernquist, L. 1989, Nature, 340, 687

Hess, K. M., & Wilcots, E. M. 2013, AJ, 146, 124

Hickson, P. 1982, ApJ, 255, 382

Hickson, P., Mendes de Oliveira, C., Huchra, J. P., & Palumbo, G. G. 1992, ApJ, 399, 353

Hill, J. M., & Oegerle, W. R. 1998, AJ, 116, 1529

Hill, J. M., & Oegerle, W. R. 1993, AJ, 106, 831

Ho, L. C., Filippenko, A. V., & Sargent, W. L. W. 1997, ApJ, 487, 591

Hohl, F. 1971, ApJ, 168, 343

Hopkins, P. F., Cox, T. J., Dutta, S. N., et al. 2009, ApJS, 181, 135

Hopkins, P. F., Hernquist, L., Cox, T. J., Di Matteo, T., Robertson, B., & Springel, V. 2006, ApJS, 163, 1

Hopkins, P. F., Hernquist, L., Cox, T. J., Dutta, S. N., & Rothberg, B. 2008, ApJ, 679, 156

Hopkins, P. F., & Quataert, E. 2010, MNRAS, 407, 1529

Huang, J. H., Gu, Q. S., Su, H. J., Hawarden, T. G., Liao, X. H., & Wu, G. X. 1996, A&A, 313, 13

Hubble, E., & Humason, M. L. 1931, ApJ, 74, 43

Huchra, J., Davis, M., Latham, D., & Tonry, J. 1983, ApJS, 52, 89

Hunsberger, S. D., Charlton, J. C., & Zaritsky, D. 1996, ApJ, 462, 50

Hunt, L. K., et al. 2008, A&A, 482, 133

Hunt, L. K., & Malkan, M. A. 1999, ApJ, 516, 660

Husemann, B., Kamann, S., Sandin, C., et al. 2012, A&A, 545, A137

Hwang, H. S., Elbaz, D., Lee, J. C., et al. 2010, A&A, 522, A33

Hwang, H. S., Geller, M. J., Diaferio, A., & Rines, K. J. 2012a, ApJ, 752, 64

Hwang, H. S., Geller, M. J., Kurtz, M. J., Dell'Antonio, I. P., & Fabricant, D. G. 2012b, ApJ, 758, 25

Hwang, H. S., Park, C., Elbaz, D., & Choi, Y.-Y. 2012c, A&A, 538, A15

Hwang, H. S., & Lee, M. G. 2009, MNRAS, 397, 2111

Hwang, H. S., & Park, C. 2009, ApJ, 700, 791

Ilbert, O., Arnouts, S., McCracken, H. J., et al. 2006, A&A, 457, 841

Iovino, A., de Carvalho, R. R., Gal, R. R., et al. 2003, AJ, 125, 1660

Jenkins, L. P., Hornschemeier, A. E., Mobasher, B., Alexander, D. M., & Bauer, F. E. 2007, ApJ, 666, 846

Jogee, S. 2006, Physics of Active Galactic Nuclei at all Scales, 693, 143

Jogee, S., Scoville, N., & Kenney, J. D. P. 2005, ApJ, 630, 837

Johnson, K. E., Hibbard, J. E., Gallagher, S. C., et al. 2007, AJ, 134, 1522

Johnston-Hollitt, M., Sato, M., Gill, J. A., Fleenor, M. C., & Brick, A.-M. 2008, MNRAS, 390, 289

Johnstone, R. M., Allen, S. W., Fabian, A. C., & Sanders, J. S. 2002, MNRAS, 336, 299

Jungwiert, B., Combes, F., & Axon, D. J. 1997, A&AS, 125, 479

Kauffmann, G., Heckman, T. M., White, S. D. M., et al. 2003a, MNRAS, 341, 33

Kauffmann, G., et al. 2003b, MNRAS, 346, 1055

Kawano, N., Ohto, A., & Fukazawa, Y. 2003, PASJ, 55, 585

Kawata, D., & Mulchaey, J. S. 2008, ApJ, 672, L103

Kelson, D. D., Zabludoff, A. I., Williams, K. A., et al. 2002, ApJ, 576, 720

Kennicutt, R. C., Jr. 1998, ARA&A, 36, 189

Kewley, L. J., Dopita, M. A., Sutherland, R. S., Heisler, C. A., & Trevena, J. 2001, ApJ, 556, 121

Kewley, L. J., Groves, B., Kauffmann, G., & Heckman, T. 2006, MNRAS, 372, 961

Kim, W.-T., & Elmegreen, B. G. 2017, ApJ, 841, L4

Knapen, J. H., Pérez-Ramírez, D., & Laine, S. 2002, MNRAS, 337, 808

Knapen, J. H., Shlosman, I., & Peletier, R. F. 2000, ApJ, 529, 93

Ko, J., Chung, H., Hwang, H. S., & Lee, J. C. 2016, ApJ, 820, 132

Ko, J., Hwang, H. S., Im, M., et al. 2014, ApJ, 791, 134

Ko, J., Hwang, H. S., Lee, J. C., & Sohn, Y.-J. 2013, ApJ, 767, 90

Ko, J., Im, M., Lee, H. M., et al. 2012, ApJ, 745, 181

Ko, J., Im, M., Lee, H. M., et al. 2009, ApJ, 695, L198

Komatsu, E., et al. 2009, ApJS, 180, 330

Konstantopoulos, I. S., Gallagher, S. C., Fedotov, K., et al. 2012, ApJ, 745, 30

Kormendy, J., & Kennicutt, R. C., Jr. 2004, ARA&A, 42, 603

Koyama, Y., Kodama, T., Nakata, F., Shimasaku, K., & Okamura, S. 2011, ApJ, 734, 66

Koyama, Y., Kodama, T., Shimasaku, K., et al. 2010, MNRAS, 403, 1611

Kranz, W. D., Tran, K.-V. H., Giordano, L., & Saintonge, A. 2010, AJ, 140, 561

Kroupa, P. 2015, Canadian Journal of Physics, 93, 169

Kuutma, T., Tamm, A., & Tempel, E. 2017, A&A, 600, L6

Lachieze-Rey, M., Vigroux, L., & Souviron, J. 1985, A&A, 150, 62

Laine, S., Shlosman, I., Knapen, J. H., & Peletier, R. F. 2002, ApJ, 567, 97

Larson, R. B., Tinsley, B. M., & Caldwell, C. N. 1980, ApJ, 237, 692

Lauer, T. R. 1986, ApJ, 311, 34

Laurikainen, E., Salo, H., Buta, R., & Knapen, J. H. 2007, MNRAS, 381, 401

Laurikainen, E., Salo, H., & Buta, R. 2004, ApJ, 607, 103

Lee, B. C., Allam, S. S., Tucker, D. L., et al. 2004, AJ, 127, 1811

Lee, G.-H., Hwang, H. S., Lee, M. G., et al. 2015, ApJ, 800, 80

Lee, G.-H., Hwang, H. S., Sohn, J., & Lee, M. G. 2017, ApJ, 835, 280

Lee, G.-H., Park, C., Lee, M. G., & Choi, Y.-Y. 2012a, ApJ, 745, 125

Lee, G.-H., Woo, J.-H., Lee, M. G., et al. 2012b, ApJ, 750, 141

Lee, J. C. 2012, Publication of Korean Astronomical Society, 27, 291

Lee, J. C., Hwang, H. S., Lee, M. G., Kim, M., & Lee, J. H. 2012, ApJ, 756, 95

Lee, J. C., Hwang, H. S., & Ko, J. 2013, ApJ, 774, 62

Lee, J. C., Hwang, H. S., & Lee, G.-H. 2016, ApJ, 833, 188

Lee, M. G., Lee, H. M., Im, M., et al. 2009, AKARI, a Light to Illuminate the Misty
    Universe, 418, 241

Lemaux, B. C., Gal, R. R., Lubin, L. M., et al. 2012, ApJ, 745, 106

Lenkić, L., Tzanavaris, P., Gallagher, S. C., et al. 2016, MNRAS, 459, 2948

Leonardi, A. J., & Rose, J. A. 1996, AJ, 111, 182

Lewis, I., Balogh, M., De Propris, R., et al. 2002, MNRAS, 334, 673

Li, C., Gadotti, D. A., Mao, S., & Kauffmann, G. 2009, MNRAS, 397, 726

Lin, Y., Cervantes Sodi, B., Li, C., Wang, L., & Wang, E. 2014, ApJ, 796, 98

Łokas, E. L., Ebrová, I., del Pino, A., et al. 2016, ApJ, 826, 227

Lynden-Bell, D. 1979, MNRAS, 187, 101

Márquez, I., et al. 2000, A&A, 360, 431

Méndez-Abreu, J., Sánchez-Janssen, R., & Aguerri, J. A. L. 2010, ApJ, 711, L61

Maciejewski, W., & Athanassoula, E. 2008, MNRAS, 389, 545

Maciejewski, W., & Sparke, L. S. 1997, ApJ, 484, L117

Maciejewski, W., Teuben, P. J., Sparke, L. S., & Stone, J. M. 2002, MNRAS, 329, 502

Mahajan, S. 2013, MNRAS, 431, L117

Mahajan, S., Haines, C. P., & Raychaudhury, S. 2011, MNRAS, 412, 1098

Mahajan, S., Haines, C. P., & Raychaudhury, S. 2010, MNRAS, 404, 1745

Mahdavi, A., Böhringer, H., Geller, M. J., & Ramella, M. 2000, ApJ, 534, 114

Malkan, M. A., Gorjian, V., & Tam, R. 1998, ApJS, 117, 25

Mamon, G. A. 1987, ApJ, 321, 622

Marinova, I., & Jogee, S. 2007, ApJ, 659, 1176

Markevitch, M., Vikhlinin, A., Forman, W. R., & Sarazin, C. L. 1999, ApJ, 527, 545

Mateos, S., Alonso-Herrero, A., Carrera, F. J., et al. 2012, MNRAS, 426, 3271

Martínez, M. A., Del Olmo, A., Coziol, R., & Perea, J. 2010, AJ, 139, 1199

Martínez, H. J., Zandivarez, A., Domínguez, M., Merchán, M. E., & Lambas, D. G. 2002, MNRAS, 333, L31

Martinet, L., & Friedli, D. 1997, A&A, 323, 363

Martini, P., & Pogge, R. W. 1999, AJ, 118, 2646

Martini, P., Regan, M. W., Mulchaey, J. S., & Pogge, R. W. 2003, ApJ, 589, 774

Masters, K. L., et al. 2011, MNRAS, 411, 2026

Masters, K. L., Mosleh, M., Romer, A. K., et al. 2010, MNRAS, 405, 783

McConnachie, A. W., Patton, D. R., Ellison, S. L., & Simard, L. 2009, MNRAS, 395, 255

McConnell, N. J., Ma, C.-P., Gebhardt, K., et al. 2011, Nature, 480, 215

McLeod, K. K., & Rieke, G. H. 1995, ApJ, 441, 96

Mendel, J. T., Ellison, S. L., Simard, L., Patton, D. R., & McConnachie, A. W. 2011, MNRAS, 418, 1409

Mendes de Oliveira, C., Coelho, P., González, J. J., & Barbuy, B. 2005, AJ, 130, 55

Mendes de Oliveira, C., & Hickson, P. 1994, ApJ, 427, 684

Mihos, J. C., & Hernquist, L. 1996, ApJ, 464, 641

Miller, N. A. 2005, AJ, 130, 2541

Miller, C. J., Nichol, R. C., Reichart, D., et al. 2005, AJ, 130, 968

Miller, C. J., Nichol, R. C., Gómez, P. L., Hopkins, A. M., & Bernardi, M. 2003, ApJ, 597, 142

Minkowski, R. 1961, AJ, 66, 558

Mohr, J. J., Evrard, A. E., Fabricant, D. G., & Geller, M. J. 1995, ApJ, 447, 8

Moles, M., Marquez, I., & Perez, E. 1995, ApJ, 438, 604

Moore, B., Katz, N., Lake, G., Dressler, A., & Oemler, A. 1996, Nature, 379, 613

Mulchaey, J. S., & Regan, M. W. 1997, ApJ, 482, L135

Muldrew, S. I., Croton, D. J., Skibba, R. A., et al. 2012, MNRAS, 419, 2670

Muratov, A. L., & Gnedin, O. Y. 2010, ApJ, 718, 1266

Nair, P. B., & Abraham, R. G. 2010a, ApJS, 186, 427

Nair, P. B., & Abraham, R. G. 2010b, ApJ, 714, L260

Newberry, M. V., Boroson, T. A., & Kirshner, R. P. 1990, ApJ, 350, 585

Noeske, K. G., Weiner, B. J., Faber, S. M., et al. 2007, ApJ, 660, L43

Noguchi, M. 1988, A&A, 203, 259

Noguchi, M. 1987, MNRAS, 228, 635

Norman, C. A., Sellwood, J. A., & Hasan, H. 1996, ApJ, 462, 114

Norton, S. A., Gebhardt, K., Zabludoff, A. I., & Zaritsky, D. 2001, ApJ, 557, 150

Nulsen, P. E. J. 1982, MNRAS, 198, 1007

Oemler, A., Jr. 1974, ApJ, 194, 1

Oh, K., Sarzi, M., Schawinski, K., & Yi, S. K. 2011, ApJS, 195, 13

Osterbrock, D. E. & Ferland, G. J. 2006, Astrophysics of gaseous nebulae and active galactic nuclei, 2nd edn. University Science Books, Mill Valley, CA

Ostriker, J. P., & Peebles, P. J. E. 1973, ApJ, 186, 467

Owen, F. N., Ledlow, M. J., Keel, W. C., Wang, Q. D., & Morrison, G. E. 2005, AJ, 129, 31

Pan, Z., Kong, X., & Fan, L. 2013, ApJ, 776, 14

Park, C., & Choi, Y.-Y. 2009, ApJ, 691, 1828

Park, C., & Choi, Y.-Y. 2005, ApJ, 635, L29

Park, C., Gott, J. R., III, & Choi, Y.-Y. 2008, ApJ, 674, 784

Park, C., Choi, Y.-Y., Vogeley, M. S., et al. 2007, ApJ, 658, 898

Park, C., & Hwang, H. S. 2009, ApJ, 699, 1595

Peng, Y., Maiolino, R., & Cochrane, R. 2015, Nature, 521, 192

Peng, Y.-j., Lilly, S. J., Kovač, K., et al. 2010a, ApJ, 721, 193

Peng, C. Y., Ho, L. C., Impey, C. D., & Rix, H.-W. 2010b, AJ, 139, 2097

Pfenniger, D. 1984, A&A, 134, 373

Pfenniger, D., & Friedli, D. 1991, A&A, 252, 75

Pfenniger, D., & Norman, C. 1990, ApJ, 363, 391

Plauchu-Frayn, I., & Coziol, R. 2010, AJ, 140, 612

Plauchu-Frayn, I., Del Olmo, A., Coziol, R., & Torres-Papaqui, J. P. 2012, A&A, 546, A48

Piovan, L., Tantalo, R., & Chiosi, C. 2003, A&A, 408, 559

Pogge, R. W., & Martini, P. 2002, ApJ, 569, 624

Poggianti, B. M., Aragón-Salamanca, A., Zaritsky, D., et al. 2009, ApJ, 693, 112

Poggianti, B. M., Desai, V., Finn, R., et al. 2008, ApJ, 684, 888

Poggianti, B. M., von der Linden, A., De Lucia, G., et al. 2006, ApJ, 642, 188

Poggianti, B. M., Bridges, T. J., Komiyama, Y., et al. 2004, ApJ, 601, 197

Poggianti, B. M., Smail, I., Dressler, A., et al. 1999, ApJ, 518, 576

Polletta, M., Tajer, M., Maraschi, L., et al. 2007, ApJ, 663, 81

Pompei, E., & Iovino, A. 2012, A&A, 539, A106

Popesso, P., Biviano, A., Rodighiero, G., et al. 2012, A&A, 537, A58

Postman, M., & Geller, M. J. 1984, ApJ, 281, 95

Pracy, M. B., Croom, S., Sadler, E., et al. 2013, MNRAS, 432, 3131

Pracy, M. B., Owers, M. S., Couch, W. J., et al. 2012, MNRAS, 420, 2232

Pracy, M. B., Kuntschner, H., Couch, W. J., et al. 2009, MNRAS, 396, 1349

Pracy, M. B., Couch, W. J., Blake, C., et al. 2005, MNRAS, 359, 1421

Prandoni, I., Iovino, A., & MacGillivray, H. T. 1994, AJ, 107, 1235

Proctor, R. N., Forbes, D. A., Hau, G. K. T., et al. 2004, MNRAS, 349, 1381

Quilis, V., Moore, B., & Bower, R. 2000, Science, 288, 1617

Quillen, A. C., Frogel, J. A., Kenney, J. D. P., Pogge, R. W., & Depoy, D. L. 1995, ApJ, 441, 549

Ramella, M., Diaferio, A., Geller, M. J., & Huchra, J. P. 1994, AJ, 107, 1623

Rasmussen, J., Mulchaey, J. S., Bai, L., et al. 2012, ApJ, 757, 122

Reese, A. S., Williams, T. B., Sellwood, J. A., Barnes, E. I., & Powell, B. A. 2007, AJ, 133, 2846

Regan, M. W., & Mulchaey, J. S. 1999, AJ, 117, 2676

Regan, M. W., & Teuben, P. J. 2004, ApJ, 600, 595

Regan, M. W., Vogel, S. N., & Teuben, P. J. 1997, ApJ, 482, L143

Ribeiro, A. L. B., de Carvalho, R. R., Capelato, H. V., & Zepf, S. E. 1998, ApJ, 497, 72

Rines, K., Geller, M. J., Diaferio, A., & Kurtz, M. J. 2013, ApJ, 767, 15

Rines, K., Geller, M. J., Diaferio, A., et al. 2002, AJ, 124, 1266

Rines, K., Mahdavi, A., Geller, M. J., et al. 2001, ApJ, 555, 558

Rines, K., & Diaferio, A. 2010, AJ, 139, 580

Rines, K., & Diaferio, A. 2006, AJ, 132, 1275

Rines, K., & Geller, M. J. 2008, AJ, 135, 1837

Roberts, W. W., Jr., Huntley, J. M., & van Albada, G. D. 1979, ApJ, 233, 67

Rodrigue, M., Schultz, A., Thompson, J., et al. 1995, AJ, 109, 2362

Romano-Díaz, E., Shlosman, I., Heller, C., & Hoffman, Y. 2008, ApJ, 687, L13

Rood, H. J. 1976, ApJ, 207, 16

Rood, H. J., & Struble, M. F. 1994, PASP, 106, 413

Rubin, V. C., Hunter, D. A., & Ford, W. K., Jr. 1990, ApJ, 365, 86

Sakamoto, K., Okumura, S. K., Ishizuki, S., & Scoville, N. Z. 1999, ApJ, 525, 691

Salpeter, E. E. 1955, ApJ, 121, 161

Sandage, A., & Tamman, G. A. 1981, A Revised Shapley-Ames Catalog of Bright
    Galaxies (Washington, DC: Carnegie Inst.)

Sanders, D. B., Soifer, B. T., Elias, J. H., Madore, B. F., Matthews, K., Neugebauer,
    G., & Scoville, N. Z. 1988, ApJ, 325, 74

Schawinski, K., Urry, C. M., Simmons, B. D., et al. 2014, MNRAS, 440, 889

Schinnerer, E., Böker, T., Emsellem, E., & Lisenfeld, U. 2006, ApJ, 649, 181

Schlegel, D. J., Finkbeiner, D. P., & Davis, M. 1998, ApJ, 500, 525

Schmitt, H. R. 2001, AJ, 122, 2243

Schiavon, R. P. 2007, ApJS, 171, 146

Sellwood, J. A. 1981, A&A, 99, 362

Sellwood, J. A., & Wilkinson, A. 1993, Reports on Progress in Physics, 56, 173

Seo, W.-Y., & Kim, W.-T. 2014, ApJ, 792, 47

Seo, W.-Y., & Kim, W.-T. 2013, ApJ, 769, 100

Serra, A. L., Diaferio, A., Murante, G., & Borgani, S. 2011, MNRAS, 412, 800

Shaw, M., Axon, D., Probst, R., & Gatley, I. 1995, MNRAS, 274, 369

Shen, J., & Debattista, V. P. 2011, Memorie della Societa Astronomica Italiana
    Supplementi, 18, 169

Shen, J., & Debattista, V. P. 2009, ApJ, 690, 758

Shen, J., & Sellwood, J. A. 2004, ApJ, 604, 614

Sheth, K., Elmegreen, D. M., Elmegreen, B. G., et al. 2008, ApJ, 675, 1141

Sheth, K., Vogel, S. N., Regan, M. W., Thornley, M. D., & Teuben, P. J. 2005, ApJ, 632, 217

Shim, H., Im, M., Lee, H. M., et al. 2011, ApJ, 727, 14

Shim, J., Lee, J., & Hoyle, F. 2015, ApJ, 815, 107

Shimada, M., Ohyama, Y., Nishiura, S., Murayama, T., & Taniguchi, Y. 2000, AJ, 119, 2664

Shlosman, I., Frank, J., & Begelman, M. C. 1989, Nature, 338, 45

Silverman, J. D., Kovač, K., Knobel, C., et al. 2009, ApJ, 695, 171

Skibba, R. A., Bamford, S. P., Nichol, R. C., et al. 2009, MNRAS, 399, 966

Slinglend, K., Batuski, D., Miller, C., et al. 1998, ApJS, 115, 1

Snyder, G. F., Cox, T. J., Hayward, C. C., Hernquist, L., & Jonsson, P. 2011, ApJ, 741, 77

Sobral, D., Best, P. N., Smail, I., et al. 2011, MNRAS, 411, 675

Sohn, J., Geller, M. J., Hwang, H. S., Zahid, H. J., & Lee, M. G. 2016, ApJS, 225, 23

Sohn, J., Hwang, H. S., Geller, M. J., et al. 2015, Journal of Korean Astronomical Society, 48, 381

Sohn, J., Hwang, H. S., Lee, M. G., Lee, G.-H., & Lee, J. C. 2013, ApJ, 771, 106

Spitzer, L., Jr., & Baade, W. 1951, ApJ, 113, 413

Springel, V., Di Matteo, T., & Hernquist, L. 2005, ApJ, 620, L79

Strateva, I., Ivezić, Ž., Knapp, G. R., et al. 2001, AJ, 122, 1861

Swinbank, A. M., Balogh, M. L., Bower, R. G., et al. 2012, MNRAS, 420, 672

Swinbank, A. M., Balogh, M. L., Bower, R. G., et al. 2005, ApJ, 622, 260

Tanaka, M., Goto, T., Okamura, S., Shimasaku, K., & Brinkmann, J. 2004, AJ, 128, 2677

Tasca, L. A. M., Kneib, J.-P., Iovino, A., et al. 2009, A&A, 503, 379

Tegmark, M., Blanton, M. R., Strauss, M. A., et al. 2004, ApJ, 606, 702

Temi, P., Mathews, W. G., & Brighenti, F. 2005, ApJ, 622, 235

Tempel, E., Stoica, R. S., Martínez, V. J., et al. 2014, MNRAS, 438, 3465

Thakur, P., Ann, H. B., & Jiang, I.-G. 2009, ApJ, 693, 586

Thompson, L. A. 1981, ApJ, 244, L43

Tinker, J. L., Leauthaud, A., Bundy, K., et al. 2013, ApJ, 778, 93

Tran, K.-V. H., Franx, M., Illingworth, G. D., et al. 2004, ApJ, 609, 683

Tran, K.-V. H., Simard, L., Zabludoff, A. I., & Mulchaey, J. S. 2001, ApJ, 549, 172

Tremaine, S., Gebhardt, K., Bender, R., et al. 2002, ApJ, 574, 740

Tremonti, C. A., et al. 2004, ApJ, 613, 898

Tzanavaris, P., Gallagher, S. C., Hornschemeier, A. E., et al. 2014, ApJS, 212, 9

Tzanavaris, P., Hornschemeier, A. E., Gallagher, S. C., et al. 2010, ApJ, 716, 556

Tremonti, C. A., et al. 2004, ApJ, 613, 898

van Albada, G. D., & Roberts, W. W., Jr. 1981, ApJ, 246, 740

van den Bergh, S. 2002, AJ, 124, 782

Vazdekis, A., Sánchez-Blázquez, P., Falcón-Barroso, J., et al. 2010, MNRAS, 404, 1639

Verdes-Montenegro, L., Yun, M. S., Williams, B. A., et al. 2001, A&A, 377, 812

Veilleux, S., & Osterbrock, D. E. 1987, ApJS, 63, 295

Villaume, A., Conroy, C., & Johnson, B. D. 2015, ApJ, 806, 82

Voges, W., Aschenbach, B., Boller, T., et al. 1999, A&A, 349, 389

Vogt, F. P. A., Dopita, M. A., Borthakur, S., et al. 2015, MNRAS, 450, 2593

Walker, L. M., Butterfield, N., Johnson, K., et al. 2013, ApJ, 775, 129

Walker, L. M., Johnson, K. E., Gallagher, S. C., et al. 2012, AJ, 143, 69

Walker, L. M., Johnson, K. E., Gallagher, S. C., et al. 2010, AJ, 140, 1254

Wegner, G., Colless, M., Baggley, G., et al. 1996, ApJS, 106, 1

Wegner, G., Colless, M., Saglia, R. P., et al. 1999, MNRAS, 305, 259

Weinmann, S. M., van den Bosch, F. C., Yang, X., & Mo, H. J. 2006, MNRAS, 366, 2

Wetzel, A. R., Tinker, J. L., Conroy, C., & van den Bosch, F. C. 2013, MNRAS, 432, 336

Wilman, D. J., Pierini, D., Tyler, K., et al. 2008, ApJ, 680, 1009

Wilman, D. J., Balogh, M. L., Bower, R. G., et al. 2005, MNRAS, 358, 71

Woo, J.-H., Treu, T., Barth, A. J., et al. 2010, ApJ, 716, 269

Worthey, G., & Ottaviani, D. L. 1997, ApJS, 111, 377

Wozniak, H., Friedli, D., Martinet, L., Martin, P., & Bratschi, P. 1995, A&AS, 111, 115

Wright, E. L., Eisenhardt, P. R. M., Mainzer, A. K., et al. 2010, AJ, 140, 1868

Wyder, T. K., Martin, D. C., Schiminovich, D., et al. 2007, ApJS, 173, 293

Yagi, M., & Goto, T. 2006, AJ, 131, 2050

Yagi, M., Komiyama, Y., Yoshida, M., et al. 2007, ApJ, 660, 1209

Yang, Y., Zabludoff, A. I., Zaritsky, D., & Mihos, J. C. 2008, ApJ, 688, 945-971

Yang, Y., Zabludoff, A. I., Zaritsky, D., Lauer, T. R., & Mihos, J. C. 2004, ApJ, 607, 258

York, D. G., et al. 2000, AJ, 120, 1579

Yun, M. S., Verdes-Montenegro, L., del Olmo, A., & Perea, J. 1997, ApJ, 475, L21

Zabludoff, A. I., Zaritsky, D., Lin, H., et al. 1996, ApJ, 466, 104

Zabludoff, A. I., & Mulchaey, J. S. 1998, ApJ, 496, 39

Zucker, C., Walker, L. M., Johnson, K., et al. 2016, ApJ, 821, 113

요　　약

　　은하의 형태와 물리적인 특성들은 은하가 속한 환경에 따라 달라진다. 그러므로 은하의 진화를 이해하기 위해서는 은하에 작용하는 환경 효과에 대한 이해가 동반되어야 한다. 본 학위논문은 다양한 환경에 위치하는 은하들의 다파장($0.2 - 25\ \mu$m) 특성과 환경 효과에 대한 네 편의 연구들로 구성되어 있다.

　　2장에서 우리는 SDSS와 *WISE* 자료를 이용한 Abell 2199 초은하단에 관한 연구 결과를 이야기한다. Abell 2199 초은하단은 여러 은하단과 은하군이 모여있는, 가까운 우주($z \sim 0.03$)에서 가장 무거운 은하 구조이다. 우리는 Abell 2199 초은하단에 소속된 은하들의 중적외선(MIR) 색지수-광도 분포로부터, 은하의 중간 진화 단계에 해당하는 MIR Green Valley(MGV)를 정의하였다. MGV에 있는 은하들은 가시광 색등급도에서는 Red Sequence에 위치한다. MGV 은하들은 Red Sequence에 함께 위치하는 MIR Blue 은하들과 비슷한 D_n4000과 별형성률(Star Formation Rates)를 갖는다. 항성 종족 모형(stellar population model)이 예측하는 MGV 은하에 속한 별들의 평균 나이는 10–100억년으로, MIR Blue 은하들(> 100억년)보다 상대적으로 젊다. 이러한 결과들은 은하가 별형성 활동이 거의 완전히 멈춘 뒤에 MGV로 진입하며, MGV에서 수십억년의 시간을 보낸 뒤에 MIR Blue 은하로 진화한다는 것을 말해준다. 은하의 형태를 살펴보았을 때, MGV에는 조기형 은하와 만기형 은하가 비슷한 비율로 존재한다. MGV 조기형 은하는 MGV 만기형 은하보다 고밀도 환경(은하단/은하군의 중심부)에 집중되어 있다. 이는 은하단과 은하군 중심부 환경이 MGV 만기형 은하에서 MIR 조기형 은하로의 형태 변화에 영향을 주었음을 의미하는 관측적인 증거이다. MGV 만기형 은하가 매우 낮은 별형성 활동을 보임에도 불구하고 그 형태를 유지하고 있다는 것은 MGV 만기형 은하의 별형성률 변화에 미치는 환경 효과가 긴 시간에 걸쳐 천천히 작용했다는 것을 말해준다. 그러므로 MGV 만기형 은하를 형성하는데 기여한 환경 효과는 Strangulation 혹은 Starvation일 가능성이 높다. 반면, MGV 만기형 은하에서 MGV 조기형 은하로의 형태 변화는 은하단/은하군 중심부에서 빈번히 일어나는 은하 병합(merging) 및 조석 상호작용(tidal interaction)에 의한 것으로 보인다.

우리는 3장에서 밀집은하군(Compact Groups of Galaxies)에서 일어나는 은하 진화에 대한 연구를 이야기한다. 밀집은하군은 약 100 kpc 이하의 좁은 공간에 3−10개의 은하들이 밀집해 있으며, 은하 간의 상호작용이 매우 활발한 환경이다. 우리는 Sohn et al. (2016)이 만든 밀집은하군 목록과 *WISE* 자료를 이용하여 밀집은하군에 속한 은하들의 MIR 특성들을 살펴보았다. 밀집은하군 은하들의 중적외선 [3.4] − [12] 색지수는 은하단 은하들에 비해 평균적으로 작다. 이 결과는 밀집은하군에 위치한 은하들의 평균 별 나이(mean stellar age)가 좀 더 많다는 것을 의미한다. 또한, 밀집은하군은 은하단에 비해 낮은 MGV 은하 비율을 보인다. 이러한 작은 MGV 은하 비율은 저밀도 환경에 위치한 밀집은하군과 고밀도 환경에 위치한 밀집은하군 모두에서 발견된다. 이는 밀집은하군에서 은하 진화가 빠르게 진행되었음을 의미한다. 고밀도 환경에 위치한 밀집은하군은 저밀도 환경에 위치한 밀집은하군보다 높은 비율의 조기형 은하들과 작은 MIR 색지수를 갖는 은하들로 이루어져있다. 이는 밀집은하군이 주변 환경으로부터 멤버 은하를 새롭게 공급받는다는 것을 말해주는 관측적 증거이다. 우리는 이 연구를 통해 밀집은하군이 다른 은하 환경보다 은하 진화가 빠르게 진행되는 환경이며, 무거운 타원은하 형성에 크게 기여하는 환경임을 밝혀냈다.

4장에서는 Gemini-North 망원경의 GMOS IFU를 이용한 E+A 은하 연구 결과를 이야기한다. E+A 은하 스펙트럼에서 보이는 강한 발머흡수선(Hγ, Hδ, Hβ)은 젊은 A형 별들의 존재를 의미한다. 하지만 젊은 별들이 주로 분포하는 은하들과는 달리, E+A 은하에서는 Hα와 같은 방출선이 거의 보이지 않는다. 이러한 스펙트럼의 특성은 E+A 은하가 10억년 전 쯤에 강한 별폭발을 겪었지만, 어떠한 이유 때문에 현재는 별형성 활동이 거의 멈춘 상태임을 말해준다. 그러므로 E+A 은하는 Post-Starburst 은하이며, 은하 진화의 중간 단계에 있는 대표적인 은하 종족으로 추정된다. E+A 은하의 젊은 A형 별들의 공간 분포는 별폭발 현상이 일어나는 영역에 대한 정보를 직접적으로 보여준다. 기존의 수치실험에서는 은하 병합 시 가스가 은하 중심부로 모여들고, 은하 중심부로부터 반경 1 kpc 이내의 영역에서 강한 별폭발이 생긴다고 예측한다. 그러나 가까운(0.03 < *z* < 0.05) 다섯개의 E+A 은하들에 대한 우리의 관측 결과는 다섯 은하 모두에서 A형 별들이 1 kpc 영역 바깥까지 넓게 분포하고 있음을 보여준다. 우리는 A

형 별들의 은하 집중도(central concentration)와 별폭발 세기 사이의 상관관계를 발견하였다. 이 결과는 A형 별들의 공간 분포가 E+A 은하가 과거에 겪은 별폭발의 특성에 따라 다르게 나타날 수 있음을 말해준다.

마지막으로 우리는 5장에서 나선은하의 막대 구조와 활동성 은하핵(Active Galactic Nuclei, AGN) 간의 관계에 대한 연구 결과를 이야기한다. 이 연구에서는 약 9천개의 나선은하들과 Lee et al. (2012a)의 분류 결과를 이용하였다. AGN를 보유한 은하들은 그렇지 않은 은하들에 비해 2.5배 높은 확률로 막대 구조를 가지고 있으며, AGN 비율도 막대를 가지지 않은 은하보다 막대은하에서 높게 나타난다. 그러나 은하의 $u - r$ 색지수와 별질량(stellar mass)를 고정하고 비교했을 때는 앞의 결과가 발견되지 않는다. 또한, AGN의 활동 세기를 의미하는 Eddington ratio를 비교한 결과 막대은하와 막대가 없는 은하 사이의 큰 차이를 발견하지 못하였다. 이 결과들은 AGN 활동이 막대가 있는 경우에도 강하게 나타나지 않으며, 막대에 의해서 AGN의 세기가 증가되지 않음을 보여준다.